KU LEUVEN

FACULTY OF SCIENCE

Resonance Laser Ionisation of Lanthanides

A case study of Praseodymium and Europium at CERN

Babet VAN DINGENEN

CERN-THESIS-2024-261
//2024

Supervisor: Prof. T. E. Cocolios
Institute for Nuclear and Radiation Physics *(KU Leuven)*

Mentor: Ralitsa Mancheva
Institute for Nuclear and Radiation Physics *(KU Leuven)* & CERN

Thesis presented in
fulfillment of the requirements
for the degree of Master of Science
in Physics

Academic year 2023-2024

Acknowledgements

Here we are, at the beginning of the finish line. During the six years of my university adventure, I have been able to grow not only academically, but also personally. I have experienced many things during this time, some good, some bad, but I can proudly say 'I made it!'. I'm grateful for the journey, the lessons that came with it and most importantly, the people that are in my life because of it.

This thesis would not have been possible without the help of some people. First of all, I would like to express my gratitude to professor Thomas E. Cocolios. For being my supervisor, but above all for letting me go to CERN for my master's thesis. Thank you for the opportunity, but also the countless efforts made such that I could actually start my exchange. A thanks to my mentor Ralitsa Mancheva is also needed. For translating all the laser jargon I was unfamiliar with in the beginning of this thesis, to collect the data for europium, and the numerous thesis iterations she read through for feedback. I would also like to thank Julius Wessolek for the hours in the lab teaching me how to work with the lasers. Even though it didn't really work out with the praseodymium, I'm grateful for the time spent in the lab figuring things out. Furthermore, my appreciation goes to Kati, Cyril, Reinhard and the rest of the RILIS team for welcoming me, and helping me with suggestions and explanations throughout my time at CERN. Also a special thanks to Max, Sander, Jake, Wiktoria and especially Daan for making the second semester struggle take place in such a nice environment.

Bovendien wil ik ook nog tijd nemen om wat mensen nauw aan mijn hart te bedanken. Eerst en vooral bedankt aan mijn grootouders en mijn zussen, voor de steun en aanmoedigende woorden doorheen mijn studies en natuurlijk ook de vele heerlijke etentjes. Dikke merci aan mijn vrienden: Tijmen, Thomas, Junan want we hebben toch niet zo'n poor life choices gemaakt aangezien het ons heeft samengebracht x; maar ook Caro, Lies, Elise, Charlotte voor de vele boitjes, avonturen, reisjes, roddelsessies en zoveel meer. Bedankt aan jullie allen voor de vriendschap en steun, ik kijk al uit naar wat er nog te wachten staat! Mats, bedankt voor de hulp en ondersteuning tijdens mijn thesis, maar eigenlijk gewoon bedankt voor alles. Wees maar zeker dat ge nog veel gaat afzien met mij. Tot slot wil ik graag deze thesis opdragen aan mijn papa, Peter Van Dingenen. Bedankt voor alle vrijheid die ik heb gekregen tijdens mijn studies maar ook de vrijheid om mezelf te ontdekken. Ik heb er toch iets van kunnen maken ;)

To say it with Taylor Swift's words: It was the end of (almost) a decade, but the start of an age. With this, I would like to present my master's thesis to you. Enjoy!

Contribution Statement

Chapter 1, 2 and 3 are based on cited literature, as well as discussions with Ralitsa Mancheva, Professor Thomas E. Cocolios and Julius Wessolek. I am also grateful to Professor Thomas E. Cocolios for allowing me to attend the ISOLDE Workshop and Users meeting 2023. The experience was enlightening, and valuable for gaining insight on the grand scheme of nuclear physics.

The data for praseodymium has been obtained by Julius Wessolek and me, with the help of Katerina Chrysalidis. The data for europium has been obtained by Ralitsa Mancheva. For both data collections, suggestions were made by the RILIS team on how to improve the laser setup and signal. I would like to express my gratitude to Ralitsa, Julius, Katerina but also the entire RILIS team for their contributions and aid.

I performed all of the data analysis in this thesis, with suggestions from Ralitsa Mancheva.

A more in-depth interpretation of the obtained results awaits a discussion with Professor Matthieu Génévriez. However, this discussion will take place after the submission deadline of this thesis.

Scientific Summary

Nuclear physics is the field that studies the nuclear force, nuclear structure, and nuclear reactions. Moreover, it describes the nucleus using a nuclear model, which depends on the type of nucleus. Lanthanides form a challenge to explain with a nuclear model due to their strong deformation and complex electronic shell structure. To be able to describe them with a good model, more information on their nuclear structure is required. A facility where such experiments on the nuclear structure take place is ISOLDE at CERN.

This thesis focuses on the investigation of two lanthanides, praseodymium and europium. For this investigation, Resonance Ionisation Laser Ion Source, or RILIS at CERN is used. For praseodymium, the laser technique is applied with a focus on spectroscopy applications. For europium, the laser ionisation prioritises production applications.

Many experiments take place at ISOLDE, often quickly one after another. Moreover, different elements require different laser setups. To be able to quickly change gear between experiments with different elements, a versatility in the laser setup is necessary. Titanium-doped sapphire lasers, also Ti:Sa lasers, are preferred in the RILIS laser setup because of their easier setup and reduced maintenance compared to the dye lasers.

After a literature study, two laser schemes were developed for both praseodymium and europium, exclusively using titanium-doped sapphire lasers. Following this, the schemes were evaluated for their practical utility. An atomic sample was implemented in the Photo-Ionization Spectroscopy Apparatus, the so-called PISA. The atomic vapour that came out of the PISA's oven, was irradiated by lasers with the frequencies of the theoretical laser scheme. The laser setup used a Z-fold Ti:Sa in resonance with the first step of the laser scheme. A grating Ti:Sa was used to scan across the ionisation potential. Each time the grating Ti:Sa is in resonance with a Rydberg state, an increased ion signal is observed. The Rydberg states converge to the ionisation potential, hence the peaks converge until they can no longer be resolved.

For praseodymium, no signal was found for either laser scheme. For europium, both laser schemes yielded a signal. Subsequently, they were used to investigate the current literature value of the ionisation potential. After an analysis, the resulting Rydberg scans generated values for the ionisation potential for europium per scan and per wave. The weighted average provided one value for the ionisation value at 5.670242 ± 0.000003 eV. However, due to observed systematic fluctuations and taking into account the limitations of the experimental setup, it is more instructive to present an ionisation region.

Layman Summary

Looking at the periodic table, there are two separate rows of elements with the upper one called the lanthanides. The lanthanides are special because of their nuclear structure. They are tough to describe using a model because of their odd shape and complicated electron arrangements. To have a better understanding of how the lanthanides work, more experiments are needed. ISOLDE at CERN is an example of a facility that can conduct these kinds of experiments.

This thesis focuses on studying two lanthanides, praseodymium and europium. At CERN, a special laser system called RILIS is used to study these elements. For this investigation, a specific type of laser at RILIS is used, called a Ti:Sa laser.

First, a literature study was conducted on how the laser can turn these elements into ions in a preferred way. The laser does this in two successive steps based on the electron orbits and ionisation energy of the element. The specific combination of successive steps is called a laser scheme. For both praseodymium and europium, two such laser schemes were developed and tested.
The testing was done with an apparatus called the Photo-Ionization Spectroscopy Apparatus, also known as PISA. The sample was heated to create an atomic vapour. By combining two Ti:Sa lasers with frequencies according to the laser scheme, the atomic vapour inside the PISA is irradiated, creating a signal.

For praseodymium, no signal was found, indicating that the theoretical laser scheme didn't work as expected. For europium, both laser schemes showed a signal. These signals were then used to investigate what is known about the ionisation energy of europium. After analysing the signals, one value for the ionisation potential of europium was calculated at 5.670242 ± 0.000003 eV. However, due to observed fluctuations combined with technical restrictions in the setup, it was concluded that ionisation happens over a range of energies, rather than at a single value.

List of Abbreviations

Acronyms

ABU	Atomic Beam Unit
AIS	Auto-Ionising State
BIBO	BiB_3O_6 crystal
CERN	Conseil Européen pour la Recherche Nucléaire (European Organization for Nuclear Research)
EM	Electromagnetic
Eu	Europium
GPS	General-Purpose-Separator
HRS	High Resolution Separator
IP	Ionisation Potential
ISOLDE	Isotope Separator On-Line Device
LASER	Light Amplification by Stimulated Emission of Radiation
Nd:YVO	Neodymium-doped Yttrium Orthovanadate laser
Nd:YAG	Neodymium-doped Yttrium Aluminum Garnet laser
PISA	Photo-Ionization Spectroscopy Apparatus
Pr	Praseodymium
PSB	Proton Synchrotron Booster
RIB	Radioactive Ion Beam
RILIS	Resonance Ionisation Laser Ion Source
SEM	Secondary Electron Multiplier
SHG	Second Harmonic Generation
Ti:Sa	Titanium:Sapphire
WL	Wavelength

Symbols

A	Ampere
Z	Atomic number
a_0	Bohr radius
k_B	Boltzmann constant
l_c	Coherence length
σ	Cross section
g_i	Degeneracy of state i
n^*	Effective quantum number
A_{21}	Einstein coefficient for spontaneous emission
B_{21}	Einstein coefficient for stimulated emission
B_{12}	Einstein coefficient for absorption
m_e	Electron mass
e	Elementary charge (> 0)
$\hat{H}$	Hamiltonian
I	Intensity
E_{IP}	Ionisation energy
$\vec{B}$	Magnetic field
μ_0	Magnetic permeability
m	Magnetic quantum number
$\mathcal{R}^*_{\mathrm{Eu}}$	Mass corrected Rydberg constant for europium
N	Number of neutrons
$\vec{l}$	Orbital angular momentum
ω	Photon frequency
h	Planck constant
P	Polarisation
N_i	Population of state i
n_i	Principal quantum number of state i
m_p	Proton mass
δ	Quantum defect
μ	Reduced mass

R	Reflectance
n	Refractive index
$\mathcal{R}$	Rydberg constant
c	Speed of light
$\vec{s}$	Spin
τ_{sp}	Spontaneous lifetime
χ	Susceptibility
T	Temperature
J	Total angular momentum
T	Transmittance
$\vec{M}_{if}$	Transition dipole moment
A	Transition strength
ϵ_0	Vacuum permittivity
v	Velocity
k	Wave vector
λ	Wavelength
$\bar{E}_{\mathsf{IP}}$	Weighted average of ionisation potential

Units

Energy	1 cm^{-1} = 0.00012398 eV

List of Figures

List of Tables

Contents

Chapter 1

Introduction

At the end of the 19th century, the quantum revolution marked the beginning of the development of nuclear physics. Discoveries that boosted the interest of the field include the discovery of radioactivity by Becquerel (1896), the isolation of radium by M. Curie and P. Curie (1898), the proposal of the existence of an atomic nucleus (1911) and its experimental confirmation by Rutherford, the formulation of the liquid-drop model for fission by Bohr and Wheeler (1939), and much more. The development of nuclear physics was at the scientific forefront during the entire 20th century. [1, 2]

Nuclear physics investigates the nuclear force, the nuclear structure, nuclear reactions, and how this knowledge can be used for societal benefit. The use of nuclei, as well as experimental techniques developed for nuclei, have many applications in both applied and theoretical research. Therefore, nuclear physics overlaps with a variety of fields including elementary particle physics, astrophysics and medicine. [2–4]

Some big questions have still not been answered today. What is dark matter and how does it work? How can cancer be better combatted using radioactive tracers? How do quarks interact and make up all matter in the universe? How can all phenomena be explained by one 'Grand Unification Theory'? To help answer these questions, the strong interaction and the behaviour and nature of nuclei need to be better understood.

1.1 Nuclear Structure

An atom consists of a nucleus around which electrons orbit. The nucleus itself is built up from neutrons and protons, which are held together through the strong force. The number of protons in a nucleus is given by the atomic number Z. In the case of a neutral atom, the atomic number is also equal to the number of electrons The number of neutrons in a nucleus is given by N. An element is determined by its atomic number. Each element can have a different N, resulting in a different isotope. The other way around, if N is constant and Z changes, the nuclei are called isobars. At certain proton and neutron numbers, the nucleus shows increased stability. This corresponds to the effect of filled nuclear shells, the so-called shell closures. The occupation numbers for protons and neutrons at which this occurs, are called the 'magic numbers'. The description of a nucleus is called a nuclear model. However, the entire chart of nuclei cannot be described by just one nuclear model, yet.

Different nuclear models are used depending on the type of nucleus. If the isotope is described as a collective ensemble with even Z and even N, vibrations and rotations are used for the description of the isotope. If the isotope is a superposition of single nucleons close to magic numbers, the Shell model or the Nilsson model is used. However, there are also isotopes far from magic numbers, with odd Z and/or odd N. These isotopes experience a strong deformation, and so form a challenge to explain with a nuclear model. To have a better understanding of the nucleus for a nuclear model, an investigation of their nuclear structure is required. [2, 4, 5]

Nuclei can be either stable or unstable. Unstable nuclei decay into a different state, given enough time. The nuclei decay by emitting a particle, like an electron or α-particle, or they transform by fission into two or more lighter nuclei. The investigation of this decay gives information on the energy levels, the angular momentum of the level, the parity and possible electric or magnetic moments. In summary, the study leads to a better understanding of atomic nuclei. [4]

The study of the nucleus is still a very active field. Theoretically, it is predicted that there are around 7000 isotopes in our universe, while only around 3000 isotopes have been observed so far. To investigate and possibly find new isotopes, as well as to broaden the knowledge on the nuclear models, nuclear physicists need experiments. Such experiments are performed using complex setups at large facilities. An example of such a facility is located in the Conseil Européen pour la Recherche Nucléaire (CERN) in Genève, Switzerland. [5]

1.2 ISOLDE at CERN

The ISOLDE facility, also known as the Isotope Separator On-Line Device, at CERN is a radioactive ion beam (RIB) facility that produces RIBs to facilitate experiments in the fields of nuclear and atomic physics, solid-state physics, materials science and life sciences. More detailed information on the workings and context of ISOLDE, is found in references [6–8].

The RIBs allows to study nuclei far from stability, also called exotic nuclei. The beams are produced using protons that impinge on a thick target containing high-Z materials at temperatures over 2000°C. The protons originate from the Proton Synchrotron Booster (PSB; see figure 1.1), and have an energy of 1.4 GeV. The incoming protons create nuclear reactions, such as spallation, fission, or fragmentation. The volatile reaction products are released in the hot environment, such that they will chemically effuse out of the target into an ion source. The ions from the ion source are guided through a mass separating dipole magnet by an electric field, and are extracted as a radioactive ion beam, ready to be delivered to experiments. [6, 10–13]

The protons from the PSB are ejected onto a target at 1.4 GeV as 2 µs pulses with intensity up to 3×10^{13} protons per pulse [7]. The rate at which the reaction products are created inside the target, also called the production rate, depends on the number of protons impinging on the target, the amount of material the protons can interact with and the probability of interaction between the protons and target in that specific area.

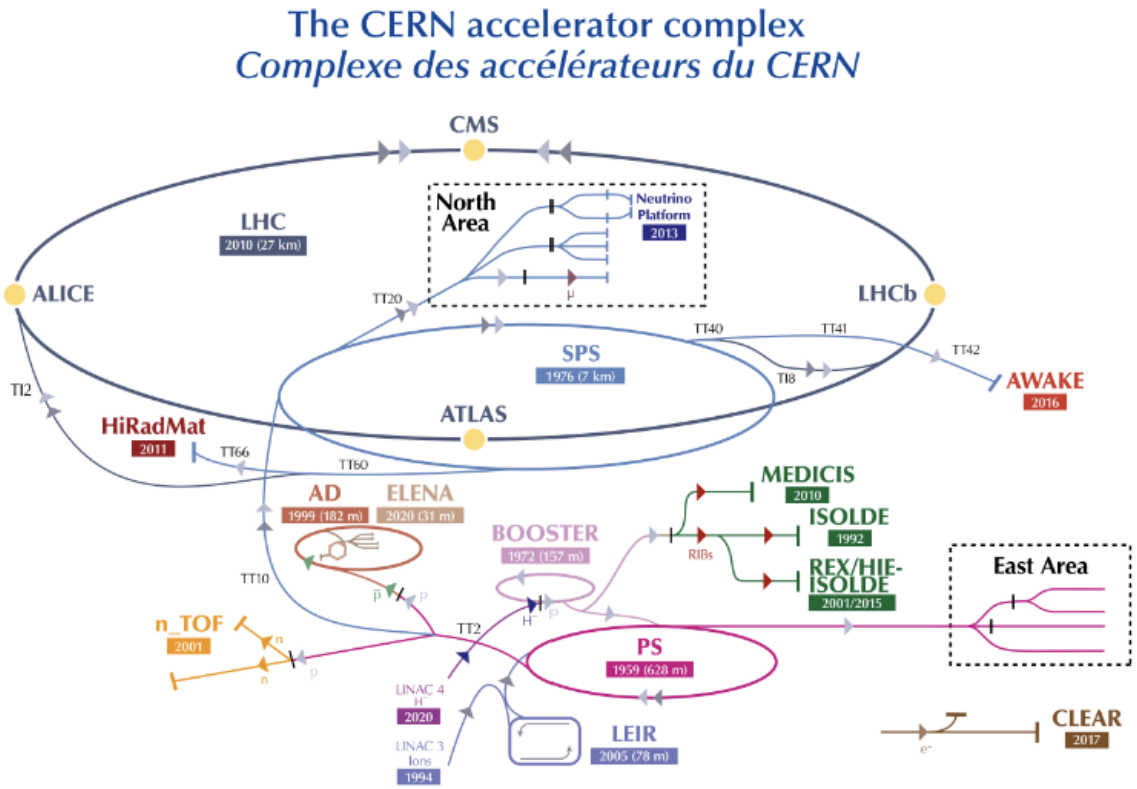

Figure 1.1: *An overview of the different accelerators of CERN. Protons from the Proton Synchrotron (magenta) get accelerated by the Booster (pink) and sent into ISOLDE (green). The other colours represent the different accelerators at CERN. Figure obtained from reference [9].*

In other words, the production rate is proportional to the proton beam flux, the target density and the reaction cross section. The target is heated to around 2000 °C, with the exact temperature depending on the isotope of interest. The high temperatures are necessary for the diffusion and effusion of the reaction products out of the target into the ion source. It also minimises the number ions lost by sticking to the wall. Depending on the isotope of interest, different target-ion source combinations are used (see figure 1.2). The ions created in the ion source are accelerated along the beamline towards the mass separator with a potential of 30kV to 60 kV.
The mass separation occurs using a separator magnet. At ISOLDE, two independent target-ion sourc frontends are available, with their own type of mass separator. The General-Purpose-Separator (GPS) uses a $70°$ doubly focusing bending magnet, and the High Resolution Separator (HRS) couples two magnets for isotope separation together, with respective $90°$ and $60°$ focusing. GPS and HRS can be used simultaneously, allowing for multiple experiments taking place at the same time. [6, 7]

The separator magnets separate the ionised reaction products utilising their charge-to-mass ratio. However, this does not distinguish isobars of different elements, creating a contaminated ion beam. Therefore, to create a beam with a higher degree of chemical purity, an additional element selection is needed. This is where resonance ionisation using lasers comes into play [6, 15].

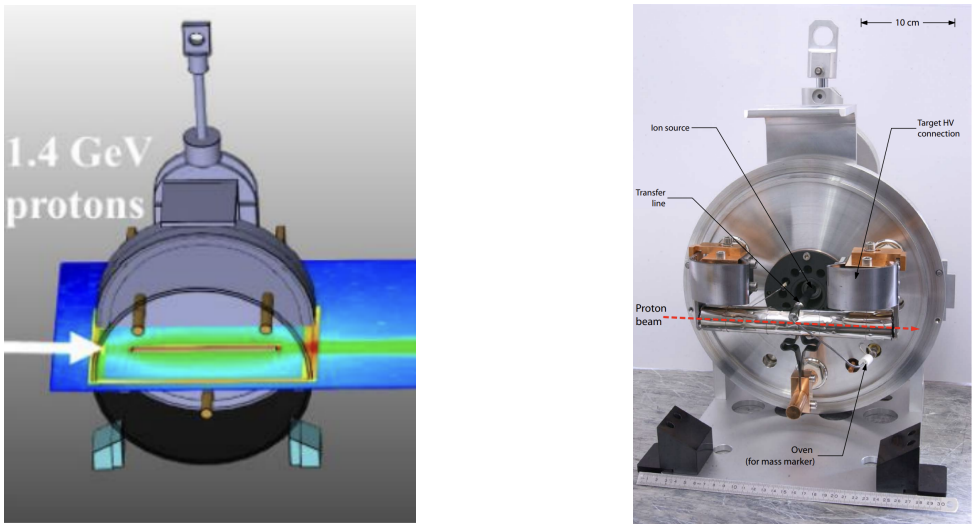

(a) (b)

Figure 1.2: *Depictions of a target used at ISOLDE. The proton beam irradiates a heated target. Ions are created in the ion source and travel through a transfer line. Inside the ion source interactions with a laser occur. The target is heated to release the reaction products. (a) 3D scheme of target with indication of the proton beam. Figure adapted from reference [14] (b) Picture of a target used at ISOLDE with indications of important components, obtained from reference [6].*

The objective of this master's thesis is to use resonance laser ionisation on lanthanides, more specifically praseodymium (Pr) and europium (Eu), for laser scheme development. Lanthanides are difficult to describe analytically with current nuclear models, as they lie in between closed shells. This results in the nuclei of lanthanides being highly deformed. Moreover, lanthanides have a rich electronic structure with overlapping energy levels between lanthanides, increasing their complexity. For both Pr and Eu, an attempt at a laser ionisation scheme development is undertaken. In the case of europium, the developed laser scheme is used to investigate the ionisation potential.

The experiments of the thesis utilise Resonance Ionisation Laser Ion Source (RILIS) at CERN (see section 3). Different lasers are available in the RILIS laser setup, with titanium:sapphire (Ti:Sa) lasers being preferred (see section 3.3). Ti:Sa lasers are more effective to work with and require less maintenance than dye lasers during an experiment run. Ti:Sa lasers are also more versatile and are easier to set up, which is of importance when there is a limited time to switch between experiments on different elements during an ISOLDE run. Hence, the focus of the laser scheme development is on considering schemes with steps exclusively in the Ti:Sa range.

Chapter 2

Resonance Laser Ionisation of Lanthanides

Resonance laser ionisation uses the atomic structure to ionise the atom. This is a multi-step process that brings a valence electron to a higher energy level by absorption of a photon. The photon energy exactly matches the transition energy between the energy levels, which is called being 'in resonance'. The allowed transitions to a higher energy level depend on the selection rules. This chapter goes into the workings of a laser and its ionisation mechanisms in section 2.3. An overview of the implemented optical elements and nonlinear optics is given in section 2.3.2 and section 2.4. Lastly, a short summary on lanthanides is given in section 2.6.

2.1 Atomic Structure

An atom consists of a nucleus with protons and neutrons, around which electrons orbit (see figure 2.1). On the atomic level, the Coulomb interaction between the protons and the electrons, and the electrons themselves, is the dominant inter-particle interaction.

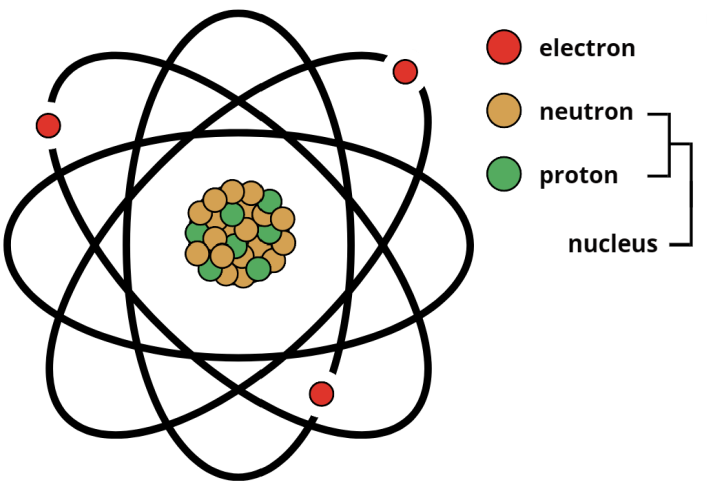

Figure 2.1: *Simplified representation of an atom with protons and neutrons at the center in the nucleus, and electrons at specific orbits around the nucleus.*

An atom has a small size of $V \sim 10^{-28}$ m^3 [16]. As a result, atoms are not visible directly, and the atomic model has to be adjusted based on experimental outcomes. This makes the development of atomic physics an iterative process.
To ionise an atom, a valence electron is excited to a state with its energy higher than the ionisation energy E_{IP}. Consequently, the electron is no longer bound, creating an ion. This process is described quantum-mechanically in its simplest form for a hydrogen atom. (see section 2.1.1). [16, 17]

According to Bohr's atomic model, for the state to be stationary, the Coulomb force has to equal the centripetal force of the nucleus and electron moving in circular orbits around their center of mass. Reducing this two-body-problem into a one-body-problem requires the reduced mass $\mu = \frac{m_e m_p}{m_e + m_p}$, and results in [16]:

$$\mu \frac{v^2}{r} = \frac{1}{4\pi\epsilon_0} \frac{Ze^2}{r^2} \ , \tag{2.1}$$

with v the velocity, r the distance between the nucleus and the electron, ϵ_0 the vacuum permittivity, and e the (positive) elementary charge. For a hydrogen atom the atomic number equals $Z = 1$.
Using the quantum condition for quantised angular momentum $\vec{l}$ yields [16]:

$$\mu r v = |\vec{l}| = n \frac{h}{2\pi} \ , \tag{2.2}$$

with n the principal quantum number and h Planck's constant.
The possible radii for the electron orbits of hydrogen are given by [16]:

$$r_n = \frac{n^2 h^2 \epsilon_0}{\pi \mu e^2} = n^2 a_0 \ , \tag{2.3}$$

with $a_0 = \frac{\epsilon_0 h^2}{\pi \mu e^2}$ the Bohr radius. The total energy of an electron moving in the Coulomb potential of the hydrogen nucleus, is given by [16]:

$$E_n = -\frac{\mu e^4}{8\epsilon_0^2 h^2} \frac{1}{n^2} = -\mathcal{R} \frac{1}{n^2} \ , \tag{2.4}$$

which represents the discretisation of the total energy of the atom for stationary states. The Rydberg constant given by [16]:

$$\mathcal{R} = \frac{\mu e^4}{8\epsilon_0^2 h^2} \ , \tag{2.5}$$

The exact value of the Rydberg constant $\mathcal{R}$ differs slightly for different nuclear masses. More details on this derivation is found in chapter 3 of reference [16].

An atomic transition of hydrogen is described using the empirically found Rydberg formula [16]:

$$\frac{1}{\lambda} = \mathcal{R} \left(\frac{1}{n_i^2} - \frac{1}{n_f^2} \right) \ , \tag{2.6}$$

with $1/\lambda = \nu$ the wavenumber [cm^{-1}], and n_i, n_f the principal quantum numbers of the initial and final state, respectively. Using equation 2.4, the Rydberg formula is rewritten as [17]:

$$E_{n_i} = E_{n_f} - \mathcal{R}\left(\frac{1}{n_i^2} - \frac{1}{n_f^2}\right) . \tag{2.7}$$

For a ground state shifted to zero, the ionisation potential E_{IP} is defined for $n_f \to \infty$, for which the energy states converge, following:

$$E_{\mathsf{IP}} = E_n + \frac{1}{n^2}\mathcal{R} . \tag{2.8}$$

2.1.1 The Hydrogen Atom

A hydrogen atom consists of a nucleus with one proton coupled with one electron. Assuming the absence of an external field, the Schrödinger equation is given by [17]:

$$i\hbar\frac{\partial\Psi(\vec{r},t)}{\partial t} = \hat{H}\Psi(\vec{r},t) , \tag{2.9}$$

with $\hbar = \frac{h}{2\pi}$, $\Psi(\vec{r},t)$ the wave function depending on the position and time, and $\hat{H}$ the Hamiltonian. The Hamiltonian $\hat{H} = \hat{T} + \hat{V}$ represent the energy of a system, depending on both the nucleus and electron as well as their interaction. For hydrogen, the kinetic energy $\hat{T}$ arises from the proton and electron kinetic energy. The potential energy $\hat{V}$ is given by the Coulomb interaction between the proton and electron.

The discrete energy levels of the stationary state are derived from the time-independent Schrödinger equation, with $\Psi(\vec{r},t) \to \exp(-iEt/\hbar)\psi(\vec{r})$ in reciprocal space [17]:

$$\hat{H}\Psi(\vec{r},t) = E\Psi(\vec{r},t) , \tag{2.10}$$

$$\Downarrow$$

$$\hat{H}\psi(\vec{r}) = E\psi(\vec{r}) . \tag{2.11}$$

The resulting Schrödinger equation for a hydrogen atom with respective momenta $p_{e,p} \to -i\hbar\nabla_{e,p}$ [16]:

$$\left(-\frac{\hbar^2}{2m_e}\nabla_e^2 - \frac{\hbar^2}{2m_p}\nabla_p^2 - \frac{e^2}{4\pi\epsilon_0}\frac{1}{r}\right)\psi(\vec{r_e},\vec{r_p}) = E\psi(\vec{r_e},\vec{r_p}) , \tag{2.12}$$

for which m_e and m_p are the respective masses of the electron and proton, ∇_e and ∇_p are the respective Laplace operators for the electron and proton, and $r = |\vec{r_e} - \vec{r_p}|$ is the distance between the two particles obtained from the position of the electron and proton $\vec{r_e}$ and $\vec{r_p}$, respectively.

In this laboratory frame, the proton and electron orbit around each other. In further derivation, the reference frame is changed to the center-of-mass frame, which describes the relative motion $\vec{r}$ of the particles with reduced mass μ. The relative motion of hydrogen is written as the Schrödinger equation for a spherically symmetric potential [16]:

$$-\frac{\hbar^2}{2\mu}\Delta\psi(\vec{r}) - \frac{e^2}{4\pi\epsilon_0}\frac{1}{r}\psi(\vec{r}) = E\psi(\vec{r}) , \tag{2.13}$$

Using spherical coordinates (r, θ, φ), the wave function is separated into a radial function R_{ln} and angular function based on spherical harmonics Y_l^m [16]:

$$\psi_{nlm}(r, \theta, \varphi) = R_{ln}(r) Y_l^m(\theta, \varphi) \ , \tag{2.14}$$

with m the magnetic quantum number. Hence, the quantum numbers (n, l, m) uniquely define the atomic state.

The radial equation for a spherically symmetric potential is given by [16]:

$$\frac{1}{r^2}\frac{d}{dr}\left(r^2\frac{dR}{dr}\right) + \frac{2\mu}{\hbar^2}\left(E + \frac{e^2}{4\pi\epsilon_0}\frac{1}{r}\right)R(r) = \frac{l(l+1)}{r^2}R(r) \ . \tag{2.15}$$

The solution to this equation is found by identifying the asymptotic behavior in the limiting cases as is done in chapter 4 of reference [16]. In general, the solution results from substituting $R(r) = u(r)\exp(-\kappa r)$ with $\kappa = \sqrt{-2\mu E}/\hbar$ into equation 2.15 to obtain:

$$\frac{d^2u}{dr^2} + 2\left(\frac{1}{r} - \kappa\right)\frac{du}{dr} + \left(\frac{2/a_0 - 2\kappa}{r} - \frac{l(l+1)}{r^2}\right)u = 0 \ , \tag{2.16}$$

with a_0 the Bohr radius (see section 2.1). The solution of this equation yields a condition for the energy levels as [16]:

$$E_n = -\frac{\mu e^4}{8\epsilon_0^2 h^2} = \frac{-\mathcal{R}'}{n^2} \ . \tag{2.17}$$

This is the same result as found from the Bohr model in equation 2.4 for $Z = 1$. Remark that the energy is discretised, and only depends on the principal quantum number n. Hence, all atomic states with possible combinations of l and m should have the same energy, the so-called degenerate energy levels. However, this simplistic model does not suffice to describe reality, as not all energy levels of the hydrogen atom for a specific n are degenerate. Thus, other interactions need to be taken into account. [16, 18]

Spin-Orbit Coupling and Fine Structure

When looking at hydrogen, a small splitting of the energy levels is observed. This splitting is only observed in high resolution spectroscopy, and is called the fine structure. It arises from the coupling of the spin of the electron to the orbital angular momentum, also known as spin-orbit coupling.

For a general atom in a coordinate system with the electron at the origin, the proton orbits around the electron with a radius r and proton current $i = \frac{Zev}{2\pi r}$. This proton current generates a magnetic field following Biot-Savart's law with magnetic permeability μ_0 [19]:

$$B = \frac{\mu_0 i}{2r} = \frac{\mu_0 Zev}{4\pi r^2} \ . \tag{2.18}$$

Introducing the orbital angular momentum from equation 2.2 for the magnetic field vector [19]:

$$\vec{B} = \frac{\mu_0 Ze\hbar}{4\pi m_e r^3}\vec{l} \ , \tag{2.19}$$

On the other hand, the electron with charge $-e$ and spin $\vec{s}$ orbiting around the nucleus produces magnetic moment [19]:

$$\vec{\mu}_s = -g_s \frac{e\hbar}{2m_e}\vec{s}\,, \tag{2.20}$$

with g_s the emperical electron spin g-factor. Hence, the interaction of the magnetic moment with the proton magnetic field gives an additional energy contribution [19]:

$$E = -\vec{\mu}_s \cdot \vec{B} = g_s \frac{e\hbar}{2m_e}\frac{\mu_0 Z e\hbar}{4\pi m_e r^3}(\vec{s}\cdot\vec{l})\,. \tag{2.21}$$

A relativistic correction has to be added, to account for the change in coordinate system-. This so-called Thomas precession correction introduces an additional $1/2$, such that the spin-orbit coupling contribution to the energy equates to:

$$E = H_{\mathsf{SO}} = g_s \left(\frac{\mu_0 e^2\hbar^2}{16m_e^2\pi r^3}\right)(\vec{s}\cdot\vec{l})\,. \tag{2.22}$$

The sign of the scalar product depends on the orientation of the spin relative to the orbital angular momentum. The splitting of the energy levels will only be observed for levels with $l > 0$. [16, 19]

Hyperfine Structure

The fine structure levels are split further into sublevels, also known as the hyperfine splitting. This additional contribution to the energy is explained by acknowledging that the atomic nucleus is not point-like and has a finite volume. Hence, a nuclear magnetic moment arises from the nuclear spin $\vec{I}$ [16]:

$$\vec{\mu}_N = g_N \frac{\mu_K}{\hbar I}\vec{I}\,, \tag{2.23}$$

with g_N the emperical nuclear g-factor, and $\mu_K = \frac{m_e}{m_p}\frac{e\hbar}{2m_e}$ the nuclear magneton. Therefore, the hyperfine structure results from the interaction between the nuclear magnetic moment and the electron magnetic field $\vec{B}_J = \frac{B_J}{J\hbar}\vec{J}$ with total angular momentum $\vec{J} = \vec{l} + \vec{s}$. The energy contribution of the hyperfine interaction is given by [20]:

$$E = H_{\mathsf{HF}} = -\vec{\mu}_N \cdot \vec{B}_J = g_N \frac{\mu_K B_J}{\hbar^2 I J}(\vec{I}\cdot\vec{J})\,. \tag{2.24}$$

The interactions between the electron and nucleus yield the corrected energy levels to be:

$$E = E_n + H_{\mathsf{SO}} + H_{\mathsf{HF}} = \frac{-Z\mathcal{R}'}{n^2} + g_s\left(\frac{\mu_0 Z e^2\hbar^2}{16m_e^2\pi r^3}\right)(\vec{s}\cdot\vec{l}) + g_N\frac{\mu_K B_J}{\hbar^2 I J}(\vec{I}\cdot\vec{J})\,. \tag{2.25}$$

Even though more corrections could be added, this equation already shows how the energy level depends on the atom. EHence, each isotope with different $\vec{s}, \vec{l}, \vec{I}, \vec{J}$ will have different energy levels. Therefore, the unique electronic structure is seen as the atomic fingerprint.

For each combination of n, l, J a different series of levels converge to the ionisation potential following equation 2.8. Each series is called a Rydberg series.
In the case of multi-electron atoms, the energy levels are more complicated due to inter-particle interaction. To account for the average effect of the core and multiple valence electrons, a new parameter is introduced, called the quantum defect δ[1]. This allows for the introduction of the effective quantum number, defined as [17]:

$$n^* = n - \delta \ . \tag{2.28}$$

Moreover, the core and multiple valence electrons als influence the Rydberg constant. Therefore, it is more appropriate to use a mass corrected Rydberg constant $\mathcal{R}^*$ value for a specific element. The ionisation potential for an atom with multiple electrons is extended to [17, 22]:

$$E_{\mathsf{IP}} = E_n + \frac{\mathcal{R}^*}{(n^*)^2} \ . \tag{2.29}$$

In the case of lanthanides, additional effects on the Hamiltonian have to be included, such as electron-electron Coulomb interactions, external crystal field contributions and ligand-field interactions. They need to be concluded to more accurately predicts energy levels and Rydberg states. For more information on how these interactions affect the energy and lift degeneracies, see references [23, 24]. The additional effects generate a complex electronic shell structure with more energy levels. More information on lanthanides in section 2.6.

2.2 Light-Matter Interaction

Matter can interacts with light through the absorption or emission of photons. These interactions cause transitions in matter. The interaction of light with matter is described by either the Einstein treatment or semi-classically.

2.2.1 Einstein Treatment

In the Einstein treatment, light, or more general radiation, interacts with matter through either spontaneous emission, absorption or stimulated emission (see figure 2.2). Considering the electron in the initial state with energy E_1 that transitions to a final state with energy E_2. The energy difference between the transition levels defines the photon energy with photon frequency ω_{21} as [25]:

$$\hbar\omega_{21} = E_2 - E_1 \ . \tag{2.30}$$

[1] In reality, $\delta(n)$ depends on n. For smaller n values the atomic radius is smaller, thus experiences less screening. The quantum defect is described by W. Ritz by the approximation:

$$\delta(n) = \delta(n) + \frac{\beta}{(n-\delta(n))^2} + \frac{\gamma}{(n-\delta(n))^4} \dots \tag{2.26}$$

$$\approx \delta_0 + \frac{\beta}{(n-\delta_0)^2} + \frac{\gamma}{(n-\delta_0)^4} \dots \tag{2.27}$$

However, to good approximation the value for $\delta(n)$ becomes constant for $n \geq 10$. Accordingly, in this thesis the quantum defect is seen as a constant $\delta_0 = \delta$. For more details on the significance of the substitution of the quantum defect $\delta(n)$, see references [21, 22].

At thermal equilibrium, the populations N_1, N_2 of the respective lower and higher energy levels are governed by Boltzmann's statistics. The ratio of the two level populations is described by the Boltzmann equation as [26]:

$$\frac{N_2}{N_1} = \frac{g_2}{g_1} \exp\left(\frac{-(E_2 - E_1)}{k_B T}\right) = \frac{g_2}{g_1} \exp\left(\frac{-\hbar\omega}{k_B T}\right) , \tag{2.31}$$

with k_B the Boltzmann constant, temperature T, and g_1, g_2 the respective degeneracies of the energy levels. From this equation is deduced that for a higher energy level, the exponent decreases, meaning that fewer atoms are in that state, or also $N_1 > N_2$. [27]

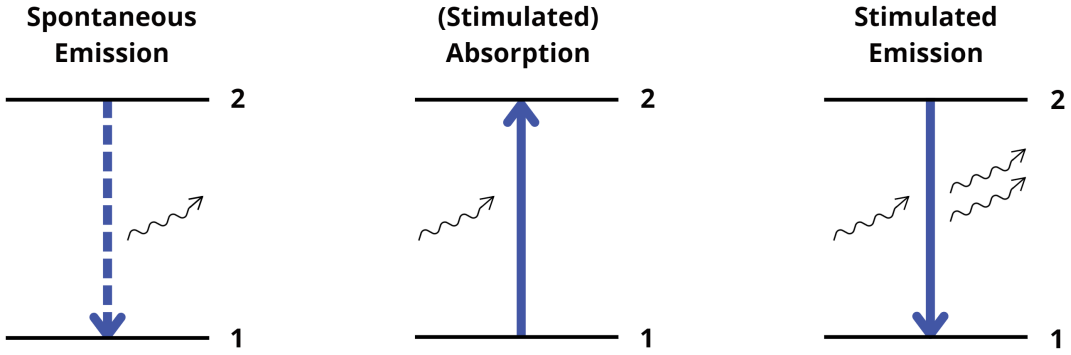

Figure 2.2: *Schematic representation of the different interactions between light and atoms. For Spontaneous emission, a photon is emitted when the electron transitions from a higher energy level 2 to a lower energy level 1. During the absorption process, a photon is absorbed by the atom, exciting the electron from a lower energy level 1 to a higher energy level 2. Stimulated emission is the process during which an incident photon stimulates the atom to emit another photon coherent with the first photon. The electron decays from the higher energy level 2 to a lower energy level 1. Based on figure in reference [25].*

Spontaneous Emission

Spontaneous emission is the process in which the atom emits the photon with energy $\hbar\omega_{21}$ in any direction. The decay creates a change of population dN_2 of the upper level within a time dt determined by the Einstein coefficient of spontaneous emission A_{21} to be [26]:

$$dN_2 = -A_{21} N_2 dt \ . \tag{2.32}$$

Through this equation, the Einstein coefficient A_{21} is related to the average lifetime of an excited two-level atomic system with respect to spontaneous emission, also the spontaneous lifetime τ_{sp} [26]:

$$A_{21} = 1/\tau_{sp} \ . \tag{2.33}$$

Absorption

During the absorption process, photons with energy $\hbar\omega_{12}$ are absorbed by the atom. As a result, the electrons go from a lower energy level to a higher energy level. Consequently, absorption is only possible in the presence of a field, being a stimulated

process. The rate of absorption dN_1 within a time interval dt is proportional to the spectral energy density ρ of the radiation field [26]:

$$dN_1 = -B_{12}\rho(\omega_{12})N_1 dt \ , \tag{2.34}$$

with B_{12} the Einstein coefficient of absorption and $\rho(\omega_{12})$ the spectral energy density at the photon frequency ω_{12}.

Stimulated Emission

Stimulated emission is a process where a second photon is emitted from the atom, due to the presence of a first photon with the same frequency. The incident photon with energy $\hbar\omega_{21}$, stimulates the atom to decay to a lower level by emitting a second photon of energy $\hbar\omega_{21}$. The two photons are coherent. The rate of change of the higher energy level dN_2 by stimulated emission is given by [26]:

$$dN_2 = -B_{21}\rho(\omega_{21})N_2 dt \ , \tag{2.35}$$

with B_{21} the Einstein coefficient of stimulated emission and $\rho(\omega_{21})$ the spectral energy density at the photon frequency.

All three Einstein coefficients remain constant for an atomic transition, independent of the radiation field. So, their value only depends on the transition.

In an ensemble of stationary atoms in a blackbody closed cavity, the individual atoms constantly transition to higher and lower levels. In dynamic equilibruim, the average total number of atoms in a given state for an ensemble remains constant. Considering the cavity at temperature T and energy density $\rho_B(\omega)$, the rate of transitions are equated. This shows the balance between the rate of absorption of photons and the total rate of emission. Writing the relation in terms of Einstein coefficients gives [25]:

$$N_1 B_{12}\rho_B(\omega_{21}) = N_2 B_{21}\rho_B(\omega_{21}) + N_2 A_{21} \ . \tag{2.36}$$

Rewriting this equation yields the energy density of the blackbody radiation at ω_{21}:

$$\rho_B(\omega_{21}) = \frac{A_{21}/B_{21}}{\frac{N1}{N_2}\frac{B_{12}}{B_{21}} - 1} \ . \tag{2.37}$$

By substituting the ratio of populations using equation 2.31, the energy density equates to:

$$\rho_B(\omega_{21}) = \frac{A_{21}/B_{21}}{\frac{g_2}{g_1}\exp\left(\frac{-\hbar\omega}{k_B T}\right)\frac{B_{12}}{B_{21}} - 1} \ . \tag{2.38}$$

This equation is related to Planck's law, resulting in the Einstein relations under thermal equilibrium:

$$\frac{A_{21}}{B_{21}} = \frac{\hbar\omega_{21}^3}{\pi^2 c^3}, \tag{2.39}$$

$$g_1 B_{12} = g_2 B_{21}. \tag{2.40}$$

From the first equation is deduced that more photon absorption leads to an increase of spontaneous emission. This is understood from more photons being available spontaneous emission according to the spontaneous lifetime τ_{sp}. On the other hand, from the second equation is derived that for atomic systems with states of equal degeneracies, rate of stimulated emission and absorption is equal. This results from every other photon inducing absorption, while the second photon induces this absorbed photon to be emitted.

2.2.2 Semi-Classical Description

In the semi-classical description of light-matter interaction, matter is treated quantum-mechanically, while the photon field is described classically. The electric dipole moment of a valence electron $\vec{p}$ interacts with the electric field $\vec{E}$ of the light wave. The average dipole moment over volume $d\tau$ of an arbitrary state $i = (n, l, m_l, m_s)$ with stationary wave function ψ_i is defined by [16]:

$$\langle \vec{p} \rangle = e\langle \vec{r} \rangle = e \int \psi_i^* \vec{r} \psi_i d\tau \ , \tag{2.41}$$

with $\vec{r}$ the position vector of the electron with the nucleus at the origin. Similarly, the transition $E_i \rightarrow E_f$ is described by the transition dipole moment that takes the wave functions of both states into account [16]:

$$\vec{M}_{if} = e \int \psi_i^* \vec{r} \psi_f d\tau \ . \tag{2.42}$$

The average radiation power emitted by an atom that undergoes the transition $E_i \rightarrow E_f$, integrated over all directions, becomes [16]:

$$\langle P_{ik} \rangle = \frac{4}{3} \frac{\omega_{if}^4}{4\pi\epsilon_0 c^3} |M_{if}|^2 \ . \tag{2.43}$$

Relating this to the Einstein equations with N_1 atoms in energy level E_1 transitioning to E_2 spontaneously gives the average power emitted by N_1 atoms to be:

$$\langle P \rangle = N_1 A_{12} \hbar \omega_{12} \ . \tag{2.44}$$

Comparing equation 2.43 and equation 2.44 for N_1 atoms, yields the relation between the transition moment and the Einstein coefficient for spontaneous emission as:

$$A_{12} = \frac{1}{3\pi\epsilon_0} \frac{\omega_{12}^3}{\hbar c^3} |M_{12}|^2 \ . \tag{2.45}$$

Combining this result with the equation found in equation 2.39 gives the relation between the transition moment and the Einstein coefficient of stimulated equation:

$$B_{12} = \frac{\pi}{3\hbar^2\epsilon_0} |M_{12}|^2 \ . \tag{2.46}$$

This allows for the calculation of the Einstein coefficients. Additionally, the transition dipole moment is only non-zero for allowed transitions, which are described by the selection rules.

Selection Rules

Electron transitions between different levels with energy E_1 and E_2, respectively, are subject to selection rules, meaning that not all transitions are allowed. Besides the conservation laws that must be fulfilled, other selection rules arise for a zero transition moment. A transition moment zero implies a forbidden transition.
Considering that the transition moment is a vector, only one of its components has to be non-zero for a transition to be allowed. The difference in light polarisation[2] translates in a different non-zero component of the transition moment, as is found in chapter 7 of reference [16].

1. **Change in Magnetic Quantum Number** Δm

   A first selection rule is set for the magnetic quantum number m. The selection rules follows from the conservation of angular momentum. The transition moment is non-zero only if $\Delta m = 0$ for linearly polarised light and $\Delta m = \pm 1$ for circularly polarised light.

2. **Change in Total Angular Momentum** ΔJ

   Another constraint for an allowed transition is on the electronic angular momentum l and on the spin quantum number s. As consequence of the conservation of angular momentum, the selection rule on the electronic angular momentum states that $\Delta l = \pm 1$. On the other hand, the spin quantum number of electrons that don't transition, doesn't change. Hence, this results in the selection rule $\Delta s = 0$, as transitions between a singlet and triplet quantum state are forbidden[3]. Combining these results, yields the general selection rule for total angular momentum J as:

   $$\Delta J = 0, \pm 1 \ , \quad \text{except} \quad J = 0 \nrightarrow J = 0 \ . \tag{2.47}$$

   Since $-l \leq m \leq l$, the magnetic quantum number has to oblige $m = 0 \nrightarrow m = 0$ as well for $\Delta J = 0$.

3. **Change in Parity** Π

   During the transition from level 1 to level 2 a photon is either absorbed or emitted, with the photon having spin $s = \pm\hbar$. Due to conservation of angular momentum, the atom must change its angular momentum during the transition by $\pm\hbar$. Therefore, the wave functions of the initial and final states need to have opposite parity. This is consistent with the negative parity of the photon, such that the system's parity switches when the photon interaction occurs. The selection rule for parity is written as $\Pi(E_k) = -\Pi(E_i)$.

In this description of light-matter interaction is assumed that the interaction occurs in the form of electric dipole interactions. Other types of interactions possible include the magnetic dipole interaction, the electric quadrupole interaction or even higher order terms. However, electric dipole interactions are typically dominant. For more details on how to describe and deduce other light-matter interactions, see references [17, 22].

[2] Light has either only a z-component for a linearly polarised wave, or an x- and y-component for circular polarised light with the z-axis the quantisation axis.

[3] For an atom with strong spin-orbit coupling, s is no longer a good quantum number. In those cases, transitions with $\Delta s = \pm 1$ are possible, but they have a much weaker intensity than an allowed transition. For those atoms, j-j coupling is introduced, as explained in reference [17]. [16]

2.3 LASER

a Light Amplification by Stimulated Emission of Radiation (laser) amplifies an oscillating light wave through stimulated emission. A laser requires stimulated emission to be the dominant process in light-matter interaction (see section 2.2). It is used in combination with frequency selective optical elements (see section 2.3.2) and possibly nonlinear optics (see section 2.4) to create a specific laser frequency. This laser frequency is then used to ionise an atom via varying ionisation mechanisms (see section 2.3.3).

2.3.1 Laser Principle

A laser consists of a pumping system, an active medium and a laser resonator (see figure 2.3). Inside the active medium, also known as the gain medium, a higher energy state E_2 is more populated than the initial state with lower energy E_1,which is a so-called population inversion. This population inversion with population difference $N_2 - N_1 > 0$, is created by energy transfer of the pumping system. Hence, the population distribution deviates from Boltzmann statistics given in equation 2.31, as the system is not in thermal equilibrium. Taking into account degeneracies of the respective energy levels, the condition for population inversion is rewritten as [25]:

$$g_1 N_2 - g_2 N_1 > 0 \,. \tag{2.48}$$

Population inversion is a necessary condition to create a system in which stimulated emission has a higher rate compared to the rate of absorption. Conversely, the net effect would result in the damping of the radiation, as the photon field is absorbed instead of amplified. The laser resonator stores the emitted light in modes of the radiation field, enhancing stimulated emission in these modes. The stimulated emission surpasses spontaneous emission as dominant process, which results in coherent light that keeps traveling back and forth in the laser resonator, amplifying the light. [16, 25–28]

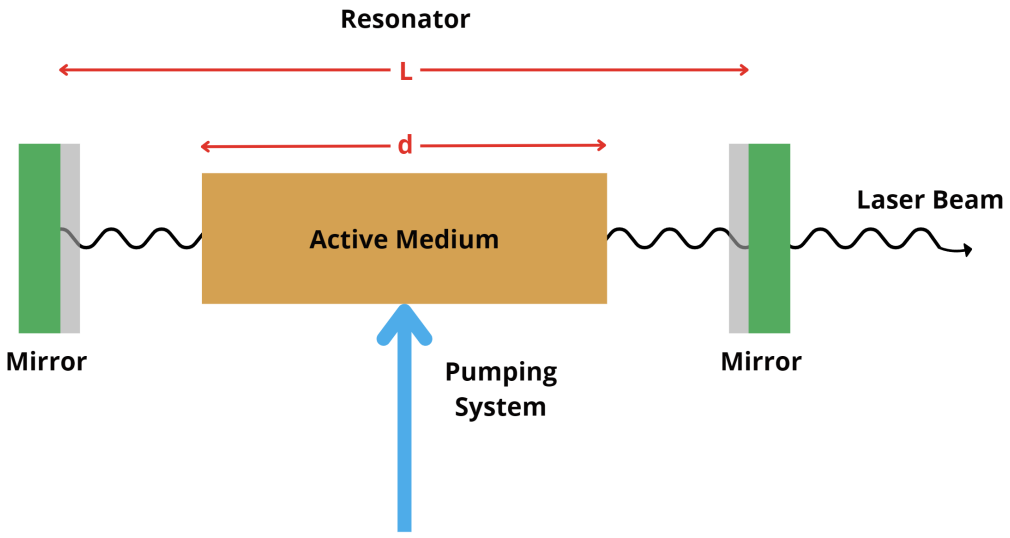

Figure 2.3: *Schematic representation of a laser system containing a pumping system, active medium and resonator. The pumping system ensures population inversion in the active medium. Stimulated emission amplifies the light travelling back and forth in the resonator. Figure adapted from reference [16].*

1. **Pumping system:**

   At thermal equilibrium, population inversion cannot exist because of its short spontaneous lifetime. Hence, population is not a stable state and is short lived. The laser system needs a continuous external pumping system to maintain it. Without the pumping system, the laser system reverts back to stable spontaneous emission as dominant process. [16, 25, 26]

   Consider a pump rate R_2 of the upper level with the lifetime of the upper level τ_2. Similarly, the pump rate and lifetime of the lower level R_1 and τ_1 are defined, although without including spontaneous emission on the laser transition. The change of population dN per unit time dt depends on the pump rate, as well as the lifetime. For the lower energy level, spontaneous emission from the higher energy level also influences the population, as described by equation 2.32. The resulting population changes are given by [25]:

$$\frac{dN_1}{dt} = R_1 + N_2 A_{21} - \frac{N_1}{\tau_1} \,, \tag{2.49}$$

$$\frac{dN_2}{dt} = R_2 - \frac{N_2}{\tau_2}. \tag{2.50}$$

   For a steady-state, the rate of change becomes zero, returning expressions for the populations. By relating these expression to equation 2.48, population inversion for a steady-state is described by:

$$\frac{R_2}{R_1}\frac{\tau_2}{\tau_1}\frac{g_1}{g_2}\left(1 - \frac{g_2}{g_1}A_{21}\tau_1\right) > 1 \,. \tag{2.51}$$

   To achieve population inversion either the upper laser level needs to be pumped more rapidly ($R_2 > R_1$), the lower level should decay more rapidly ($\tau_1 < \tau_2$) to keep the population of the lower level small, or the population per state of the lower laser level should be smaller ($g_1 > g_2$). Additionally, $A_{21} < \frac{g_1}{g_2}\frac{1}{\tau_1}$, which ensures that the rate of spontaneous emission from level 2 is smaller than the total decay rate of electrons from level 1. Hence, the built up from spontaneous emission in the population of N_1 decays quickly enough, such that population inversion is maintained. [25]

   Examples of pumping systems used are a flashlamp, a gas discharge, an electric current, or another laser. [16]

2. **Active Medium:**

   Inside the active medium, absorption and stimulated emission are competing processes. In the simplest case, the laser uses two levels to be operational. The laser frequency has a value at or near the angular transition frequency [26]:

$$\omega_{\text{laser}} \sim \frac{E_2 - E_1}{\hbar} \,. \tag{2.52}$$

   However, lasers can use multiple energy levels to be operational. A laser typically uses more levels, as otherwise N_2 can become saturated and the medium, resulting from spontaneous emission occuring faster than stimulated emission.

By introducing an additional metastable state, the electron is in an excited state for a longer time. This increases the time for stimulated emission to occur, hence increasing stimulated emission. For a multi-level laser, the pumping frequency is higher than the emitted photon frequency, as the emitted frequency originates from a lower lying metastable state. [26]

Specifically for semiconductor lasers, the active medium is an ion-doped metal. Free ions that are excited by the pumping system go into the absorption band and decay with the characteristic frequency. The active medium is cut at Brewster's angle, which polarises the laser light. [27]

3. **Fabry-Pérot Resonator:**
The laser resonator stores the energy obtained from stimulated emission within resonator modes. A single resonator mode is a wave with a broad spectral range.

A Fabry-Pérot resonator consists of two mirrors, located a distance L apart from each other. Taking laser radiation propagation along the z-direction and mirrors perfectly reflecting with the dimensionless reflectivity coefficients $R_1 = R_2 = 1$. The laser field within a resonator is described as a quasiplane standing wave composed of two waves of equal amplitude A but opposite propagation direction [26]:

$$E = \frac{A}{2}\cos\Big(\omega t - (kz - \varphi_0)\Big) + \frac{A}{2}\cos\Big(\omega t + (kz - \varphi_0)\Big)\ . \tag{2.53}$$

The field is rewritten as a standing wave:

$$E = A\cos(kz - \varphi_0)\cos(\omega t). \tag{2.54}$$

When the field travelled a round trip through the resonator over a distance 2L, it needs to return back to its original configuration. This resonator eigenvalue problem leads to the condition for the wave vector k [26]:

$$k_l = l \times \frac{2\pi}{2\mathrm{L}}\ , \tag{2.55}$$

with l the order of resonance. Using the dispersion relation $\omega = kc$, the resonance angular frequencies of a resonator become multiples of $c/2$L:

$$\omega_l = l \times \frac{2\pi c}{2\mathrm{L}}\ . \tag{2.56}$$

These resonator frequencies are equidistant, with subsequent resonance frequency distances, also called the spectral range of the cavity:

$$\omega_l - \omega_{l-1} = \frac{2\pi c}{2\mathrm{L}}\ . \tag{2.57}$$

The boundary conditions state for $z = 0$ and $z =$L that $E = 0$. From this, the phase offset is found to be $\varphi_0 = -\pi/2$, such that the standing wave:

$$E = A\sin(k_l z)\cos(\omega_l t)\ . \tag{2.58}$$

The field varies with time and phase. Hence, each combination of k_l and ω_l represents a single mode of spectral range $\frac{\pi c}{2\mathsf{L}}$. By increasing the length of the resonator, the spectral range is decreased.

The energy stored in this pattern of electromagnetic waves is quantised for each mode as [26]:

$$E_n = n \times \hbar\omega_l \ , \tag{2.59}$$

with $n = 0, 1, 2 \ldots$ the number of photons for a single mode, neglecting the zero point energy. [16, 26]

However, this description is not complete, as the photons in the resonator also propagate through the active medium. Hence, a decrease in the intensity of the photon field going through the active medium, has to be taken into account. Furthermore, in reality one of the two mirrors is a partial reflector, as it couples out some light for the laser beam. Besides rectangular plane mirrors, curved mirrors can also be used instead.

An open resonator consists of spherical mirrors, with an active medium inside the resonator. The spherical mirrors concentrate the stimulated emission at the resonator axis, as only those travelling along the axis are reflected. Rays that travel with an inclination compared to the mirrors, leave the resonator. The mirror diameter is small compared to mirror separation, leading to an increase in diffraction losses. Because of these diffraction losses, the radiation field is transformed into a Gaussian standing wave. This slightly changes the resonance wave number and resonance frequencies to [26]:

$$k_l\mathsf{L} = \left(l + \frac{1}{2}\right)\pi \ , \tag{2.60}$$

$$\omega_l = l \times \frac{\pi c}{\mathsf{L}} + \frac{c}{4\mathsf{L}} \ , \tag{2.61}$$

with the second term of ω_l attributed to the gaussian wave shape. More information on resonators, different resonator configurations and their mathematical description is found in references [16, 26, 28].

Threshold condition

The change in intensity of a monochromatic electromagnetic (EM) wave traveling though a medium is described by Beer's law. The EM wave with frequency $\omega = \frac{E_2 - E_1}{\hbar}$ and initial intensity $I(\omega, 0)$ propagating through a medium of length d along the z-direction is written as [16]:

$$I(\omega, z) = I(\omega, 0) \cdot \mathsf{exp}\left(-\alpha(\omega) \cdot z\right) \ , \tag{2.62}$$

with the frequency-depedent absorption coefficient of the medium given by [16]:

$$\alpha(\omega) = \left(N_1 - \frac{g_1}{g_2} N_2\right) \sigma(\omega) \ , \tag{2.63}$$

and $\sigma(\omega)$ the absorption cross section of the transition $2 \rightarrow 1$. Using the condition for population inversion from equation 2.48, the absorption coefficient becomes smaller

than zero. In turn, the transmitted wave is amplified instead of attenuated. The light wave inside the resonator travels back and forth between parallel mirrors, passing multiple times through the active medium. The amplification factor $G(\omega)$ per passing, assuming no energy losses per round trip, is given by [16]:

$$G(\nu) = \frac{I(\omega, 2\mathsf{L})}{I(\omega, 0)} = \exp(-2\alpha(\omega) \cdot d) \ , \tag{2.64}$$

which for $\alpha(\omega) < 0$ becomes larger than one. Despite a positive amplification factor, the light is not instantaneously amplified, as there are also losses that attenuate the wave. Such losses include reflection losses, diffraction, absorption and scattering. [16]
Reflection losses are due to an imperfect mirror with reflection coefficient $R \neq 1$. Only fraction R of the incident intensity is reflected. At each passing at the mirror, a fractional reflection loss of $(1-R)$ occurs. The wave propagating in the laser resonator also experiences diffraction, resulting in angular spread. As a result, a fraction of the intensity is not reflected back into the active medium and is lost from the resonator. Lastly, some of the light is absorbed by and scattered of from optical elements of the laser system. The cumulative sum per roundtrip is given by the loss factor γ. The decrease in intensity per roundtrip as described by Beer's law becomes [16]:

$$\frac{I(2\mathsf{L})}{I(0)} = e^{-\gamma} \ . \tag{2.65}$$

For light amplification, the amplification should be larger than attenuation. This yields a threshold condition for a self-sustained oscillation to be $2\alpha(\omega) \cdot d + \gamma \leq 0$. The minimum inversion $\Delta N = N_1 \frac{g_2}{g_1} - N_2$ for lasing must fulfil [16]:

$$\Delta N \geq \frac{\gamma}{2\sigma \cdot d} \ . \tag{2.66}$$

Stimulated emission produces coherent light, which means that there is a constant phase relation between two superposed photons. In other words, their phase difference is constant for a period of time or space. The phase of a photon i is given by $\phi_i(z,t) = kz - \omega t$. Hence, for the superposed photons to be temporally coherent, the temporal phase difference $\Delta\phi_t = \phi_1(z,t_1) - \phi_2(z,t_2)$ is constant at any given point z. The time interval $\delta t_c = t_2 - t_1$ is the coherence time of the photons, which is the time that the phase relation between the photons is constant for fixed z. Analogous for spatial coherence, the spatial phase difference $\Delta\phi_z = \phi_1(z_1,t) - \phi_2(z_2,t)$ is constant within spatial coherence length $\Delta z_c = z_2 - z_1$. Spatial and temporal coherence lengths are related via [27]:

$$\Delta z_c = c\Delta t_c \ . \tag{2.67}$$

Typically, laser light has a coherence length between $1 - 10000$ km [29]. [27–29]

Lineshape of laser beam

Contrary to what has been assumed until this point, laser light doesn't consist of just one frequency, as is suggested by equation 2.52. Due to the described losses, the amplitude of the emitted radiation decreases when it travels through the active medium.

These losses are redistributed at slightly different frequencies, resulting in a superposition of monochromatic oscillations $\exp(i\omega t)$ with different frequencies ω and amplitudes $A(\omega)$ [28]:

$$I(t) = \frac{1}{2\sqrt{2\pi}} \int_0^\infty A(\omega) e^{i\omega t} d\omega \ . \tag{2.68}$$

With the amplitude distribution described by a Lorentzian profile, characterised as [28]:

$$A(\omega - \omega_0) = I_0 \frac{\gamma/2\pi}{(\omega - \omega_0)^2 + (\gamma/2)^2} \ , \tag{2.69}$$

with full width at half-maximum (FWHM) $\delta\omega_n = \gamma$, and the profile centered around ω_0 the laser frequency as determined by equation 2.52.

Different mechanisms also lead to additional broadening of the emitted radiation. They are classified in homogeneous and inhomogeneous broadening mechanisms. For more on broadening mechanisms and how they influence the lineshape, see references [25, 26, 28]. The resulting lineshape follows a Voigt profile, generated from the convolution of the natural Lorentzian profile and broadened Gaussian profile. [28]

2.3.2 Tunable Laser

A laser is said to be a tunable laser once frequency selective and frequency tuning elements are added to the cavity. The combination of different optical elements yields the desired frequency of the laser. Optical elements that select a laser frequency are a Lyot filter and a Fabry-Pérot interferometer. The frequency is changed continuously using a diffraction grating. For more detailed explanations on the frequency selective elements, see references [26–28].

Lyot Filter - Mode Selection

A laser oscillates on multiple modes simultaneously (see section 2.3.1). To select one single mode, a Lyot filter is inserted into the resonator. A Lyot filter is an optical filter consisting of birefringent polarizers. Birefringence is the optical property of a medium originating from anisotropic binding forces. This anisotropy leads to an anisotropy in the refractive index n_i. Light propagating through a birefringent medium is split into ordinary o-rays and extraordinary e-rays depending on the polarisation of the light. The medium is transparent for o-rays, which travel at the same speed according to $v_o = c/n_o$. On the other hand, e-rays propagate at different speeds in different directions because of the refractive index n_e. [27]
In a birefringent polarizer, ploarised light is split in o- and e-rays with respective wave numbers $k_o = n_o k$ and $k_e = n_e k$, and phase velocities $v_o = c/n_o$ and $v_e = c/n_e$. The difference in refractive index culminates a phase difference between the two partial waves, given by [28]:

$$\Delta\phi = k(n_o - n_e)x = \frac{2\pi}{\lambda} \Delta n x \ , \tag{2.70}$$

with x the length of the polarizer. This phase difference depends on the polarisation of the incoming light. Only one of the partial waves is amplified, as the other partial

wave experiences strong losses. The transmission function of a Lyot filter for parallel polarisation of incident and transmitted waves, is given by [28]:

$$I(\lambda) = I_0 \cos^2(\frac{\pi \Delta n x}{\lambda}) \ . \tag{2.71}$$

The free spectral range of the Lyot filter is defined by [28]:

$$\delta\omega = \frac{2\pi c}{\Delta n x} \ . \tag{2.72}$$

This free spectral range translates in selection of a single mode. The wavelength of the transmission peak at broad frequency is tuned by changing Δn. This is done by rotating the birefringent polarizers with respect to each other, as it changes the refractive index n_e. [26, 28]

Fabry-Pérot Interferometer - Frequency Selection

Once the laser oscillates on a single mode, the frequency is tuned more finely by a Fabry-Pérot interferometer (FPI). A FPI, also called an etalon, consists of two parallel, plane plates, separated at a fixed distance d (see figure 2.4). In between the two mirrors, a ray is reflected multiple times and subsequently focused onto a screen. However, at every reflection, part of the ray is transmitted and is focused on the screen as well. At the focus, all the transmitted rays and the reflected ray interfere, creating multiple-beam interference. Only rays that originate from the same initial ray interfere. Two different initial rays are not coherent, meaning that there is no sustained mutual interference. The resulting interference pattern of the etalon on the screen are narrow concentric

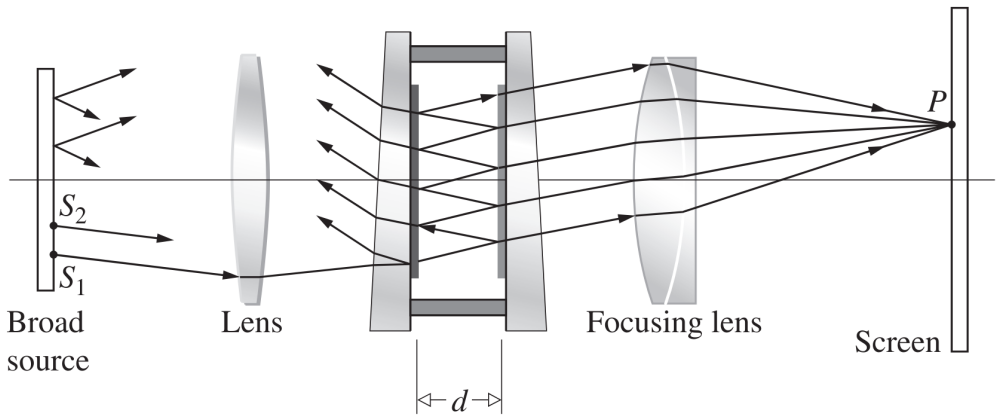

Figure 2.4: *Schematic representation of fixed Fabry-Pérot Interferometer. Two plane, parallel mirrors are a distance d apart, in between which multiple reflections of a wave occur. This yields a multiple-beam interference pattern according to the Airy function $\mathcal{A}(\theta)$ on the screen. Figure obtained from reference [27]*

rings, described by the Airy function $\mathcal{A}(\theta)$. This Airy function depends on the angle θ between the laser beam impinging on the etalon and the normal to the etalon. The phase difference between successively transmitted waves is characterised by [27]:

$$\delta = \frac{4\pi n}{\lambda} d \cos(\theta_t) \ , \tag{2.73}$$

with n the refractive index of the etalon, and θ_t the angle of the transmitted wave. The intensity pattern of the transmitted I_t wave compared to the incident wave I_i is determined by the concentric interference, and is given by [27]:

$$\frac{I_t}{I_i} = \frac{T^2}{1 - R^2 - 2R\cos(\theta_t)} , \tag{2.74}$$

with reflectance R and transmittance T of the plane mirrors, for which $T + R = 1$. The relative irradiance of the fringe interference pattern is written as [27]:

$$\frac{I_t}{I_t|_{\text{max}}} = \mathcal{A}(\theta) . \tag{2.75}$$

Peaks in transmission occur at specific phase differences $\delta_{\text{max}} = 2\pi\beta$, with β the order of resonance. The irradiance halves at $\delta = \delta_{\text{max}} + \delta_{1/2}$, yielding sharp fringes. The half-width γ of a transmission peak is characterised by [27]:

$$\gamma = \frac{2T}{\sqrt{R}} . \tag{2.76}$$

The free spectral range of the etalon, as is derived in reference [27]:

$$\delta\omega = \frac{2\pi c}{2nd} . \tag{2.77}$$

Since d is fixed, $\delta\omega$ is the selected frequency range. By placing multiple etalons with different thicknesses behind one another, the range selection decreases substantially, possibly going into narrow-band mode. [26, 29]

Diffraction Grating - Frequency Tuning

Diffraction occurs for an obstructed wave, altering the amplitude or phase of the wave. Diffraction is characterised by a superposition of a large number of waves. In the case of a diffraction grating, the superposed waves are obstructed by an array of N diffracting elements, periodically distributed with length a apart. Each of these elements creates their own Fraunhofer diffraction pattern. In this work, a reflection phase grating is used (see figure 2.5). [27, 29]

A laser emits coherent light, such that the diffracted waves constructively interfere. For constructive interference, the optical path length difference δr equals a multiple of the wavelength $m\lambda$. This results in the relation [29]:

$$a\sin(\theta) = \delta r = m\lambda . \tag{2.78}$$

The multiple m is the so-called order of the principal maxima. Using a diffraction grating yields a laser that continuously changes laser frequency when the angle of the diffraction grating is continuously changed.
Interference between adjacent slits is not exactly constructive, such that the contributions of $N - 1$ neighbouring slits leads to an intensity that goes to zero fast (see figure 2.6). Increasing the number of slits results in sharper maxima, which are separated by $N - 1$ minima.

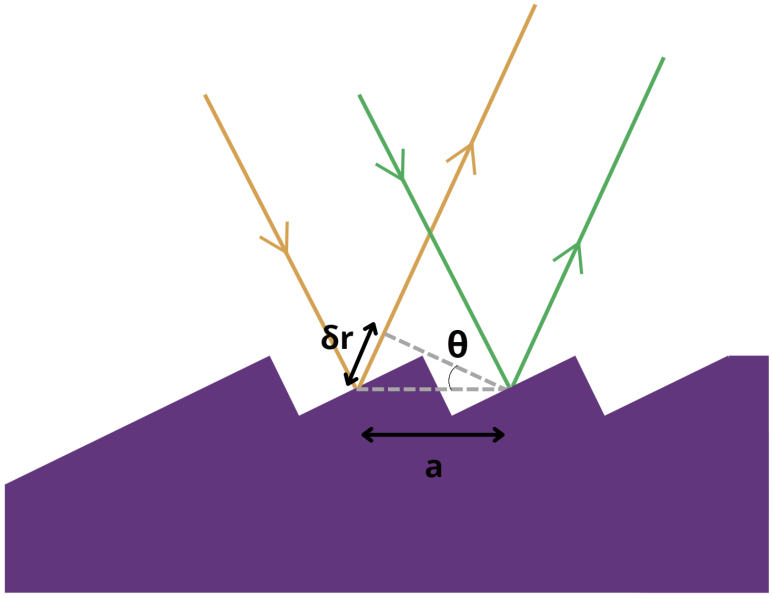

Figure 2.5: *Schematic representation of a reflection phase grating. The diffraction grating consists of different diffracting elements. The reflected waves constructively interfere according to equation 2.78. Figure adapted from [27].*

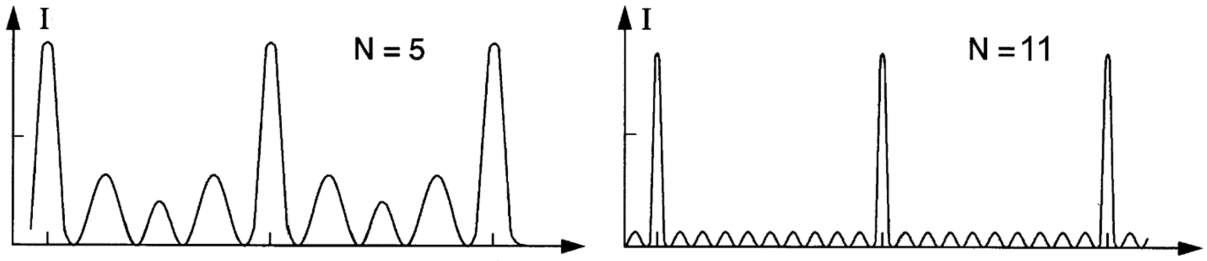

Figure 2.6: *Typical intensity pattern of waves reflected of a diffraction grating with multiple slits N. The maxima are separated by $N-1$ minima, and get sharper for increasing N. Figure adapted from [28].*

The linewidth of the laser using a diffraction grating is given by [30]:

$$\frac{\lambda}{\Delta\lambda} = mN \ . \tag{2.79}$$

In reality, the pattern is the convolution of a cosine and sinc function as a result of overlapping effects of diffraction and interference of the diffracting elements. Consequently, the maximum at $m = 0$ has highest intensity. The intensity of the peaks decreases for increasing principal maxima. For a mathematical description on the intensity, see references [27–29]. [29]

2.3.3 Ionisation Mechanisms

The energy at which a valence electron is no longer bound is called the ionisation energy or the ionisation potential (IP). Laser ionisation is either resonant or non-resonant. Moreover, laser ionisation only takes place if two constraints are satisfied. A first constraint for ionisation stems from a minimum saturation of the ionisation level. That is,

the interacting photons must exceed the rate of spontaneous emission A_{12} [31]:

$$\sigma_i(\lambda)\phi > A_{12} \ , \tag{2.80}$$

with $\sigma_i(\lambda)$ the cross section of ionisation at wavelength λ and ϕ the photon flux. This condition is also called the flux condition. A second condition for ionisation, also known as the fluence condition, states that sufficient photons are used for excitation if [32]:

$$\sigma_i(\lambda)\psi\tau_l > 1 \ , \tag{2.81}$$

with ψ the fluence of photons and τ_l the laser pulse length. For resonant ionisation, the laser frequency matches the transition energy between two levels of the atom at frequency $1/\lambda = \frac{E_2 - E_1}{hc}$. Typical values for the resonant ionisation cross section are of the order of [32]:

$$\sigma_{\text{resonant}} \approx 10^{-14} - 10^{-10}\text{cm}^2 \ . \tag{2.82}$$

On the other hand, non-resonant ionisation induces a transition into the continuum for a frequency $1/\lambda > \frac{E_{\text{IP}}}{hc}$. The cross section is typically lower than for resonant ionisation, and is of the order of [32]:

$$\sigma_{\text{non-resonant}} \approx 10^{-19} - 10^{-17}\text{cm}^2 \ . \tag{2.83}$$

Therefore, a higher photon flux is required for non-resonant ionisation compared resonant ionisation. Resonance ionisation is favourable, as it offers an improved detection efficiency along with isomeric selection. In some cases, additional resonant steps are necessary to reach above the ionisation potential. Increasing the number of resonant steps has the advantage that it increases the selectivity[4] by the product of each transition, thus reducing contamination further. Hence, even if the IP is reached with only two steps, it can be favourable to increase the number of steps anyway.

A laser impinging on an atom results in the absorption of the laser photon. Different mechanisms can be used to laser ionise an atom (see figure 2.7). Resonant ionisation uses auto-ionising states or Rydberg states to match the laser frequency to. Non-resonant ionisation is done into the continuum. In some cases, it is preferred to use multiple lasers. In those cases, a first laser brings the atom in an excited state to subsequently be ionised by a second or even third laser. In this case, the respective laser frequencies match the transition energies of successive energy levels in the atom of interest.

Rydberg states

Electronic energy levels converge to the ionisation limit as principal quantum number $n \to \infty$ according to equation 2.29 (see section 2.1.1). Those high energy levels that

[4]The maximum selectivity S before mass separation depends on the radiation line width Γ and the spaning between absorption lines due to the isotope shift $\Delta\omega_{12}$, and is given by [31]:

$$S = \left(\frac{\Delta\omega_{12}}{\Gamma}\right)^2 . \tag{2.84}$$

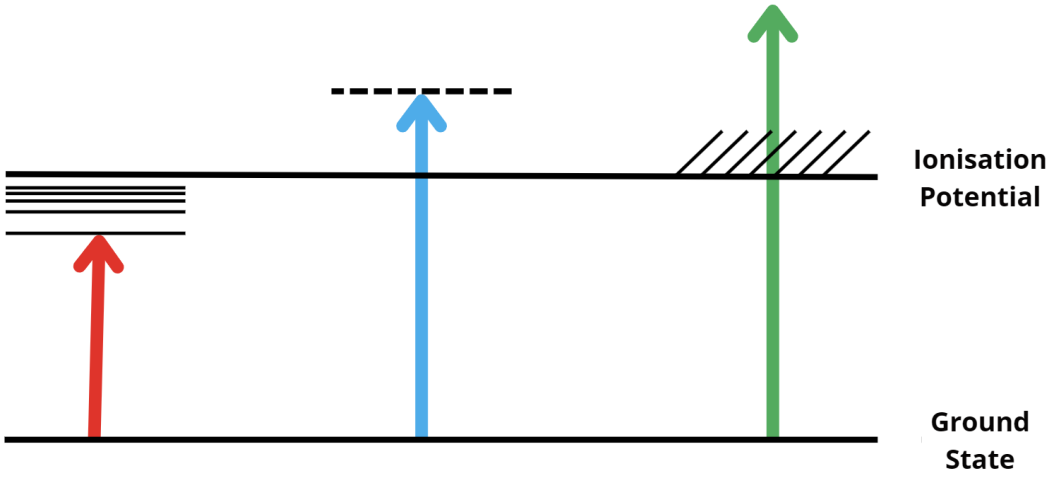

Figure 2.7: *Laser ionisation occurs in three ways. Either the laser brings the valence electron into a Rydberg state (red) where the atom subsequently gets ionised through field or surface ionisation. Or the excitation and ionisation goes via an auto-ionising state (blue) above the ionisation potential. A last possibility is to non-resonantly ionise the atom into the continuum using a high power laser (green).*

are still below the ionisation potential are called the Rydberg states with energy E_n. Since they are still below the IP, photon absorption still occurs. Each orbital angular momentum l defines its own converging series, called a Rydberg series. For higher n, Rydberg states become less resolved. [17, 22]

However, an atom with multiple valence electrons has multiple ionisation limits. As the atom ionises, the ion can undergo subsequent ionisation with its own ionisation potential. This creates multiple Rydberg series originating from subsequent ionisations of multiple valence electrons. If these multiple Rydberg series occur in the same energy region, even though they converge to different IPs, they can interact. Moreover, this interaction leads to energy shifts of the individual IPs. [17]

Once the atom is in a Rydberg state, ionisation can spontaneously occur from external effects such as field ionisation, collisional ionisation or blackbody radiation. [32]

Auto-ionising states

Some neutral atoms can be excited to a state above first ionisation potential, called auto-ionising states (AIS). Two simultaneous excited electrons, for which each energy state is below the IP, interact. If the total excitation energy is above the IP, the interaction leads to an energy transfer, resulting in ionisation. A quantum mechanical description of the interaction is found in references [17, 22]. [32]

Non-resonant into continuum

The continuum stems from the solution of radial function of the wave equation for $r \rightarrow \infty$. It is generated from all positive energy states possible for the electron. However, the low cross sections indicate that high laser power is needed to comply with the saturation conditions. For more details on the continuum, see references [17, 22, 32].

2.4 Nonlinear Optics

To generate a laser with a higher frequency, nonlinear optics are introduced. Nonlinear optics occurs when an impinging wave on a medium induces nonlinear electron elongations in the atomic system. This response of the medium is the so-called susceptibility χ, which is related to the induced polarisation $\vec{P}$ due to these elongations. For nonlinear optics, this susceptibility is no longer linearly related to the electric field $\vec{E}$. The resulting polarisation becomes [27]:

$$\begin{aligned} P(t) &= \epsilon_0 \left[\chi^{(1)} \vec{E}(t) + \chi^{(2)} \vec{E}^2 + \chi^{(3)} \vec{E}^3 + \dots \right] , \\ &= P^{(1)}(t) + P^{(2)}(t) + P^{(3)}(t) + \dots . \end{aligned} \tag{2.85}$$

As higher order susceptibilities are smaller, nonlinear optics requires a high $\vec{E}$-field to take place. Only then do higher order polarisations intensities play a dominant role. Consequently, the field of nonlinear optics only grew after the discovery of the laser, which produces high intensity $\vec{E}$-fields. The nonlinear terms of equation 2.85 start for a order of $\alpha \geq 2$. For a detailed description of nonlinear optics and the different effects, see references [17, 28, 33]. This work utilises harmonic generation specifically as a nonlinear optical effect. [16, 17, 27]

2.4.1 Harmonic Generation

Harmonic generation is the process in which a laser beam with frequency ω_{laser}, is directed into a nonlinear medium and is transmitted out of the medium with frequency $\alpha\omega_{\text{laser}}$ (see figure 2.8). The process is derived from equation 2.85 by writing it in the frequency domain as [17]:

$$\begin{aligned} P_l(\omega_i)/\epsilon_0 = {} & \chi^{(1)}_{lm} E_m(\omega_i) \\ & + 2\chi^{(2)}_{lmn}(\omega_i;\omega_j,\omega_k) E_m(\omega_j) E_n(\omega_k) \delta(\omega_i;\omega_j+\omega_k) \\ & + 6\chi^{(3)}_{lmno}(\omega_i;\omega_j,\omega_k,\omega_h) E_m(\omega_j) E_n(\omega_k) E_n(\omega_k) E_o(\omega_h) \delta(\omega_i;\omega_j,\omega_k,\omega_h) \\ & + \text{Higher } E_i \text{ terms} + \text{Terms involving magnetic field} + \dots , \end{aligned} \tag{2.86}$$

with l, m, n, o Cartesian coordinates and δ the Dirac delta. Second harmonic generation (SHG; $\alpha = 2$), is explained by the second term of equation 2.86 when $\omega_i = \omega_j + \omega_k \rightarrow 2\omega = \omega + \omega$ such that the susceptibility becomes $\chi^{(2)}_{lmn}(2\omega;\omega,\omega)$. This is interpreted as an absorption of two photons with frequency ω resulting in the emission of one photon with frequency 2ω (see figure 2.8). Analogous, third harmonic generation (THG; $\alpha = 3$) is given by the third term of equation 2.86, with $\omega_i = \omega_j + \omega_k + \omega_h \rightarrow 3\omega = \omega + \omega + \omega$, fourth harmonic generation (FHG; $\alpha = 4$) by the fourth term etc..

In the case of SHG, neglecting higher order terms ($\alpha > 2$) and introducing a lightwave of the form $E = E_0 \sin(\omega t)$, equation 2.86 is rewritten as:

$$P_l(\omega)/\epsilon_0 = \chi^{(1)}_{lm} E_m(\omega) + 2\chi^{(2)}_{lmn}(2\omega;\omega,\omega) E_m(\omega) E_m(\omega), \tag{2.87}$$

$$= \chi^{(1)}_{lm} E_{0,m} \sin(\omega t) + 2\chi^{(2)}_{lmn}(2\omega;\omega,\omega) E^2_{0,m}(1 - \cos(2\omega t)) . \tag{2.88}$$

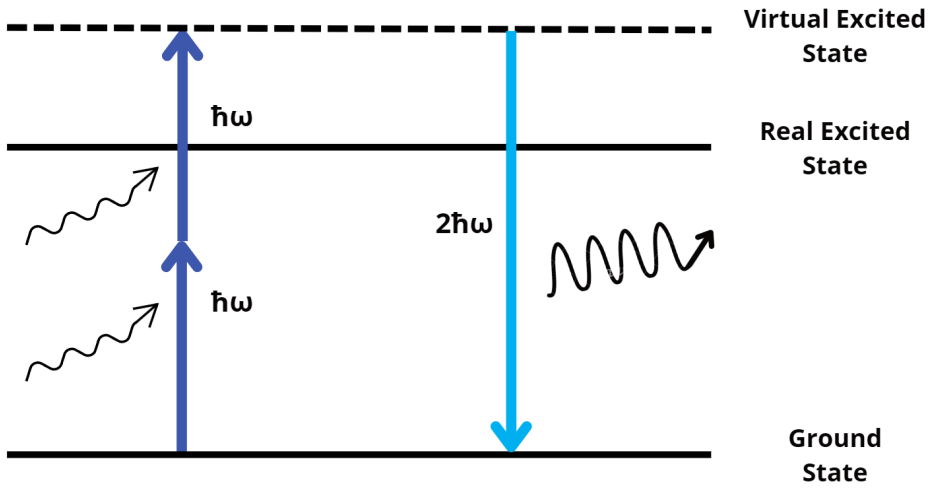

Figure 2.8: *Schematic representation of second harmonic generation quantum mechanically. Incoming laser light is subject to nonlinear optics inside a medium in which the outgoing light is frequency-doubled. Figure adapted from [17].*

Hence, the polarisation contains both a linear and nonlinear term with frequency ω, which translates to the medium transmitting both waves with frequency ω and 2ω, respectively. They propagate through the medium with propagation vector k_ω and $k_{2\omega}$, respectively. The wave with frequency ω is called the fundamental. The intensity of the wave with frequency 2ω, the so-called second harmonic, is proportional to the intensity of the incident wave with $I(2\omega) \sim I^2(\omega)$. [16, 27]

The induced nonlinear polarisation $P^{\text{NL}}(\alpha \geq 2)$ obtained from equation 2.86, acts as a driving force in the wave equation. It is produced by an ensemble of coherent osillating dipoles, spatially separated by distance d. The second harmonics generated at different positions in the medium, propagate through the medium with a phase difference $k_\omega d$. Due to the frequency dependence of the refractive index, the fundamental and the refractive index propagate at different phase velocities. Hence, even though the ensemble of dipoles is coherent, the second harmonics generated at different position interfere periodically, alternating between destructive and constructive interference. This limits the SHG conversion efficiency. By making a configuration such that the fundamental and second harmonic propagate with the same phase velocity, only constructive interference occurs. This is also called the phase-matching condition in SHG. [17, 27]

2.4.2 Phase-matching

The irradiance of the second harmonic generated inside a medium with thickness l^{NL} is determined by the interference of multiple second harmonics generated at different places in the crystal. The irradiance resulting from this interference is given by [27]:

$$I(2\omega) \sim \frac{\sin^2\left((n_\omega - n_{2\omega})l^{NL}k_\omega\right)}{(n\omega - n_{2\omega})^2}\,, \tag{2.89}$$

which yields a maximum intensity for the coherence length $l^{NL} = l_c$ [27]:

$$l_c = \frac{1}{4}\frac{2\pi}{k_\omega |n_\omega - n_{2\omega}|} \ . \tag{2.90}$$

For normal dispersion, the refractive indices $n_\omega \neq n_{2\omega}$, such that the maximum irradiance is expected for a crystal thickness smaller than the coherence length. However, by using a birefringent nonlinear crystal it is possible to obtain index-matching for $n_\omega = n_{2\omega}$. This results in an infinite coherence length, or also constructive interference for any crystal thickness.

The refractive indices are related to the phase through the wave vector [28]:

$$n_\omega / c = k_\omega / \omega = v_{phase} \ . \tag{2.91}$$

Hence, to obtain phase-matching, the wave vectors need to relate as:

$$2k_\omega = k_{2\omega} \ . \tag{2.92}$$

For phase-matching to occur, the phase velocities of the fundamental and the second harmonic must be equal. Index-matching, and so phase-matching, is achieved with birefringent nonlinear crystals that are cut at the proper angle, and oriented correctly relative to the incident laser beam. [17, 27, 28]

In summary, nonlinear optics allow for efficient doubling of the frequency, giving a broader spectral range while keeping the same experimental setup.

2.5 Applications of Resonance Laser Ionisation

Resonance laser ionisation's main application at a Isotope Separator On-Line (ISOL) facility is the production of radioactive ion beams. Additionaly, it is also used to investigate the nuclear structure using laser spectroscopy. A short summary on the applications is presented here. For more information on how resonance laser ionisation is used, see references [6, 8, 15, 31, 32].

2.5.1 Production

Using a laser ion source in an ISOL facility results in an efficient and element-selective ionisation. It reduces isobaric contamination as the isobars are not resonantly ionised by the laser, due to having different energy levels compared to the isotope of interest. This reduces background signal and lowers the radioactive load at the mass separator. RILIS is also a tool for beam diagnostics, as the isotope of interest is easily identified by blocking a laser beam, as for no laser the ion signal is decreased. Additionally, the laser is protected from the hostile target environment while the ionisation region is simple and robust. Resonance ionisation laser ion source also achieves isomer-selective ionisation for some isotopes. [15, 32]

New concepts of laser ion sources have been developed, depending on the application

of the RIB. An ion source for highest selectivity includes trapping (LIST), which confines the ions using a radiofrequency quadrupole ion guide. Another example is the hybrid plasma-laser ions source VADLIS, which gives an increased efficiency. The purity needed of specific isotopic beams generates conditions on the laser scheme, while the efficiency depends on the wavelength and minimum power of the laser system. [15]

2.5.2 Spectroscopy

By measuring the spectrum of a laser ionised beam, model-independent information on the hyperfine structure is deduced. Information on the magnetic dipole moment μ and the quadruple moment Q_s can be found from the distance between the spectral peaks. Systematic trends along an isotopic chain of a particular element is also measured using laser spectroscopy. An example of such trend across an isotopic chain is the the change of charge radii $\delta\langle r^2\rangle$. [31, 34]

Laser spectroscopy techniques are typically categorised into resonant ionisation spectroscopy, trap-assisted spectroscopy and collinear beams. Because of the differences in chemistry and atomic properties between elements, no general method can be applied across the periodic table. More information on the spectroscopy techniques is found in reference [31].

To measure a hyperfine spectrum, the transition has to be sensitive to it, also the electron orbit has to be affected by the nuclear magnetic moment. The electron orbit that experiences the biggest influence from the nucleus, is the s-orbit, as they lie closest to the nucleus. Therefore, to measure the hyperfine structure, the laser scheme has to have a first excitation step with a transition of the electron from an s- to another orbit, ideally s-to-p.

2.6 Lanthanides

The elements ranging from lanthanum (La) to lutetium (Lu) can be grouped together as the lanthanides. The lanthanide region spans from atomic number 57 to 71, containing 15 elements. They are characterised by electrons occupying the $4f$ orbital (see figure 2.9), and by generally being more chemically reactive than transition metals. Overall, lighter lanthanides are more abundant than heavier lanthanides[5], as well as lanthanides with even atomic number are more abundant than those with odd atomic number[6]. [35]

The first lanthanide La has electronic configuration [Xe]$6s^2 5d^1$, as it is favourable to have an empty $4f$. For higher atomic number, $4f$-orbitals are filled which results in lanthanide contraction[7] as they become more stable than $5d$-orbitals. Ce has electron configuration [Xe]$6s^2 5d^1 4f^1$, where $4f$-orbitals have not contracted sufficiently to

[5] This results from how elements are created in the universe. Heavier elements are more difficult to create as they require higher pressures and higher temperatures. [35]

[6] Odd Z-elements have a larger neutron capture cross section. Hence, they are more likely to take up another neutron, becoming less common. Even Z-elements are generally more stable when formed. [35]

[7] The $4f$-orbitals contract, penetrating the Xe core. Hence, $4f$-orbitals present core-like behavior, as they don't take part in bonding. [23]

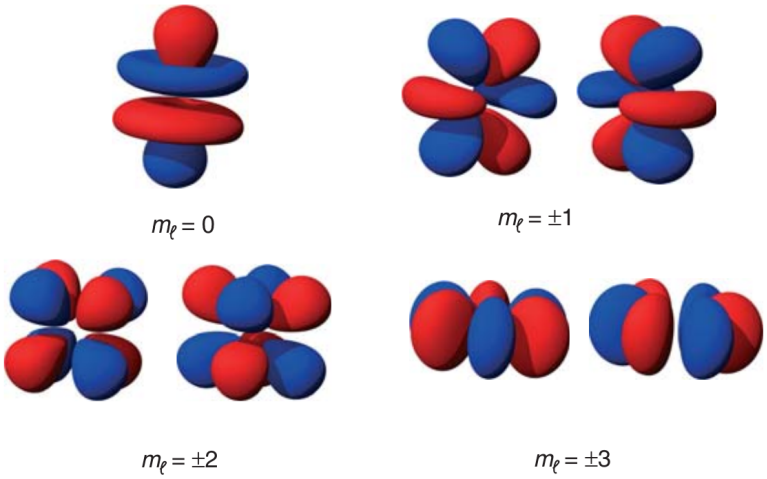

Figure 2.9: *Representation of f-orbitals with their associated magnetic quantum number. Figure obtained from [23].*

have electron energy lower than that of the $5d$-electrons. From praseodymium on, the lanthanides follow the pattern for electron configurations of [Xe]$6s^2 4f^n$ until europium. After Eu, the half-filled f-subshell becomes stable, such that the next electron is added to the $5d$-orbital. However, the lanthanide pattern is resumed with terbium until the last lanthanide Lu with electron configuration [Xe]$4f^{14}5d^1 6s^2$.
Because of lanthanide contraction, $4f$-orbitals do not take part in chemical bonding. Consequently, the $5d$- and $6s$- valence electrons determine the chemical and physical behavior of the element. As a result, for a chemical process that doesn't involves changes in the number of f-electrons, the lanthanide series all display similar chemistry. Additionally, for the ionisation of lanthanides, electrons are first removed from $6s$- and $5d$-orbitals. [23, 35]

The lanthanide contraction causes $4f$-orbitals to contract before the bonding region of the atom. As a result, no covalent overlap is possible for lanthanides, except for Eu and Ce. Besides, lanthanides also do not posses the right symmetry for such overlap. Consequently, high and low oxidation states are not possible for lanthanides, with their most stable chemical state being the $+3$ oxidation state. $4f$-orbitals are embedded within the $5s$ and $5p$ core, which also shields them from coordination chemistry. On the other hand, the inner $4f$-orbitals poorly shield the outer electrons from the nuclear charge. As a result, the atomic radii contract for higher effective nuclear charge, decreasing the relative ionic radius for heavier lanthanides. Although the lanthanides are chemically similar, subtle changes arise because of the ion size.
The valence $5d$- and $5s$-electrons form a conduction band, together with a $4f$-electron. Accordingly, the $+3$ oxidation state is most common for lanthanide elements, and is justified by stabilisation obtained from interactions of triply charged ions. However, for some lanthanides, additional $4f$-electrons are donated as it leads to a (half-)filled f-orbital. Consequently, the $+2$ and $+4$ oxidation state also occurs for those elements, as is the case for Eu, Sm and Ce. This difference in oxidation state is the main contribution to the differences in physical chemistry between the lanthanides. [23, 35]

The crystal field theory is a necessary addition to the Hamiltonian (see section 2.1), to

accurately predict the energy levels of lanthanides. Remark that crystal field splittings are very small, of the order of 100 cm^{-1}, and therefore are treated as a perturbation. Another important corrective term includes configuration interactions between configurations of the same parity. This configuration interaction is accounted for through electrostatically correlated magnetic interations. For additional corrections made to the effective Hamiltonian, see reference [24]. The electronic energy levels are calculated by diagonalising the effective Hamiltonian with a free-ion basis. The result is a rich atomic structure with complex electronic configurations. [24, 35]

Spectroscopic and magnetic properties of the lanthanides are determined by the f-orbitals, and thus are uninfluenced by the environment. Luminescence spectroscopy is a technique to study the energy level scheme of a lanthanide ion. Resulting from the selection rules (see section 2.2.2), d-d and f-f transitions are forbidden, while f-d transitions are allowed. However, the forbidden f-f transitions can occur because of symmetry breaking in free ions of lanthanides. Furthermore, besides electric dipole transitions, also magnetic dipole moment transition[8] need to be taken into account. The magnetic dipole transitions follows different selection rules as previously described. A difference is that inner subshell transitions are allowed, although they have weaker intensities. Moreover, magnetic dipole transitions are parity-allowed, allowing intra-configurational transitions. A third transition mechanism that has to be considered, are electric quadrupole transitions. The so-called hypersensitive transitions are sensitive to changes in symmetry and strength of the ligand field. As a result they obey the selection rules of quandrupole transitions, yielding them peuso-quadrupole transitions. However, in general, a lanthanide transition contains only contributions of the electric dipole and magnetic dipole. Additional effects on the configuration include the ligand-field interactions and induced electric dipole interactions, see references [23, 36]. [23, 24, 35, 36]

[8] Magnetic dipole transitions are related to the rotational movement of the electron as opposed to the translational movement of the electron under the electric field. [23]

Chapter 3

RILIS as Experimental Setup

The combination of successive steps for laser ionisation is called a laser scheme. The laser scheme is experimentally investigated using lasers and a detection system. This chapter gives an overview of the experimental setup of RILIS at ISOLDE in section 3.1. Additionally, details are provided on how the Photo-Ionization Spectroscopy Apparatus (PISA) is used as a detection system in section 3.2. Furthermore, in this thesis only Ti:Sa lasers are used, thus a description of a Ti:Sa laser is offered in section 3.3.

3.1 RILIS

ISOLDE's ionised radioactive beam can be contaminated by isobars. By utilising the unique atomic structure of each element, the specific element is extracted, creating a beam with a higher degree of purity. This idea lies at the basis of RILIS. Hence, with the need of a beam of high purity, the majority of the ion beams produced at the ISOLDE facility at CERN, make use of RILIS. In 2023, RILIS was involved in up to 65% of the experiments which were performed in ISOLDE that year [37]. For more detailed information regarding the development and current operation of RILIS, see references [8, 15, 37].

Each atom has a unique electronic structure with unique energy levels (see section 2.1). Tunable lasers are set to match the energy difference of the transition levels of the atom of interest. This resonantly excites and eventually ionises that specific atom (see section 2.3.2). The uniqueness of the energy levels of the atom of interest makes excitation via resonance with lasers very selective. During ionisation, the isobaric contaminants remain unaffected, as the laser frequency does not match their energy levels. The selectivity increases for additional excitation steps (see section 2.3.3). The excitation and ionisation using lasers, results in RILIS being a highly efficient ion source as well. [8, 10, 37, 38]

Isotopes created during the nuclear reactions in the target effuse into the ion source. The ion source is the region in which the laser-atom interactions physically occur (see figure 3.1). It is a refractory metal tube, typically made of Ta, Re or W, with a diameter $d = 3$ mm and length $L = 34$ mm. This tube gets resistively heated to a temperature around $T \approx 2000$ °C, creating a confining potential and improving the extraction efficiency of the ion source [15].

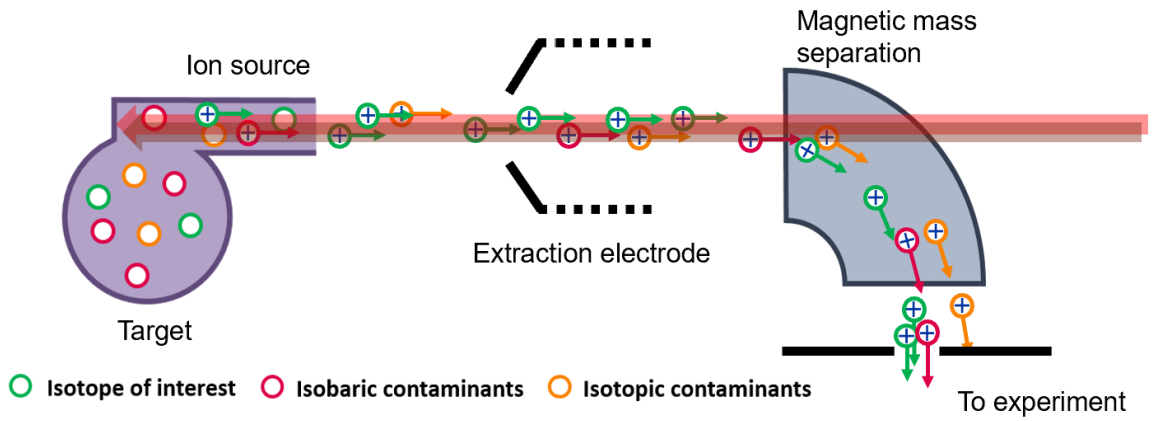

Figure 3.1: *Schematic overview of laser ionisation process of RILIS when used on-line. A laser is directed into the ion source where it will resonantly excite and ionise target isotopes. The laser ions are extracted and directed into a separator magnet. In the separator magnet isotopic contaminants are filtered out based on there charge-to-mass ratio. The remaining ions are transported to the experiment. Figure obtained from reference [37].*

Lasers are directed into the ion source where they resonantly ionise the isotopes of interest. Due to the resistive heating of the ion source, a longitudinal electric potential is induced, accelerating the ions towards the extraction electrode. However, the high resistive heating induces surface ionisation of atoms with a low ionisation potential. These surface ions are the main source of isobaric impurities. The degree of surface ionisation α_s depends on temperature T according to the Saha-Langmuir equation [15]:

$$\alpha_s = \frac{g_i}{g_0} \exp\left(\frac{\phi - E_{\mathrm{IP}}}{k_B T}\right) , \tag{3.1}$$

with g_i, g_0 the statistical weights of the ionic and atomic ground states, respectively, and ϕ the work function.

The laser setup of ISOLDE's RILIS consists of four titanium:sapphire lasers, three dye lasers, two neodymium-doped yttrium orthovanadate (Nd:YVO) lasers and three neodymium-doped yttrium aluminum garnet (Nd:YAG) lasers (see figure 3.2). The lasers have a repetition rate of 10 kHz, which matches the mean residence time of the atoms in the ion source. By using nonlinear optics for harmonic generation (see section 2.4), a total spectral range of $210 - 950$ nm is covered by the RILIS setup. Depending on which part of the range is operated, a different type of laser setup is used. To determine which to use, typically, the laser with the highest power output is set up, as is deduced from the tuning curves of RILIS (see figure 3.3). However, this power condition is not always necessary, so the laser setup is evaluated according to the requirements of the experiment. [8, 15]

Another important use of RILIS is for laser spectroscopy (see section 2.5.2). There is a longstanding experimental campaign to measure the isotope shifts and hyperfine structure of long isotopic chains with extremely sensitive in-source laser spectroscopy [8, 15].

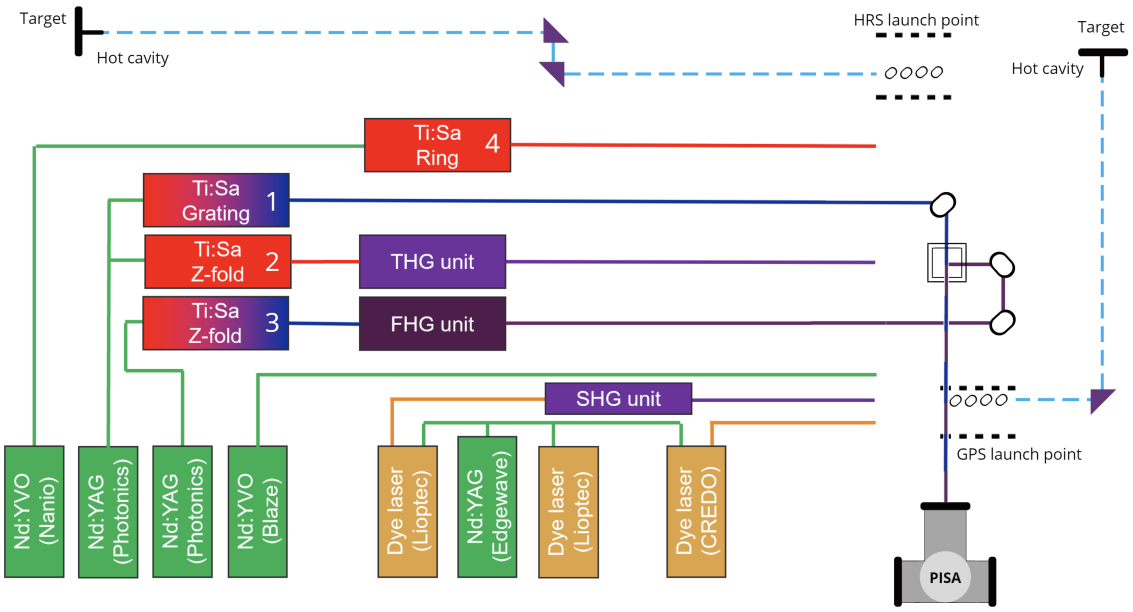

Figure 3.2: *A schematic representation of the laser setup at RILIS. There are four Ti:SA lasers which are pumped by either a ND:YVO or ND:YAG laser. Also three Dye lasers are present which are pumped by an ND:YAG laser. The model of the laser is given in brakets. Using harmonic generation, a spectral range of* $210 - 950$ *nm is covered with this laser setup. Next to the laser setup is also a reference area where the PISA, is installed. By utilising optical elements such as mirrors and beamsplitters, lasers light reaches either the GPS launch point, HRS launch or the atomic beam unit. Figure adapted from reference [37].*

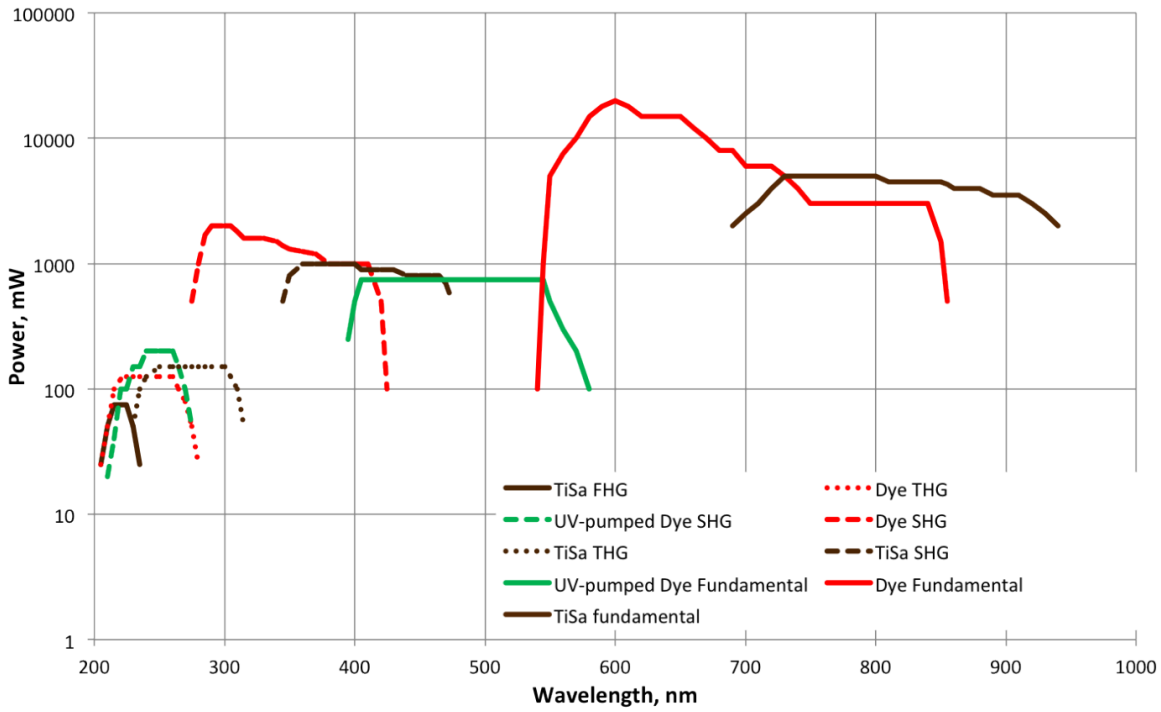

Figure 3.3: *Tuning curves of the RILIS lasers. Depending on the range needed for the experiment, different lasers are set up. The laser setup is based on the highest power output of the needed range. Figure obtained from reference [32].*

3.2 PISA

The Photo-Ionization Spectroscopy Apparatus is a compact atomic beam unit (ABU) at RILIS (see figure 3.4). It allows for utilisation the laser setup of RILIS without being on-line. Hence, it can be used for optimisation, ionisation scheme development, or as a reference cell, as explained in detail in references [39, 40]. The PISA was developped by T. Kron for his doctoral thesis [39] and was first put to use in reference [40].

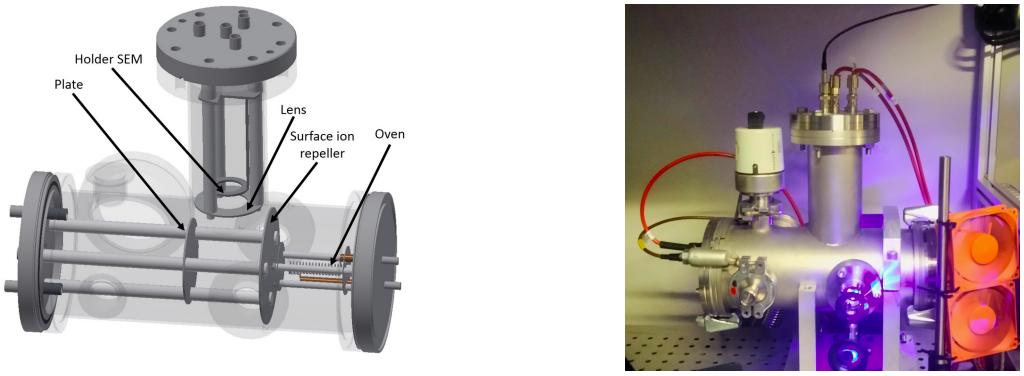

(a) (b)

Figure 3.4: *Comparison of schematic representation and picture of PISA as used in RILIS (a) Schematic representation of PIS as developed in the doctoral thesis of T. Kron, with indications of all important components. Figure obtained from reference [39]. (b) Picture of PISA in use at RILIS.*

The PISA generates an atomic beam of a desired element by evaporation. This atomic vapour is irradiated resonantly by the lasers. The resonance signal of the laser ions is detected by the secondary electron multiplier. In absence of a resonant signal, the background is measured arising from surface ions and electrons. The apparatus is put in vacuum to pressures of the order of $\sim 10^{-6}$ mbar. This also reduces the background signal as the heat transfer to the restgas is negligible. [39]

The different components of the PISA include an oven, electrodes and a detection system. These different components are described below.

3.2.1 Oven

The front side of the PISA consists of three rods between which the sample with desired element is placed (see figure 3.5). The sample is inside a small capillary tube usually made out of graphite. For lanthanides however, a tantalum tube has to be used instead of graphite, as the lanthanides chemically react with the carbon of the graphite oven. The tube is inserted in an oven, held in place by a stainless steel plate. Above this plate is another stainless steel plate with a small hole. This second plate already slightly collimates the atomic beam coming out of the oven.

A coil sits around the capillary tube without making contact with it. This coil is resistively heated. Consequently, the oven is heated from the radiative heat of the coil around it, such that the sample inside the oven evaporates into an atomic beam. To increase the

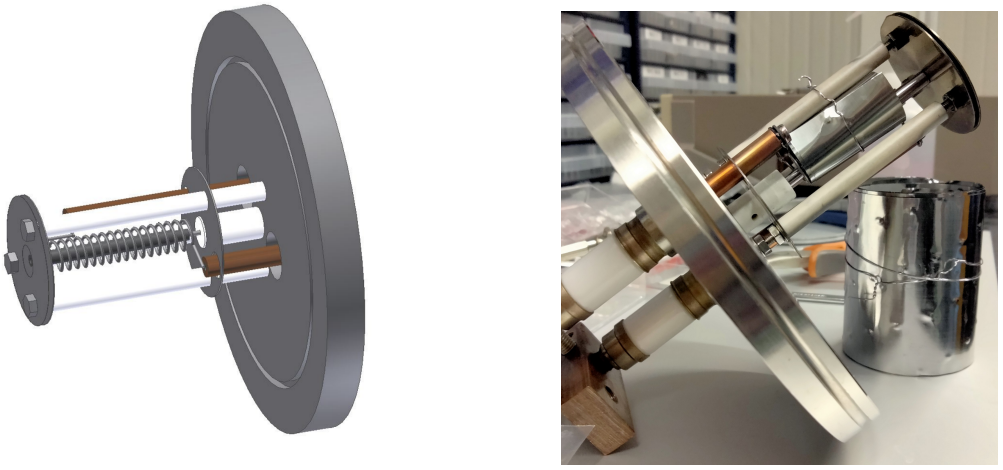

(a) (b)

Figure 3.5: *Side by side comparison of scheme of oven of PISA and how it looks in reality. (a) Schematic representation of oven of PISA as was developed in the doctoral thesis of T. Kron. Figure obtained from reference [39]. (b) Picture of the oven with a molybdenum heat shield around the oven and coil to increase the radiative heat to the sample.*

efficiency of radiative heating, a molybdenum heat shield is put around the coil. For the sample to evaporate, the oven needs to be heated up to around 1000 °C, depending on the vapour pressure of the element inside. The temperature calibration of the apparatus is done using a pyrometer in reference [40], and is given by:

$$T[°C] = 52[°C/\mathrm{A}] \cdot T[\mathrm{A}] + 236[°C] \ , \tag{3.2}$$

with A denoting the current on the coil in Amperes. The temperature calibration was done without a heat shield, so the actual temperature of the oven with a heat shield is higher. A new calibration should be done using a thermocouple. However, with the current design it is not yet possible to insert such a thermocouple. To ensure that the PISA does not melt, it should not be heated higher than 20 A or 1300°C. To reach higher temperatures, an additional cooling system should be designed.

Since the oven has to reach high temperatures to evaporate the sample, a lot of surface ions are created. Besides the surface ions, a lot of ionic electrons are present inside the PISA, which typically have a high energy. When these electrons collide with the remaining atomic vapour inside the PISA, they create secondary ions. Both the surface ions as well as the ions created by the electrons are detected, increasing the background signal. Therefore, to reduce the background signal, the surface ions and electrons are deflected from the line of sight of the detector by the electrodes.

3.2.2 Electrodes

The electrodes of the PISA consist of two plates and a repeller (see figure 3.6). The two plates are held up by rods, the repeller is attached to one of the plates, being insulated from each other. To deflect the surface ions and electrons, voltages are applied on the

plates and repeller. The background contributors have higher energy for higher temperatures. Hence, for an element that requires high temperatures to become vapour, higher energetic background particles require a higher voltage on the plates to be deflected. The voltages are adapted based on the output signal.

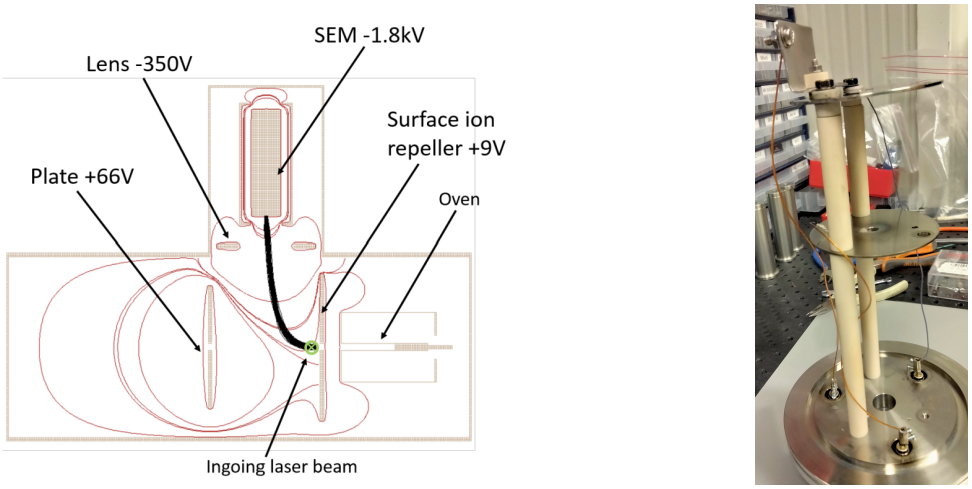

(a) (b)

Figure 3.6: *(a) Simulation on the trajectories of ions inside PISA. The red lines represent the electrode potential lines and the black line the resulting path of the ions to go into the detector. Figure obtained from reference [40]. (b) Picture of back flange with electrodes. The two plates and repeller are put under voltage to deflect electrons and surface ions.*

3.2.3 SEM

The detection system of the PISA is a secondary electron multiplier (SEM). The ions impinging on the detector, kick out electrons called the secondary electrons. The average number of electrons emitted from one single incident ion is called the secondary emission coefficient η. A voltage is applied to the detector, accelerating the secondary electrons into an electron multiplier. The secondary electrons are accelerated towards a metal electrode with high η, creating more electrons that are emitted. The final detected charge q depends on the number of metal electrodes m in the multiplier with M the magnification factor [16]:

$$q = Me = \eta^m e \ , \tag{3.3}$$

with e the elementary charge. The output of the SEM is a current given by:

$$I(t) = \frac{MNe}{\tau_s} \exp\left(\frac{-t}{\tau_s}\right) \ , \tag{3.4}$$

with τ_s the decay constant of the multiplier, N the number of ions. [16, 41]

The PISA is used without any mass separation. Hence, the background signal cannot be identified. Moreover, the signal obtained from an atomic sample is the linear combination of all isotopes in that sample in their natural abundance. The only mass selection while using the PISA occurs through the use of RILIS lasers.

3.3 Titanium:Sapphire Laser

A titanum:sapphire (Ti:Sa) laser is a four-level laser that uses a titanium-doped sapphire (Ti^{+3}:Al_2O_3) crystal as active medium (see figure 3.7). This crystal is cut at Brewster's angle[1], and is optically pumped by a pumping laser. The pumping laser is directed by two planar mirrors into a focusing lens. The focused laser beam propagates through a semi-transparent mirror and irradiates the crystal. The population inversion inside the crystal results in amplified light through stimulated emission (see section 2.3). The emitted photons propagate inside a Fabry-Pérot resonator with curved mirrors, called the cavity. The frequency selective Lyot filter and Fabry-Pérot etalon inside the cavity determine the laser frequency (see section 2.3.2). The end mirror of the cavity is an output coupler, which transmits some light for the laser beam.

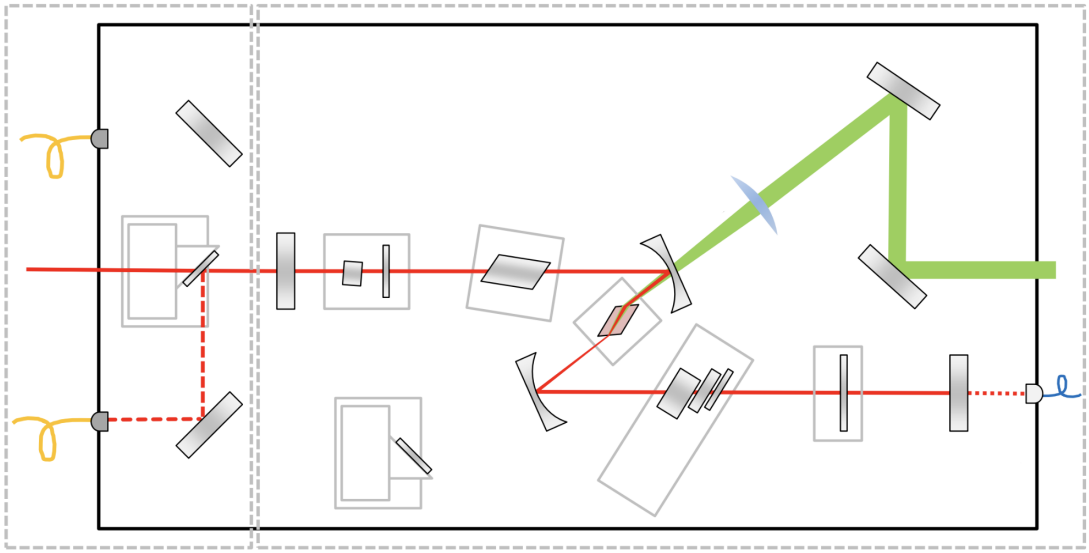

Figure 3.7: *Schematic representation of a Ti:Sa laser. An initial laser is shone in and reflected by two mirrors after which it is focused through a lens on a Titanium-doped Sapphire crystal. Because of the population inversion created inside the crystal, a photon field is emitted inside the Z-cavity. The frequency selective Lyot filter and etalon determine the laser frequency. The cavity is optimised by the position of the curved mirrors until it lases. The laser is then coupled out and transported to the experiment. Figure adapted from reference [42].*

Ti:Sa lasers as used in RILIS, are designed with a Z-cavity based on the design from Mainz [43]. The different Ti:Sa lasers are pumped by Nd:YAG Photonics lasers. The output power of a Ti:Sa laser increases for a better aligned laser. Alignment of the laser is done by optimising the position and angle of all optical elements inside the cavity.
A second type of laser used at RILIS is called a grating Ti:Sa. In case of a grating Ti:Sa, a set of prisms and a diffraction grating are added into the Z-cavity. This so-called prism beam expander, changes the beam shape to a horizontal line. The tailored beam shape lessens the power impinging on the diffraction grating as well as increases the number of slits used of the diffraction grating. More grating slits used, results in a smaller

[1] The light impinging at Brewster's angle, is reflected polarized. More on this process is found in reference [27].

linewidth of the eventual signal (see section 2.3.2), which is favoured. The diffraction grating rotates to change the angle of incidence of the impinging laser beam, which results in a reflected beam with a different frequency.

The fundamental lasing range of a Ti:Sa laser at RILIS spans $700 - 950$ nm. By using harmonic generation, the lasing range of the Ti:Sa increases (see figure 3.3). Examples of nonlinear birefringent crystals used for the nonlinear optics are BiB_3O_6 (BIBO) and β-BaB_2O_4 (BBO). More details on the Ti:Sa lasers used at RILIS are found in reference [8, 15, 30, 37, 43, 44].

In this work, Ti:Sa 1 and Ti:Sa 3 are the used lasers from the RILIS setup (see figure 3.2). Ti:Sa 3 is a standard Z-fold Ti:Sa (see figure 3.8), while Ti:Sa 1 is a grating Ti:Sa (see figure 3.9). The Z-fold Ti:Sa is set at the resonance frequency of the first excitation step. For laser scheme development Ti:Sa 1 is set up as a second step such that it scans across the ionisation potential. The scan is done by changing the angle of the diffraction grating continuously. However, changing the angle of incidence, also changes the response of the nonlinear crystal. To account for this scanning range in harmonic generation, the temperature of the nonlinear crystal is changed. The refractive index of such crystal is related to temperature, as determined in references [45, 46]. The nonlinear crystals are put in a crystal oven. The changing temperature of the crystal oven is controlled via the 'Master puppet' software written by Cyril Bernerd. It uses information on the grating position, power output and wavelength to adjust the temperature. The adjusted temperature of the crystal oven changes the refractive index. In turn, the adjusted refractive index ensures phase-matching (see section 2.4.2).

Once the wanted laser frequency is obtained, the laser beam is transported to the experiment. This is done using a combination of a telescope, mirrors and beamsplitters. The laser beams are spatially and temporally overlapped. The focus and wavelengths are optimised on the ion signal. From the signal of the scan, Rydberg states or autoionising states are extracted, and the laser scheme is finalised. More on laser scheme development in chapter 4.

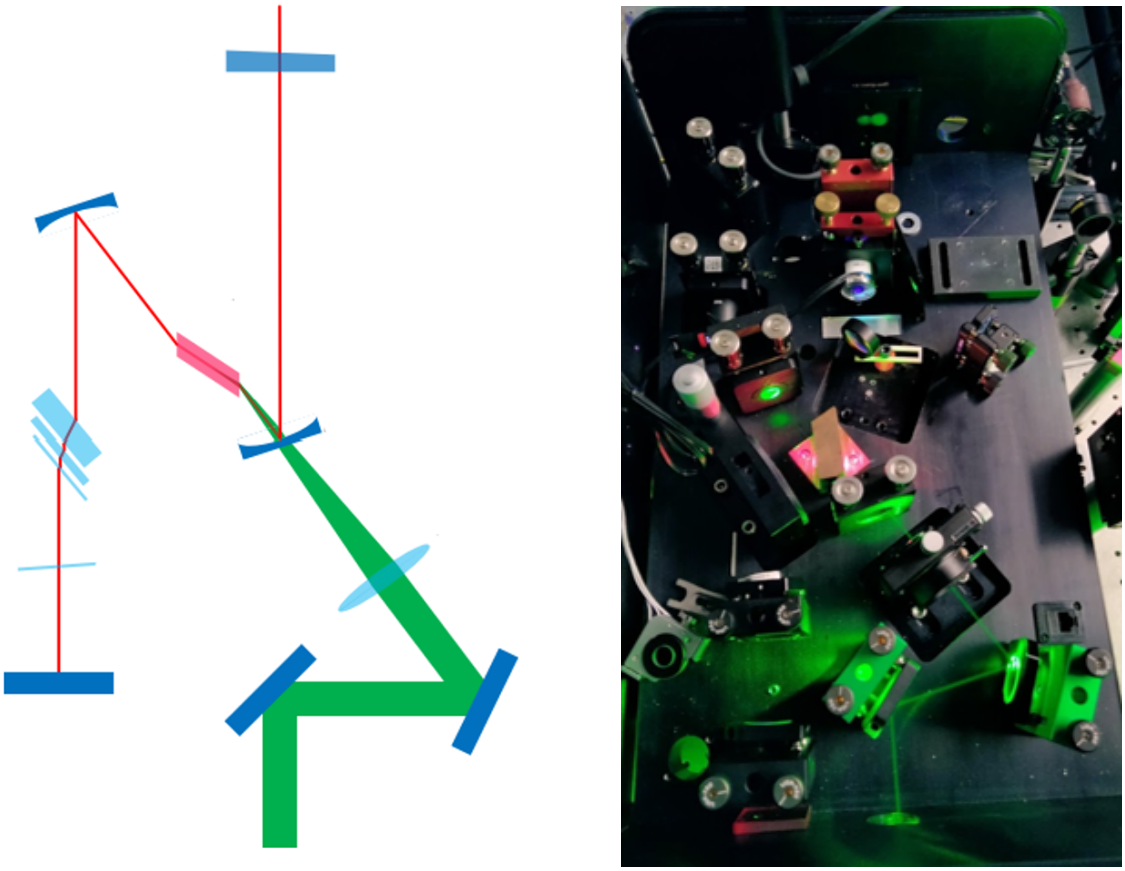

(a) (b)

Figure 3.8: *(a) A schematic of a Z-fold Ti:Sa used in RILIS. A pumping laser creates population inversion in the Ti^{+3}:Al_2O_3 crystal. Stimulated emission generates a photon field that oscillates in the Z-cavity between mirrors. A lyot filter and etalon are added for frequency selection. Figure obtained from reference [47]. (b) Picture of Z-fold Ti:Sa taken in RILIS, CERN.*

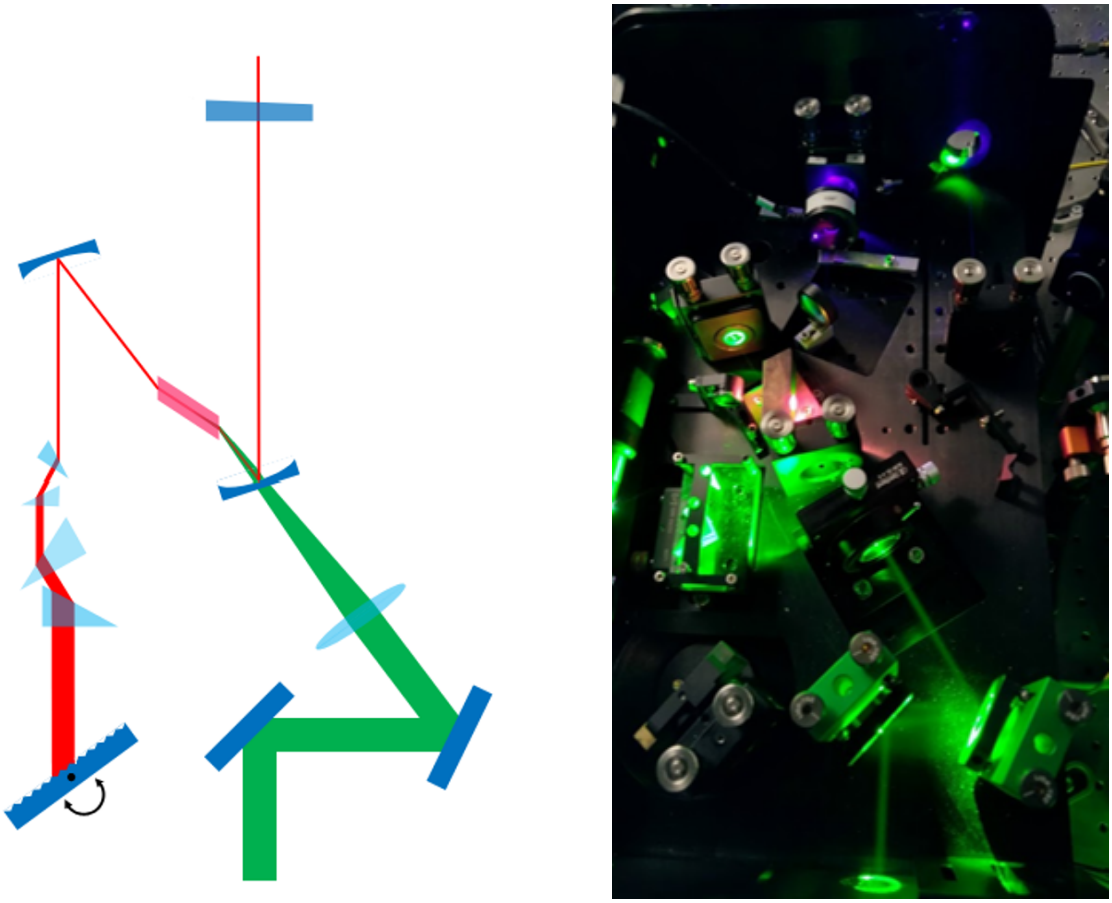

(a) (b)

Figure 3.9: *(a) A schematic of a grating Ti:Sa used in RILIS. The photon field oscillating in the Z-cavity travels through a beam expander, to create a horizontal beam shape. This increases the number of slits of the diffraction grating irradiated, improving the generated signal linewidth. The diffraction grating turns to change the angle of incidence, resulting in a change in output frequency. Figure obtained from reference [47]. (b) Picture of grating Ti:Sa taken in RILIS, CERN.*

Chapter 4

Laser Ionisation Scheme Development

Resonance laser ionisation is used for either spectroscopy or production of RIBs. Depending on the application, different constraints are applied on the laser scheme for ionisation. For praseodymium, the goal is to use the scheme for spectroscopy, while for europium the scheme is developed to use for production. This chapter comprises the scheme developments, as well as an investigation of the ionisation potential of europium using the developed schemes.

Typically, a laser scheme development consists of three phases. For each successive excitation or ionisation step in the laser scheme, an iteration of the phases has to be done. More information on how a laser ionisation scheme is developed can be found in [48].

1. **Literature study**

   First, a literature study has to be conducted based on the information available in the different databases referenced in [49–51] . This consists of comparing all the known electron levels, to see which comply to the selection rules (see section 2.2.2). Hence, these are the only electron levels to which a transition with a laser can occur. From those that comply, only the ones that are within the obtainable range of the laser setup are considered. In case of RILIS, the wavelength of the transition between the levels has to be between $210 - 950$ nm (see section 3.1). Typically, steps within the Ti:Sa range are prioritised over steps in the dye range due to ease of setup and reduced maintenance. However, Ti:Sa lasers are only preferred as long as the laser ionisation efficiency is not compromised.
   Another criterion for a step in the laser scheme is based on the transition strength A, which is given in the Kurucz database in reference [51]. Typically, a transition strength of the order of 10^6-10^8 s^{-1} is prioritised to ensure level saturation. Using the electron levels that satisfy all criteria, a theoretical laser scheme is developed for further investigation.

2. **Scanning Setup**

   The theoretical laser scheme is investigated using an atomic beam unit. A sample of the stable isotope of interest is placed in an oven and heated to become atomic vapour. This vapour is hit with a laser at a specific wavelength resonant with the chosen excitation step, resonantly exciting the atoms. With a second laser and a diffraction grating, a scan is performed across the possible transitions

or ionisation potential. During this scan, the first laser remains at the specified wavelength. When the wavelength of the second laser equals the energy of a possible transition, a resonant ionisation increases the ion current.

3. **Saturation**

   In some cases, it is useful to know how the ion current changes with laser power. This saturation power gives an indication of the minimum power required without loss of efficiency, which then relates to the Einstein coefficient of the transition.

Additionally, efficiency measurements can be done to measure the combined efficiency of ionisation, extraction and release process. The absolute efficiency corresponds to the highest ion signal measured, which determines whether the ionisation scheme can be used at ISOLDE. On-line measurements have an increased efficiency of ionisation due to laser-atom overlap. However, to conserve resources, efficiency measurements take place in a simplified configuration. Hence, these efficiency measurements return relative efficiencies that serve as a lower limit of the ionisation efficiency. For this thesis it was not yet necessary to know the efficiency of the schemes and so their measurements remain for future work. Since the developed schemes are not used for operation, it is also not yet necessary to measure their saturation curves. [48, 52]

In this work, the laser scheme development is done using the PISA (see section 3.2). This atomic beam unit is used off-line. Therefore, no ISOLDE beam-time is necessary for laser scheme development and schemes can still be developed even when there are no protons available. Another advantage of working with PISA is that Doppler broadening[1] of the laser is reduced, as the laser is perpendicular to the atomic beam. Hence, the resolution of the setup increases compared to on-line measurements when the laser is collinear to the atom beam. If efficiency measurements are necessary or an exact yield has to be known, measurements have to be done on-line at one of the ISOLDE frontends, as the difference in geometry compared to the PISA influences the efficiency and yields.

4.1 Scheme Development of Praseodymium

At first instance, a laser scheme for praseodymium is studied. Praseodymium has atomic number $Z = 59$ and so is part of the lanthanides. The ground state of Pr has a total angular momentum $J = 9/2$, an electronic configuration of $4f^3 6s^2$ and a nuclear term $^4I°$ with odd parity. Not much is known about the nuclear structure of praseodymium, and what is known, is still inconclusive. To explore the nuclear structure of Pr with laser spectroscopy, a new laser scheme has to be established.

The developed laser scheme would preferably only use Ti:Sa lasers, and would use a transition that allows for the examination of the nuclear structure (see section 2.5.2). For the transition to be sensitive to the hyperfine structure, the electron should transition from an s-shell to another shell, as these transitions experience the largest effect

[1] Other broadening mechanisms contain collision broadening or saturation broadening. In case of a collinear setup, they will also have an increased effect. More details on their influence on the lineshape and origin can be found in reference [25].

from the nucleus and often display large hyperfine splitting. For this reason, levels of unknown electronic configuration are not considered for the scheme development.

The extended limitations on the possible energy levels because of the required Ti:Sa-range, as well as the need for a known electronic configuration, put additional constraints on the literature study of the possible electron levels. Unfortunately, there are only very few transition strengths known of the electronic levels of praseodymium. Hence, this criterion for A was kept in mind, but levels with unknown transition strength were still considered. The first step transitions chosen to investigate are given in table 4.1, which also gives the ground state in bold.

Table 4.1: *Chosen first step levels for laser ionisation scheme of praseodymium together with the ground state in bold. The different columns represent the total angular momentum of the state J_{upper}, the difference in angular momentum with the ground state ΔJ, the energy of the first step in inverse centimetres E, the wavelength WL, the energy from the first step to the ionisation potential in inverse centimetres and in nanometres, and the transition strength A.*

Configuration	J_{upper}	ΔJ	E[cm^{-1}]	WL[nm]	To IP[cm^{-1}]	To IP[nm]	A[s^{-1}]
$\mathbf{4f^36s^2}$	$\mathbf{9/2}$		$\mathbf{0}$		$\mathbf{44120}$	$\mathbf{226.65}$	
$4f^36s6p$?	$7/2$	-1	21513.28	464.83	22607.72	442.33	$1.565E^{+7}$
$4f^36s6p$?	$7/2$	-1	21565.83	463.70	30688.48	443.36	$4.302E^{+7}$

A first Ti:Sa laser is operated at fundamental 10782.92 cm^{-1} with SHG using a BIBO crystal cut at Brewster angle of 157°(see section 2.4), to reach the energy level of 21565.84 cm^{-1}. Subsequently, a grating Ti:Sa is set up at fundamental 11285 cm^{-1} with SHG to return 22570 cm^{-1}, so it may reach above the IP. Even though the oven was heated up to 20 A, no signal was seen. The hypothesis is that, with how the heat shield and coil are set up, a cold spot arises at the end of the tip of the oven. This causes the Pr to condensate before it gets out of the oven. To remedy this, a new oven with a longer coil and more insulating heat shield was designed by the ISOLDE workshop. This new setup is verified with another laser scheme for Pr known to work, but that is not sensitive to the hyperfine structure. However, the verifying signal is very faint, indicating that there is a large contribution of the background signal. In hope to decrease this background, the electrode positions were changed. This new configuration was tested and verified with a samarium (Sm) sample, as Sm is known to come out of the oven more easily and at lower temperatures. Alas, no praseodymium signal was found when the Pr sample was put back inside the oven, with either scheme of chosen first step. A possible explanation is that the PISA needs to be heated up to even higher temperatures to get Pr out. However, if even more current would be added to the coil, the risk of melting the apparaturs increases.

An alternative option to investigate the hyperfine structure of praseodymium would be on-line or by designing a cooling system for the PISA. However, both are not feasible within the timeframe of this thesis, and so remain for future work. Proceeding to higher atomic number, a laser scheme for europium is developed.

4.2 Scheme Development of Europium

Europium is a lanthanide with atomic number $Z = 63$. The ground state has angular momentum $J = 7/2$, an electronic configuration $4f^7 6s^2$ and nuclear term $^8S°$ with odd parity. The investigation of the ionisation potential for Eu started with the development of a laser scheme in the three phases previously explained. The goal is to develop a laser scheme that exclusively uses Ti:Sa lasers. Using this developed laser scheme, the ionisation potential is investigated and compared to the current literature value, as well as the methodology used to calculate it in reference [53].

Starting from the databases referenced in [49–51], a literature study is done, taking the Ti:Sa range of RILIS and the preferred transition strengths into account. The first steps for different theoretical laser schemes to investigate, are given in table 4.2. Both of these possible first steps require second harmonic generation. For the first laser scheme, a Z-fold Ti:Sa was set up at 10880.63 cm^{-1} which corresponds to 21761.26 cm^{-1} via SHG using a BIBO crystal at $160°$. Subsequently, the range between 12055 cm^{-1} and 11800 cm^{-1} is scanned in order to reach above the IP. The oven is heated to 14 A. This scan is done twice. Analogous, for the second laser scheme, the Z-fold Ti:Sa is set up at 10802.58 cm^{-1}, which corresponds to 21605.17 cm^{-1} with SHG and the same BIBO crystal. The grating Ti:Sa scans from 12080 cm^{-1} to 11800 cm^{-1}, with the oven also heated to 14 A. This scan is done three times in total. The different Rydberg scans can be found for scheme 1 and scheme 2 in figure 4.1 and 4.2, respectively.

Table 4.2: *Chosen first step levels for laser ionisation scheme of europium and the ground state of Eu in bold. The different columns represent the total angular momentum of the state J_{upper}, the difference in angular momentum with the ground state ΔJ, the energy of the first step in inverse centimetres E, the wavelength WL, the energy from the first step to the ionisation potential in inverse centimetres and in nanometres, and the transition strength A of the first step.*

Configuration	J_{upper}	ΔJ	E[cm^{-1}]	WL[nm]	To IP[cm^{-1}]	To IP[nm]	A[s^{-1}]
$\mathbf{4f^7 6s^2}$	$\mathbf{7/2}$		$\mathbf{0}$		$\mathbf{45734.74}$	$\mathbf{218.65}$	
$4f^7 6s6p$	$9/2$	1	21761.26	459.53	23973.48	417.13	$1.515E^{+8}$
$4f^7 6s6p$	$7/2$	0	21605.17	462.85	24129.57	414.43	$1.493E^{+8}$

From the data, the Rydberg states are identified. Each time the scanning Ti:Sa is at resonance with a Rydberg state, an increased ion signal is measured. Rydberg states converge to the ionisation potential (see section 2.3.3). Hence, closer to the ionisation potential, resonant peaks converge, until they can no longer be resolved.

The fact that europium is observed, while praseodymium is not, is explained by their physicochemical differences. Eu has both a $+2$ and a $+3$ oxidation state, while Pr only has a $+3$ oxidation state (see section 2.6). This makes Eu easier to work with as the chemistry is less limiting. Accordingly, Rydberg states of Eu are successfully measured and used for the investigation of the ionisation potential of Eu.

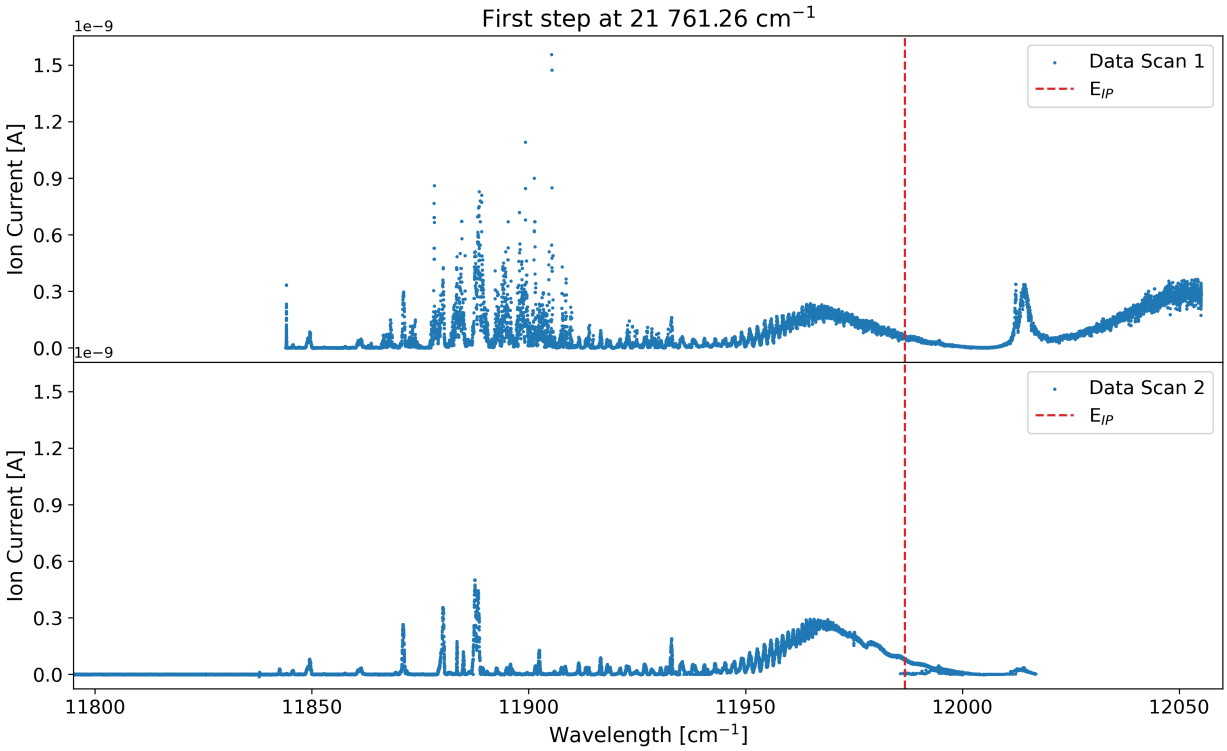

Figure 4.1: *The ion current is measured for the laser scheme that starts with a first step excitation to* 21761.26 *cm*$^{-1}$*. A grating Ti:Sa set up with second harmonic generation, scans a range starting below the IP en ending over the IP for a second ionisation step. Each time the grating Ti:Sa is in resonance with a Rydberg state, the ion current increases. In red dotted line is the current literature value for the ionisation potential. The scan is repeated twice.*

4.2.1 Fit of the Rydberg States

The next step of the analysis is the fit of the Rydberg series. The fitting is done using *scipy.curve_fit*, which is a non-linear least square fitting function [54]. The function returns the optimal values for the parameters that minimise the sum of the squared residuals, along with the estimated approximate covariance of the optimal parameter values. Each peak is fitted manually with a gaussian function. The individual fits are appended in the model, until the peaks can no longer be resolved, at which point the model is stopped.

The different fits with their respective residuals are depicted in figures 4.3, 4.4, 4.5, 4.6 and 4.7. The residuals shown are those within the range the peaks can be resolved, the fitted range. For the model to be a good fit, the residuals should be normally distributed around zero, otherwise part of the signal is not fitted. For the first scheme, the first scan shows large residuals compared to the signal in the wavelength region $11870 - 11910$ cm^{-1}, indicating that it is not well fitted. This is due to having more noise on the signal in that range and the amplitudes of the fit not going high enough. Since only the centroid of the fit is used, the fit is deemed sufficient for the purpose of this thesis. For the second scan of that same scheme, the residuals peak in the same region, with a too

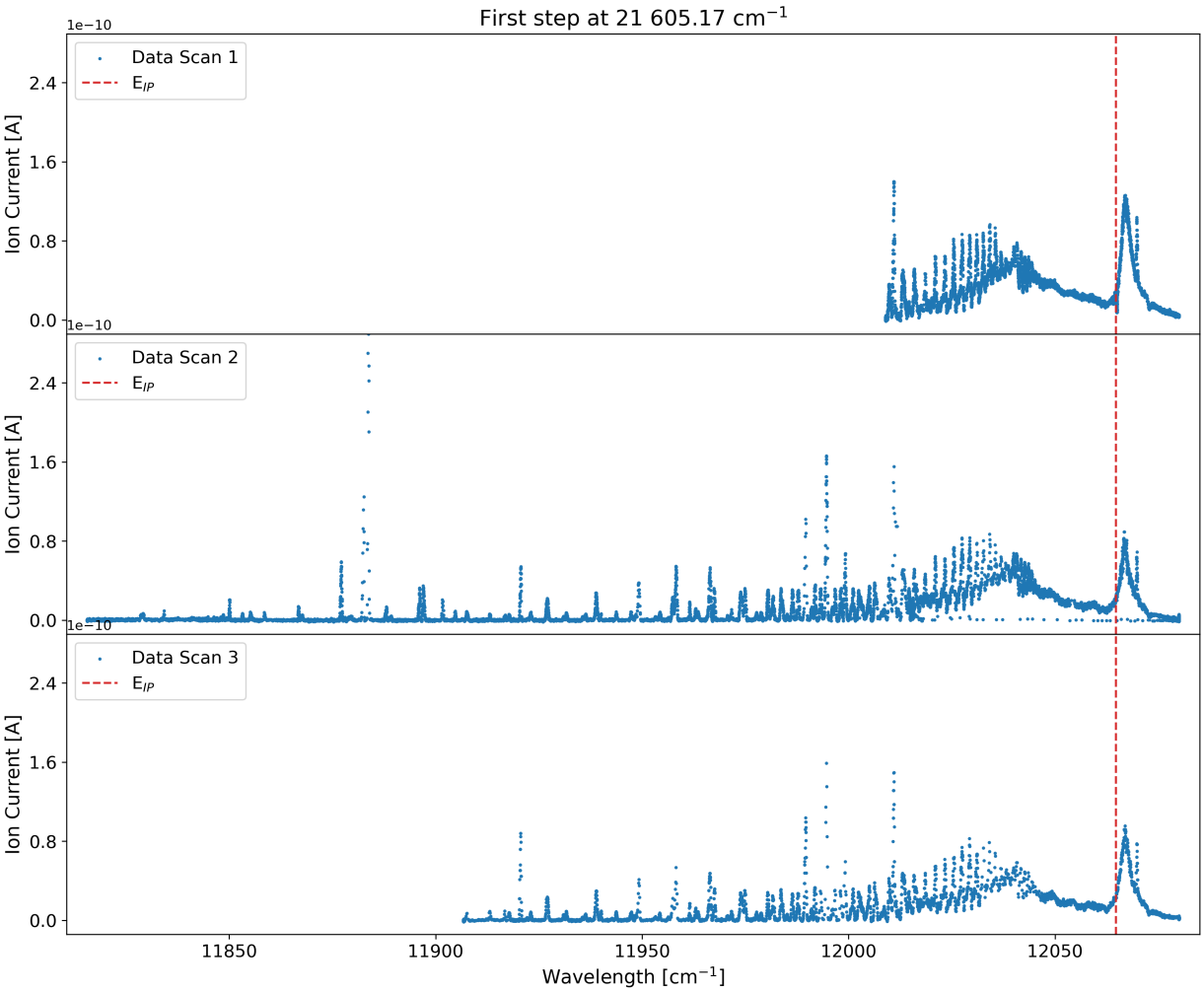

Figure 4.2: *The ion current is measured for the laser scheme that starts with a first step excitation to* 21605.17 *cm*$^{-1}$*. A grating Ti:Sa set up with second harmonic generation, scans a range starting below the IP en ending over the IP for a second ionisation step. Each time the grating Ti:Sa is in resonance with a Rydberg state, the ion current increases. In red dotted line is the current literature value for the ionisation potential. The scan is done three times. The different ranges are due to differences in when the data collection started relative to when the scan started.*

low amplitude of the fit. However, following the same reasoning for the first scan, only using the resulting centroids, the fit is sufficient. For the second scheme, the residuals are well distributed around zero, indicating an acceptable fit.

To finish the laser scheme development, the second laser step should be resonant with a scanned Rydberg state. At that state, the atom ionises through collisional energy, field ionisation or thermal fluctuation. The laser scheme is finalised once saturation and efficiency measurements are done. This finalisation remains as a future task for

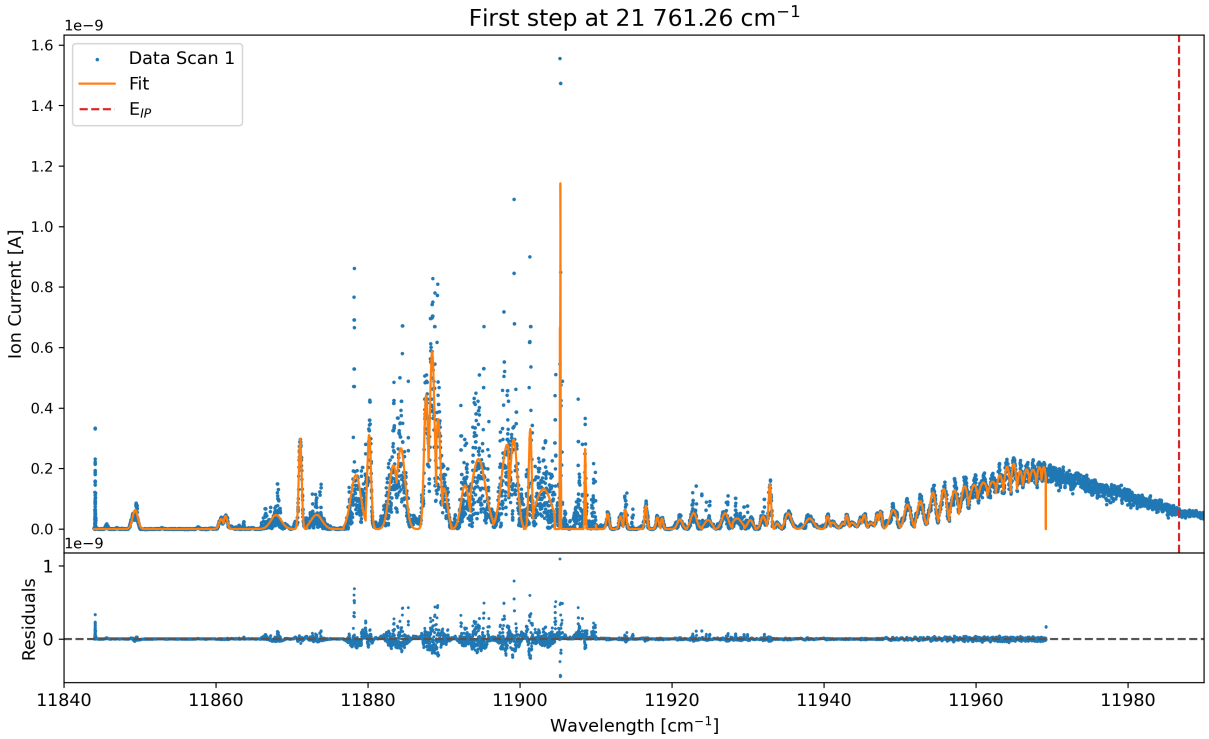

Figure 4.3: *Fit of the first Rydberg scan of the first scheme and its residuals. Each peak is fitted with a Gaussian, until the peaks can no longer be resolved. At that point the model is set to zero and the further data points are no longer used. The red dotted line represents the literature value of the ionisation potential. The corresponding residuals are shown for the fitted range*

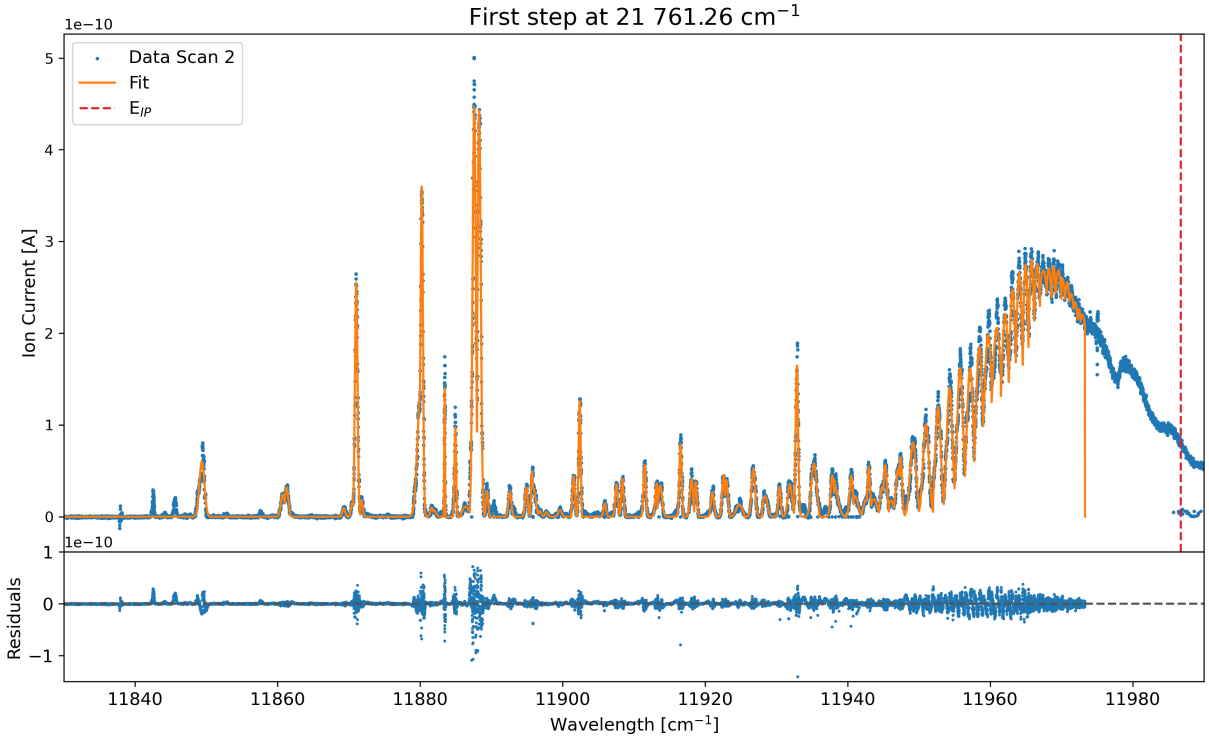

Figure 4.4: *Fit of the second Rydberg scan of the first scheme and its residuals. Each peak is fitted with a Gaussian, until the peaks can no longer be resolved. At that point the model is set to zero and the further data points are no longer used. The red dotted line represents the literature value of the ionisation potential. The corresponding residuals are shown for the fitted range.*

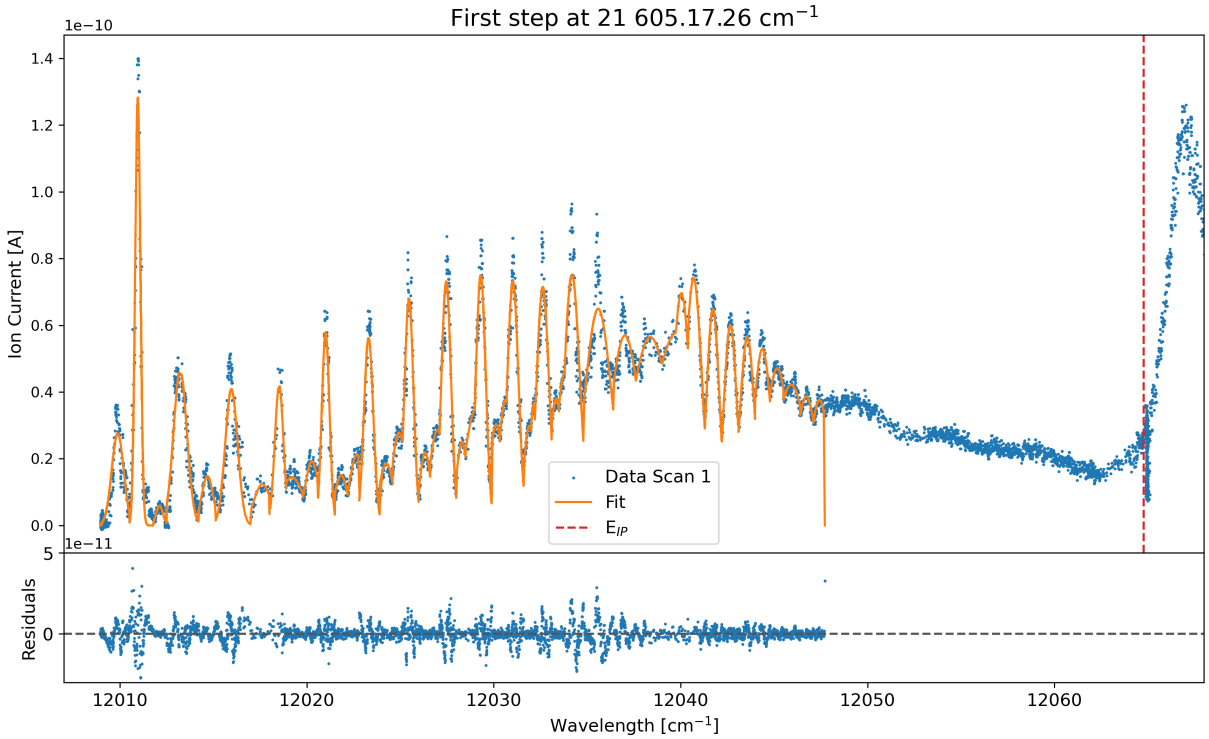

Figure 4.5: *Fit of the first Rydberg scan of the second scheme and its residuals. Each peak is fitted with a Gaussian, until the peaks can no longer be resolved. At that point the model is set to zero and the further data points are no longer used. The red dotted line represents the literature value of the ionisation potential. The residuals are shown for the range the peaks can be resolved, the fitted range.*

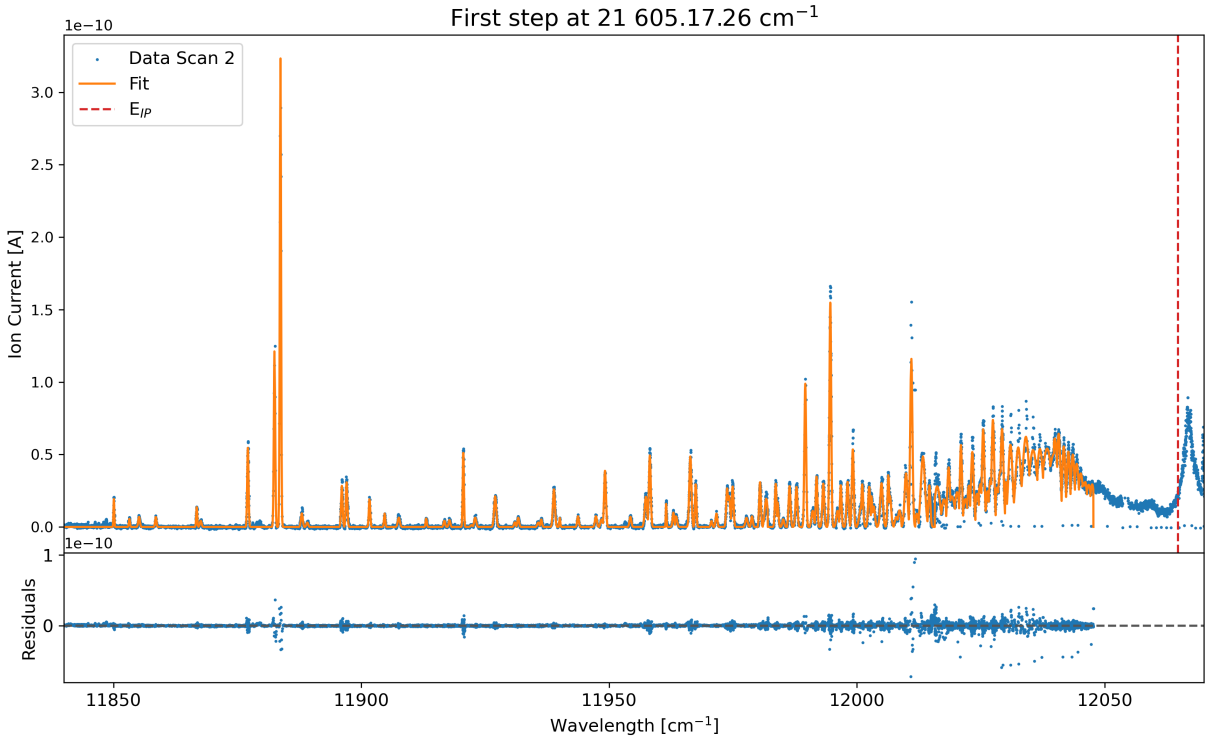

Figure 4.6: *Fit of the second Rydberg scan of the second scheme and its residuals. Each peak is fitted with a Gaussian, until the peaks can no longer be resolved. At that point the model is set to zero and the further data points are no longer used. The red dotted line represents the literature value of the ionisation potential. The corresponding residuals are shown for the fitted range.*

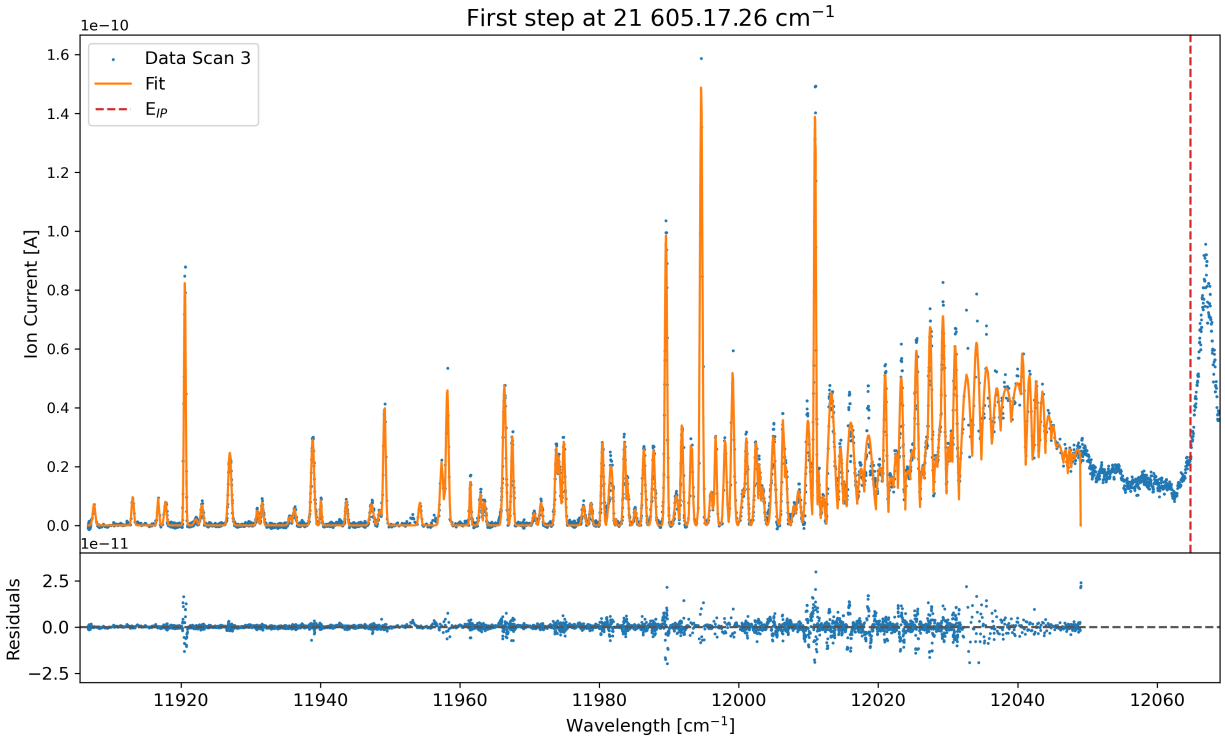

Figure 4.7: *Fit of the third Rydberg scan of the second scheme and its residuals. Each peak is fitted with a Gaussian, until the peaks can no longer be resolved. At that point the model is set to zero and the further data points are no longer used. The red dotted line represents the literature value of the ionisation potential. The corresponding residuals are shown for the fitted range.*

when the scheme would be used online, or compared to other available laser schemes for Eu.

4.2.2 Determination of the Europium Ionisation Potential

The centroid of the respective fits gives the energy of that specific Rydberg state. This value can be used to determine the effective principal quantum number by rewriting equation 2.29 to:

$$n^* = \sqrt{\frac{\mathcal{R}^*_{\text{Eu}}}{E_{\text{IP}} - E_n}}\,, \tag{4.1}$$

with $\mathcal{R}^*_{\text{Eu}}$ the mass corrected Rydberg constant for europium with value $\mathcal{R}^*_{\text{Eu}} = 109736.918$ cm^{-1} [53]. Initially, an estimate is given for the value of the ionisation potential. From the results, the principal quantum number is calculated from equation 2.28, knowing the theoretical values for the quantum defect. The theoretical values for the quantum defect are plotted in reference [55] and extracted for europium in reference [40]. The values for the quantum defect are given in table 4.3.

Table 4.3: *Theoretical values for the quantum defect, predicted in [55] and extracted specifically for europium in [40]. Each wave has a different quantum defect, which can be used to deduce the principal quantum number n knowing the effective principal quantum number n^*.*

Series	s-wave	p-wave	d-wave	f-wave
Quantum defect δ	4.24	3.75	2.78	1.00

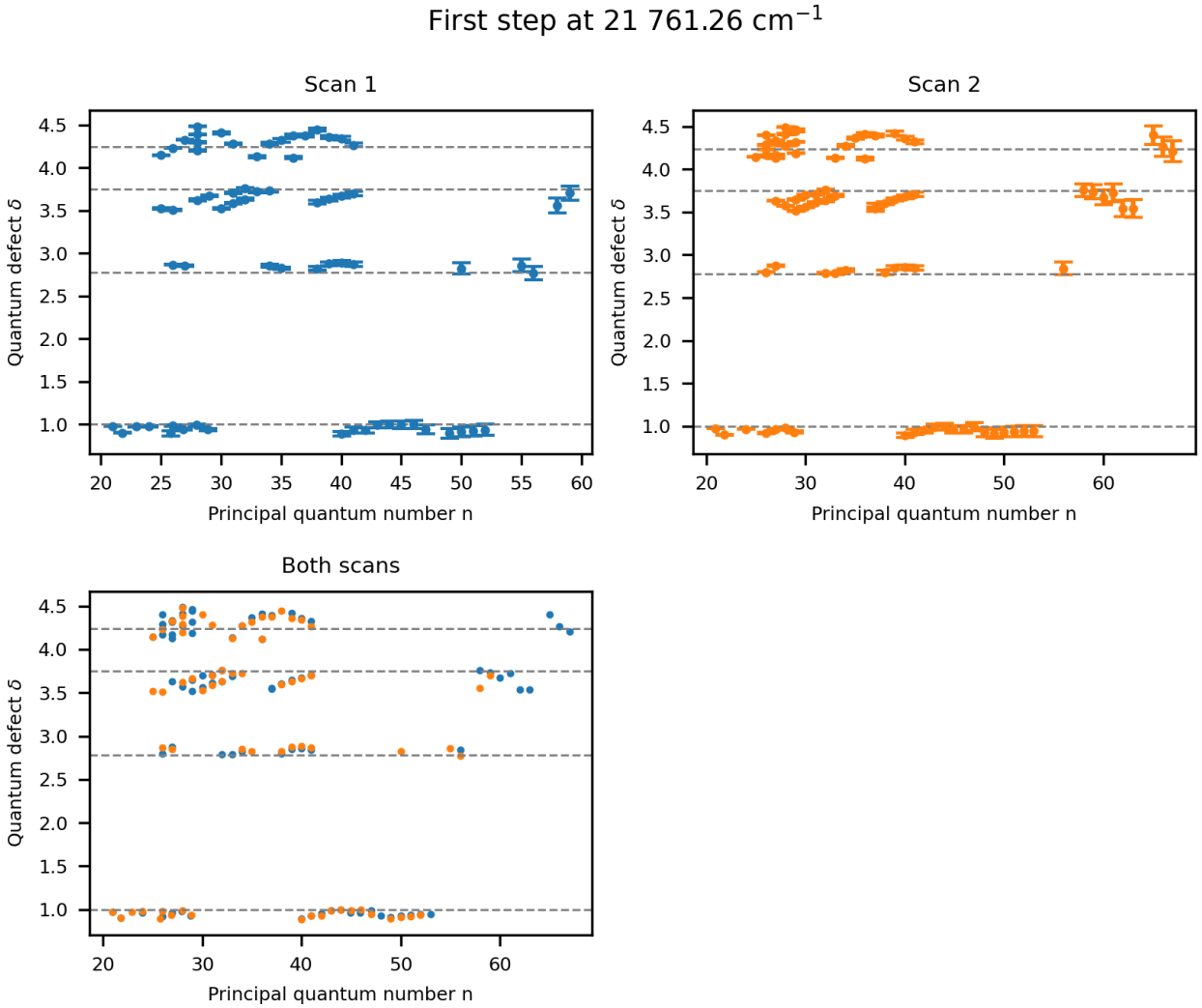

Figure 4.8: *Quantum defect δ as a function of principal quantum number n, which is an approximate constant relation. Each scan for the first scheme is plotted with its errorbars on δ, which increase for higher n due to more difficult to fit converging Rydberg peaks. The grey dotted line represent the theoretical values for δ. Both scans are also given in the plot below, showing their overlap.*

The uncertainty on the n^* is calculated according to [41]:

$$\Delta x(x_i) = \sqrt{\sum_i^n \left(\frac{\partial x}{\partial x_i}\right)^2 (\Delta x_i)^2}\,, \tag{4.2}$$

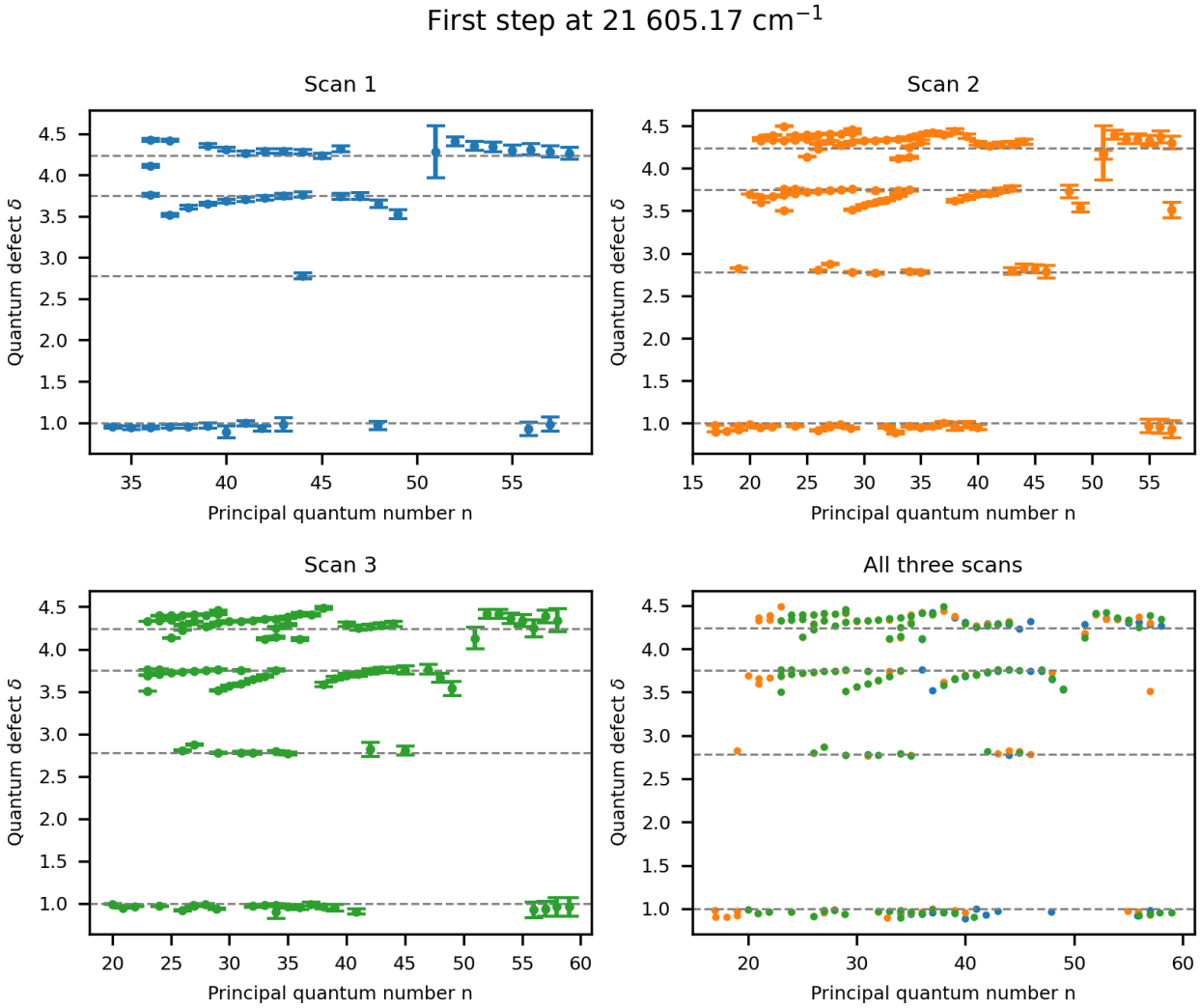

Figure 4.9: *Quantum defect δ as a function of principal quantum number n, which is an approximate constant relation. Each scan for the second scheme is plotted with its errorbars on δ, which increase for higher n due to more difficult to fit converging Rydberg peaks. The grey dotted line represent the theoretical values for δ. The first scan has a shorter range, due to starting the data collection later respective to start of the scan. All three scans are also given in the fourth plot, showing their overlap.*

with a number of n variables x_i. For n^*, the only effect on the uncertainty comes from E_n, as $\mathcal{R}^*_{\text{Eu}}$ is a constant without uncertainty from reference [53], and E_{IP} is an estimate value. The uncertainty on E_n has to take the uncertainty on the wavemeter $\Delta_{\text{WM}} = 0.03$ cm^{-1} into account. This systematic error is taken into account twice, once for the readout of the first step, and once for the readout of the scan. Additionally, due to the use of second harmonic generation, the uncertainties of both steps need to be accounted for twice. As a result, the uncertainty on E_n is given by:

$$\Delta E_n = \sqrt{(2\Delta_{\text{step 1}})^2 + (2\Delta_{\text{scan}})^2} = \sqrt{(2\Delta_{\text{WM}})^2 + \left(2\sqrt{\Delta^2_{\text{WM}} + \Delta^2_{\text{fit}}}\right)^2}\,. \tag{4.3}$$

Using this result, the uncertainty on n^* and δ is calculated following equation 4.2.

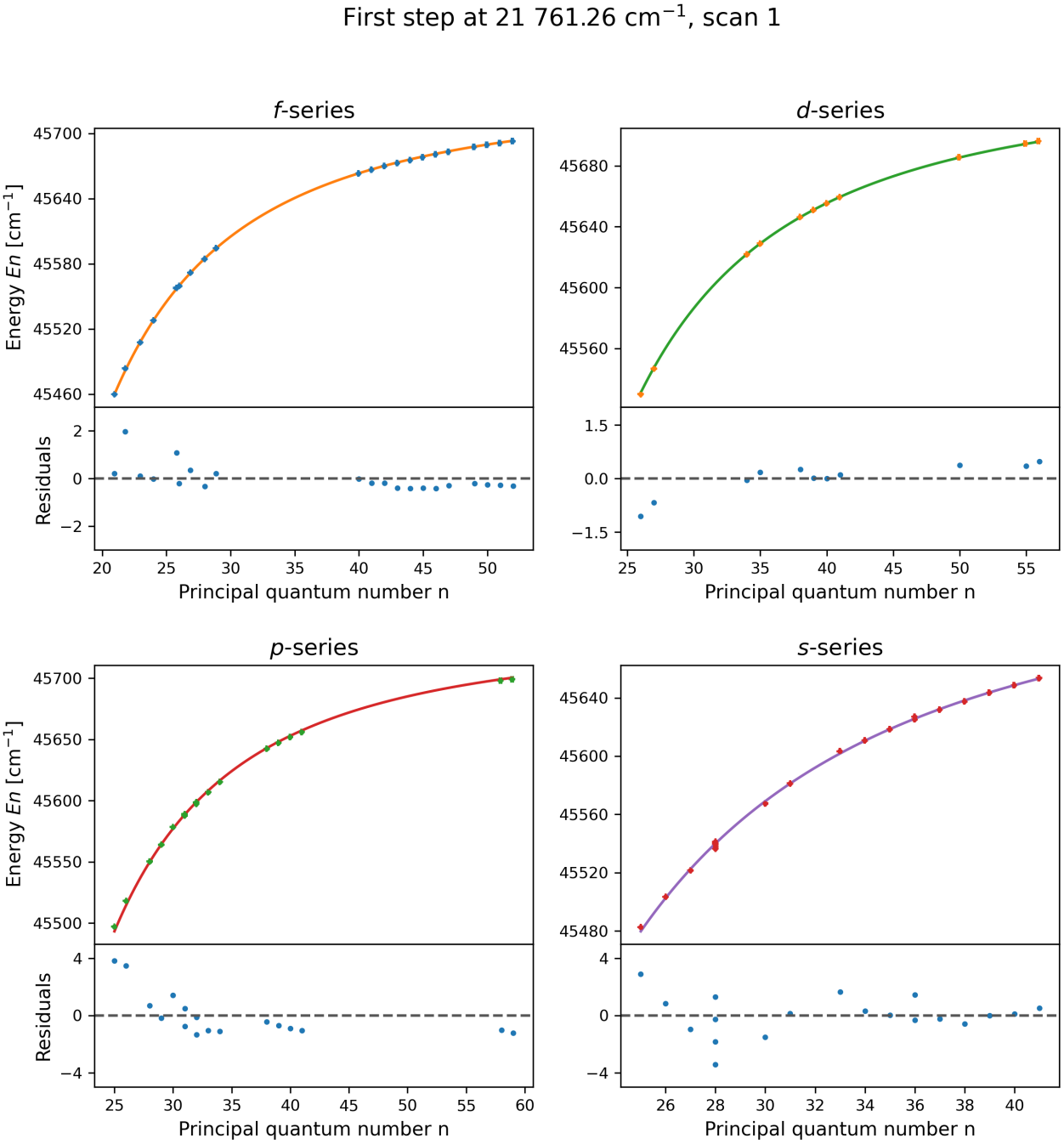

Figure 4.10: *Fit of the energy as a function of the principal quantum number following equation 4.4, for the first scan of the first scheme. Each series is fitted separately, resulting in a different value of the ionisation potential the Rydberg series converge to. Results of the fit are given in table 4.4*

Knowing that n has to be an integer quantum mechanically, the type of wave can be determined based on the fractional value of n^* and the values of $\delta_{\text{theoretical}}$. The estimate value for the ionisation potential is fine-tuned to get an approximate constant relation between n and δ. The respective estimated values for the ionisation potential for scheme 1 and scheme 2 are $E_{\text{IP, 1}}^{\text{estimate}} = E_{\text{IP, 2}}^{\text{estimate}} = 45735$ cm^{-1}. An explanation for these values can be found in appendix A. δ as a function of n is plotted in figures 4.8

and 4.9, for scheme 1 and scheme 2, respectively. The grey lines represent the theoretical values for δ. Note that the errorbars on δ increase for higher n. This is a result of the Rydberg peaks converging closer to the ionisation potential, and hence being more difficult to fit due to lower resolution.

Using the plots as a guide, the data points get grouped into the different series. Each series' energy as a function of principal quantum number is plotted and fitted separately using a non-linear least square fitting method lmfit [56], following:

$$E_n = E_{\text{IP}} - \frac{\mathcal{R}^*_{\text{Eu}}}{n - \delta_{\text{theoretical}}} \ . \tag{4.4}$$

However, for the second scheme, the first scan only has one datapoint as d-wave. Therefore, no reliable fit can be done so the point is omitted. The other fits return a value for the ionisation potential Rydberg states converge to. For the first scheme, first scan, the different fits for each wave is given in figure 4.10. The fits of the other scan and of the other scheme can be found in appendix B.The respective values for the different ionisation potentials are given in table 4.4.

Table 4.4: *The different values obtained for the ionisation potential from the fit of E_n vs n, for each scheme, scan and series. All values are given in inverse centimetres. No values is found for the d-wave of the first scan, second scheme as only one datapoint is available. As no reliable fit can be done, no ionisation potential is extracted for that d-wave.*

	Scheme 1		Scheme 2		
	Scan 1 [cm^{-1}]	Scan 2 [cm^{-1}]	Scan 1 [cm^{-1}]	Scan 2 [cm^{-1}]	Scan 3 [cm^{-1}]
s	45734.4 ± 0.3	45734.4 ± 0.3	45734.76 ± 0.10	45733.5 ± 0.3	45734.0 ± 0.2
p	45736.3 ± 0.4	45735.9 ± 0.2	45735.30 ± 0.11	45736.3 ± 0.3	45735.8 ± 0.3
d	45734.53 ± 0.14	45734.67 ± 0.13		45734.1 ± 0.3	45734.78 ± 0.16
f	45735.42 ± 0.12	45735.37 ± 0.12	45735.18 ± 0.03	45735.9 ± 0.3	45735.37 ± 0.08

4.2.3 Weighted Average of the Ionisation Potential

Using the different values of the ionisation potential, the weighted average $\bar{x}$ return one value according to [57]:

$$\bar{x} = \frac{\sum_i^n \frac{x_i}{(\Delta x_i)^2}}{\sum_i^n \frac{1}{(\Delta x_i)^2}} \ , \tag{4.5}$$

with x_i the n different values and their corresponding error Δx_i. The error on this weighted average is calculated accordingly by [57]:

$$\Delta\bar{x} = \frac{1}{\sqrt{\sum_i^n \frac{1}{(\Delta x_i)^2}}} \ . \tag{4.6}$$

The weighted average of the ionisation potential per scheme is shown in figure 4.11, together with the weighted average error. Using equation 4.5 for both schemes yields

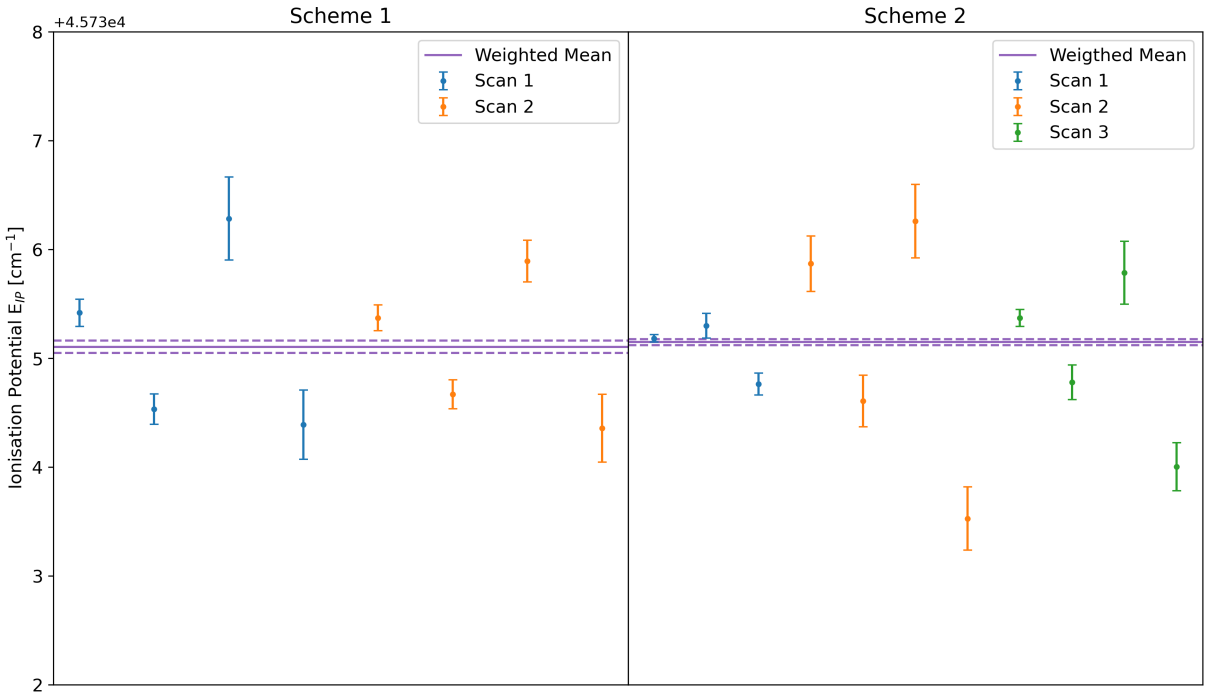

Figure 4.11: *Results for the ionisation potential for all scans per scheme as a result of the fit of energy as a function of principal quantum number. The purple lines are the corresponding weighted average with its uncertainty in dotted line. All scans scatter around the purple line with approximately the same pattern based on the type of wave.*

a weighted average $\bar{E}_{\text{IP}}$ of the ionisation potential at 45735.13 ± 0.03 cm^{-1} (5.670242 ± 0.000003 eV).

However, looking at figure 4.11, the values for the ionisation potential fluctuate around $\bar{E}_{\text{IP}}$ in the same pattern. Consequently, the different results for the ionisation potential are also plotted per wave, as is done in figure 4.12. Calculating the weighted average per wave using equation 4.5, yields the values given in table 4.5. The results are com-

Table 4.5: *Weighted average of the ionisation potential per wave, given in inverse centimeters. All measurements are combined per wave. The result for the s- and d-wave are lower than for the p- and f-wave, indicating that there might be an underlying effect on the ionisation potential.*

	s-wave	p-wave
$\bar{E}_{\text{IP}}$ [cm^{-1}]	45734.51 ± 0.08	45735.58 ± 0.09
$\bar{E}_{\text{IP}}$ [eV]	5.670164 ± 0.000010	5.670297 ± 0.000011
	d-wave	f-wave
$\bar{E}_{\text{IP}}$ [cm^{-1}]	45734.65 ± 0.08	45735.24 ± 0.03
$\bar{E}_{\text{IP}}$ [eV]	5.670181 ± 0.000010	5.670255 ± 0.000004

pared to those obtained in reference [40] in black, and the current literature value as obtained in [53] in pink. The black literature values follow the weighted average for both

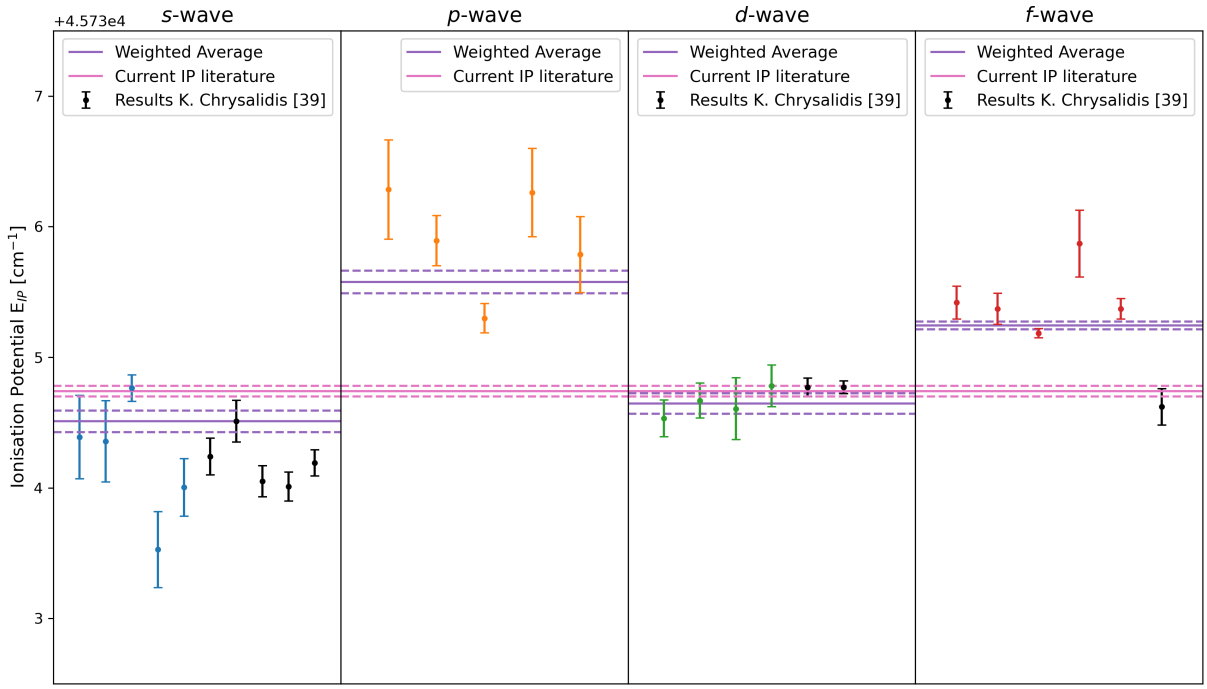

Figure 4.12: *Results for the ionisation potential per wave together with their weighted potential in purple. The results are compared to previous obtained result in reference [40] in black, and the current literature value for the ionisation potential in pink, as obtained in reference [53].*

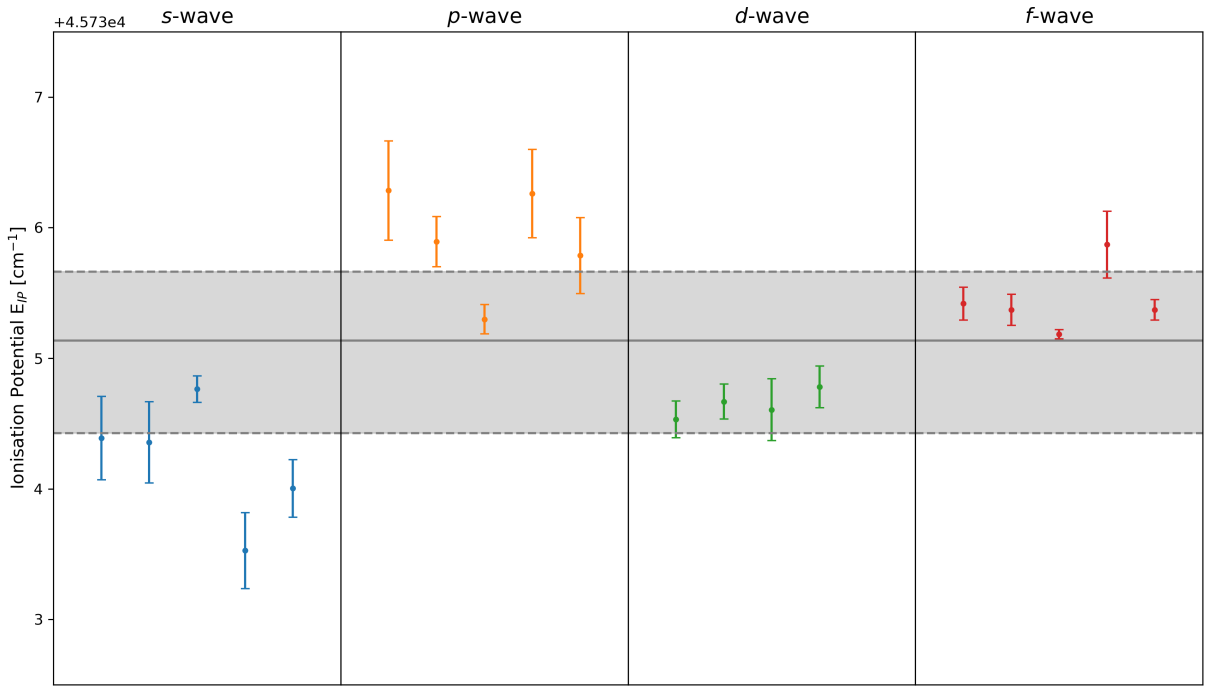

Figure 4.13: *Different ionisation potential results plotted per wave. The systematic fluctuations per wave indicates that the ionisation potential cannot be seen as an exact number, but as a region instead. This is indicated by the grey shaded region, spanning the lowest to highest possible value of the ionisation potential, originating from the weighted average per wave. The grey line portrays the weighted average for the ionisation potential for all datapoints.*

the s-wave and the d-wave. However, for the f-wave, the literature ionisation potential deviates from the respective weighted average. Granted, there is only one datapoint available for the f-wave. The current literature value for the ionisation potential of Eu is equal to $E_{\text{IP}}^{\text{Literature}} = 45734.74 \pm 0.04$ cm^{-1}. Therefore, the value is just below the value for the weighted average found in this thesis. However, for the determination of the ionisation potential, the referenced work only takes the contribution of the s-wave into account.

The values in table 4.5 and figure 4.12 for the weighted average per wave, shows values for s-, p-, d- and f-waves. The presence of parity mixing is explained by contributions of both electric and magnetic dipole transitions in lanthanides (see section 2.6). Additionally, the crystal field and configuration interactions induce configuration mixing, especially configuration interactions that mix states of the same parity. The systematic fluctuation of the value for the IP per wave, indicates that there is a systematic energy shift. This energy shift is explained by Rydberg mixing (see section 2.3.3). The overlapping Rydberg series for $6s$- and $6p$- valence electrons interact, shifting the IP. Additionally, the shift in ionisation energy indicates that the effect might be coupled to the parity.

This fluctuation argues that the ionisation potential is not an exact number, but rather a region. Hence, it is more appropriate for the ionisation potential to be given from the upper bound of the p-wave to the lower bound of the s-wave. This results in a region going from the lowest possible value between all waves, to the highest possible value for the IP, as is shown in figure 4.13. Thus, the region of the ionisation potential of europium spans 45734.43 cm^{-1} to 45735.67 cm^{-1} (5.670154 eV to 5.670308 eV). The use of an IP region is also supported by the PISA not having mass separation. The resulting ionisation potential is a linear combination of the IP's of stable isotopes (^{151}Eu and ^{153}Eu) according to their natural abundance. To know a more exact value for the ionisation potential per isotope, on-line measurements should be done.

Chapter 5

Conclusions and Outlook

The objective of this thesis was to use resonance laser ionisation to investigate lanthanides. Specifically, to develop a laser ionisation scheme that exclusively uses Ti:Sa lasers of the RILIS setup at CERN for the two lanthanides praseodymium and europium. Additionally, for praseodymium, this laser scheme had to be sensitive to the hyperfine structure. The measurements were done by implementing atomic samples in the PISA.

This thesis presented the literature study done for the first excitation step of the laser scheme for praseodymium. The two schemes chosen to investigate had a first step of $\lambda = 464.83$ nm and a first step of $\lambda = 463.70$ nm, respectively. Despite an improved coil and heat shield, no signal was seen for the schemes when scanned across the ionisation potential. This is likely due to the high temperature needed to create atomic vapour of Pr, which is not yet possible with the current setup.

Next, a literature study was done for a laser scheme of europium, yielding two different schemes. The first scheme used a first step of $\lambda = 459.53$ nm and the second scheme a first step of $\lambda = 462.57$ nm. Both schemes generated succesful meeasurements. The succesful measurements for Eu, in contrast to Pr can be explained by their differences in physicochemistry. Eu has oxidation states $+2$ and $+3$, while Pr only has $+3$, resulting in an easier measurement for Eu.
Subsequently, the schemes were used to investigate the ionisation potential of Europium. The observed parity mixing in the results is explained by the importance of both electric and magnetic dipole interactions in lanthanides. A systematic fluctuation per wave is observed in the IP. This trend in fluctuation can be explained from Rydberg mixing for Eu with multiple valence electrons. The energy states interact, generating a shift in the ionisation energy. As a result, the ionisation potential represents a region rather than an exact number. This is also endorsed by the fact that the PISA does not have a mass selection. Hence, the resulting IP is subject to a linear combination of the isotopes of Eu in their natural abundance. The resulting IP region spans from 5.670154 eV to 5.670308 eV.

In conclusion, it was not possible to develop a laser scheme that is sensitive to hyperfine splitting and exclusively uses Ti:Sa lasers for Pr, using the current PISA setup at RILIS. Future work for Pr should involve designing a cooling system for the PISA. That way, the temperature can be increased without the risk of melting the apparatus. Otherwise, praseodymium could also be investigated by using a full front-end in ISOLDE.

Nevertheless, it was possible to investigate two different first steps for a laser scheme that consists exclusively of Ti:Sa lasers for Eu using PISA at RILIS. These first steps allowed for the investigation of the ionisation potential of Eu, resulting in a ionisation potential region. To find a specific number, on-line measurements should be done. Additionally, to finalise the laser scheme, saturation and efficiency measurements remain for future work.

Bibliography

[1] K. Temst. Historal and Social Aspects of Physics, 2022. Lecture Series.

[2] K. Krane and W. Lynch. Introductory nuclear physics. *Physics today*, 42(1):78–78, 1989.

[3] S. S. M. Wong. *Introductory nuclear physics*. Wiley-VCH Verlag GmbH & Co. KGaA, Weinheim, [Germany, second edition, 2004 - 2004.

[4] W. Demtröder. *Nuclear and Particle Physics*. Springer, 2022.

[5] T. E. Cocolios. Nuclear Models, 2021. Lecture Series of 'Advanced Nuclear Physics'.

[6] B. Marsh. *In-Source Laser Resonance Ionization at ISOL Facilities*. PhD thesis, Manchester U., 2007. PhD thesis presented 14 March 2007.

[7] M. J. G. Borge and B. Jonson. ISOLDE past, present and future. *Journal of Physics G: Nuclear and Particle Physics*, 44(4):044011, Mar 2017.

[8] S. Rothe and T. Day Goodacre et al. Laser ion beam production at CERN-ISOLDE: New features – more possibilities. *Nuclear Instruments and Methods in Physics Research Section B: Beam Interactions with Materials and Atoms*, 376:91–96, 2016. Proceedings of the XVIIth International Conference on Electromagnetic Isotope Separators and Related Topics (EMIS2015).

[9] E. Mobs. The CERN accelerator complex. complexe des accélérateurs du CERN, 2016. General Photo.

[10] The ISOLDE facility. [Online]. Available: https://isolde.web.cern.ch/isolde-facility [Accessed November 27, 2023]. CERN, 2023.

[11] The ISOLDE Radioactive Ion Beam facility, [Online]. Available: https://isolde.web.cern.ch/isolde-radioactive-ion-beam-facility [2023, December 8]. CERN.

[12] R. Raabe. RIB production, 2022. Lecture Series of 'Exotic Nuclei: Properties and Interactions'.

[13] M. J. G. Borge and K. Blaum. Focus on exotic beams at ISOLDE: A laboratory portrait. *Journal of Physics G: Nuclear and Particle Physics*, 45(1):010301, Nov 2017.

[14] R. Mancheva. Towards a high throughput ion source for medical radioisotope production at medicis. https://indi.to/n8Z3m, Nov 2023. ISOLDE Workshop and Users Meeting.

[15] V. Fedosseev and K. Chrysalidis et al. Ion beam production and study of radioactive isotopes with the laser ion source at ISOLDE*. *Journal of Physics G: Nuclear and Particle Physics*, 44(8):084006, Jul 2017.

[16] W. Demtröder. *Atoms, molecules and photons: An introduction to atomic-, molecular-, and quantum-physics: With 677 figures and 42 tables*. Springer, second edition, 2010.

[17] W. T. Hill and C. H. Lee. *Light-matter interaction: Atoms and molecules in external fields and nonlinear optics*. Wiley-VCH, 2007.

[18] J. J. Sakurai and J. Napolitano. *Modern Quantum Mechanics, Second edition*. Addison-Wesley, 2011.

[19] A. Stesmans. Introduction to magnetic resonance: Lecture notes, 2023–2024.

[20] L. da Costa Pereira. Hyperfine interaction, 2022-2023. Lecture Notes.

[21] G. W. F. Drake and R. A. Swainson. Quantum defects and the 1/n dependence of rydberg energies: Second-order polarization effects. *Phys. Rev. A*, 44:5448–5459, Nov 1991.

[22] J. Berkowitz. *Photabsorption, photoionization, and photoelectron spectroscopy*. Academic Press, INC, New York, first edition, 1979.

[23] D. A. Atwood. *The Rare Earth Elements: Fundamentals and Applications*. Wiley, Chichester, 2013.

[24] B. Jacquier G. Liu. *Spectroscopic Properties of Rare Earths in Optical Materials*. Springer Series in Materials Science. Springer-Verlag Berlin Heidelberg 2005, Heidelberg, first edition, 2006. Jointly published with Tsinghua University Press, Beijing, China.

[25] S. Hooker and C. E. Webb. *Laser physics*. Oxford University Press, 2010.

[26] K. F. Renk. *Basics of Laser Physics for students of Science and Engineering*. Springer Heidelberg, 2012.

[27] E. Hecht. *Optics*. Pearson, fifth edition, 2017.

[28] W. Demtröder. *Laser Spectroscopy*. Vol. 1: Basic Principles. Springer-Verlag, fourth edition, 2008.

[29] W. Tittel. Optics: Lecture notes, 2023-2024. Course given at Université de Genève.

[30] K. Chrysalidis. *Improving the Spectral Coverage and Resolution of the ISOLDE RILIS*. PhD thesis, Mainz U., 2019. PhD thesis presented 29 November 2019.

[31] Cheal B. et al. Progress in laser spectroscopy at radioactive ion beam facilities. *Journal of Physics G: Nuclear and Particle Physics*, 37(11):113101, sep 2010.

[32] B. Marsh. Resonance ionization laser ion sources. 2013. 61 pages, contribution to the CAS-CERN Accelerator School: Ion Sources, Senec, Slovakia, 29 May - 8 June 2012, edited by R. Bailey.

[33] D.L. Mills. *Nonlinear Optics: Basic Concepts*. Springer-Verlag, 1998.

[34] L. Lalanne. New results and upgrades from the CRIS experiment at ISOLDE. https://indi.to/NqDxq, Nov 2023. ISOLDE Workshop and Users Meeting.

[35] D. Cotton. *Lanthanide and actinide chemistry.* Inorganic chemistry: a Wiley series of advanced textbooks. Wiley, Chichester, 2006.

[36] A. Karl A. Gschneidner and L. Eyring. *Handbook on the physics and chemistry of rare earths*. Handbook on the physics and chemistry of rare earths 2. North-Holland, Amsterdam, 1979.

[37] C. Bernerd. RILIS operation and development in 2023. https://indi.to/VrS6b, Nov 2023. ISOLDE Workshop and Users Meeting.

[38] The ISOLDE RILIS | Motivation for RILIS, [Online]. Available: https://rilis-web.web.cern.ch/training [2023, November 3]. CERN.

[39] T. Kron. *Konzeption, Aufbau und Test einer Referenzzelle für die resonante Laserionisation*. PhD thesis, Mainz U., 2011. PhD thesis presented 8 December 2011.

[40] K. Chrysalidis. Resonance ionization spectroscopy of europium: The first application of the PISA at ISOLDE-RILIS, 2016. Presented 26 Sep 2016.

[41] W. R. Leo. *Techniques for nuclear and particle physics experiments: A how-to approach*. Springer-Verlag, 1994.

[42] S. Rothe, B. A. Marsh, C. Mattolat, V. N. Fedosseev, and K. Wendt. A complementary laser system for ISOLDE rilis. *Journal of Physics: Conference Series*, 312(5):052020, sep 2011.

[43] S. Rothe. An all-solid state laser system for the laser ion source rilis and in-source laser spectroscopy of astatine at ISOLDE, CERN, 2012. PhD thesis presented 24 September 2012.

[44] ISOLDE | RILIS, [Online]. Available: https://isolde.web.cern.ch/rilis [2023, November 3]. CERN.

[45] G. Ghosh. Temperature dispersion of refractive indices in β□bab2o4 and lib3o5 crystals for nonlinear optical devices. *Journal of Applied Physics*, 78:6752 – 6760, 01 1996.

[46] H. Lingxiong, L. Xiang, Z. Ge, H. Chenghui, and W. Yong. The accurate refractive indices of BIBO crystal at different temperatures. *Journal of Physics D: Applied Physics*, 42(22):225109, nov 2009.

[47] P. Naubereit. *Resonance Ionization Spectroscopy of Protactinium : Studies on Intrinsic Quantum Chaos and the Ionization Potential*. PhD thesis, Mainz, 2020.

[48] V. N. Fedosseev, B. A. Marsh, D. V. Fedorov, U. Köster, and E. Tengborn. Ionization scheme development at the ISOLDE RILIS. *Hyperfine Interactions*, 162(1–4):15–27, 2006.

[49] A. Kramida, Y. Ralchenko, J. Reader, and NIST ASD Team. NIST Atomic Spectra Database (ver. 5.10), [Online]. Available: https://physics.nist.gov/asd [2023, November 3]. National Institute of Standards and Technology, Gaithersburg, MD., 2022.

[50] V. V. Kazakov and V. G. Kazakov et al. Electronic structure of atoms: atomic spectroscopy information system [Online]. Available: http://stacks.iop.org/1402-4896/92/i=10/a=105002 [2023, November 3]. Physica Scripta, 2017.

[51] R. L. Kurucz and B. Bell. Atomic Line Data Kurucz CD-ROM No. 23, [Online]. Available: https://lweb.cfa.harvard.edu/amp/ampdata/kurucz23/sekur.html [2023, November 3]. Smithsonian Astrophysical Observatory, Cambridge, Mass., 1995.

[52] T. D. Goodacre. *Applied Laser Spectroscopy for Nuclear Physics: Isotope Shifts in the Mercury Isotopic Chain and Laser Ion Source Development*. Springer Theses. Springer Nature, Switzerland, 2021.

[53] S. G. Nakhate, M. A. Razvi, J. P. Connerade, and S. A. Ahmad. Investigation of rydberg states of the europium atom using resonance ionization spectroscopy. *Journal of Physics B: Atomic, Molecular and Optical Physics*, 33(22):5191–5202, Nov 2000.

[54] The Scipy community. scipy.optimize.curve_fit - scipy v1.13.0 manual.

[55] U. Fano, C. E. Theodosiou, and J. L. Dehmer. Electron-optical properties of atomic fields. *Rev. Mod. Phys.*, 48:49–68, Jan 1976.

[56] R. Otten et al. M. Newville, T. Stensitzki. Getting started with non-linear least-squares fitting. LMFIT: Non-Linear Least-Squares Minimization and Curve-Fitting for Python [Online]. Available: https://lmfit.github.io/lmfit-py/intro.html [2024, May 20].

[57] J. Van de Vondel. Meetfouten - Statistiek, 2023-2024. Lecture Notes of 'Experimentele basistechnieken in de natuurkunde'.

Appendix A

Initial Estimate Value of the Ionisation Potential

The determination of the ionisation potential requires to give an initial estimation of the ionisation potential $E_{\text{IP}}^{\text{estimate}}$. This estimate value should result in an approximate constant relation between the quantum defect δ and the principal quantum number n for each wave. Initially, five different estimate values are investigated:

- $E_{\text{IP}}^{\text{estimate}} = 45733$ cm^{-1}, as it visually gives a more constant relation between δ and n for scheme 1.
- $E_{\text{IP}}^{\text{estimate}} = 45736$ cm^{-1}, as it visually gives a more constant relation between δ and n for scheme 2.
- $E_{\text{IP}}^{\text{estimate}} = 45734$ cm^{-1} to better explore the parameter space.
- $E_{\text{IP}}^{\text{estimate}} = 45735$ cm^{-1} to better explore the parameter space.
- $E_{\text{IP}}^{\text{estimate}} = 45734.74$ cm^{-1}, as current literature value for the ionisation potential as obtained in reference [53]

The different plots of δ as a function of n for both schemes is depicted in figure A.1. To examine which of these plots results in a more constant relation between δ and n, the data is fitted with a linear relation according to:

$$y = m \cdot x + q, \tag{A.1}$$

with m the slope which should be approximately zero, and q the vertical displacement which is this case should be approximately the theoretical value of the quantum defect per wave. The fit is done per wave and per scheme. Hence, the scans per scheme are added together, this to increase statistics. The fits are done using lmfit, and are shown in figures A.2, A.3, A.4, A.5, A.6, A.7, A.8, A.9, and A.10, A.11. The best parameter values, as well as the corresponding χ^2 from the fits are presented in tables A.1, A.2, A.3, A.4, and A.5 corresponding to the different $E_{\text{IP}}^{\text{estimate}}$.

The best initial estimate of the IP, is the one that gives a more constant relation between δ and n. With this in mind, the different fit parameters are compared. For scheme 1 $E_{\text{IP}}^{\text{estimate}} = 45736$ cm^{-1} gives the largest q-values, and so the largest deviation from

zero. Additionally, $E_{\text{IP}}^{\text{estimate}} = 45734$ cm^{-1} returns q-values with largest uncertainty. Hence, these two options are not longer taken into account for scheme 1. The fit for scheme 2 with $E_{\text{IP}}^{\text{estimate}} = 45736$ cm^{-1} and $E_{\text{IP}}^{\text{estimate}} = 45734.74$ cm^{-1}, return q-values with the largest deviation from zero. Thus, for scheme 2 these estimate values are no longer considered. The remainder options for the estimate value for both scheme 1 and scheme 2 all have q-values of the same order.
Secondly, the best predictor of the theoretical quantum defect is examined. For scheme 1 $E_{\text{IP}}^{\text{estimate}} = 45733$ cm^{-1} is overall the worst and so is no longer considered. For scheme 2 $E_{\text{IP}}^{\text{estimate}} = 45735$ cm^{-1} is overall a better predictor, however it is not a good predictor. $E_{\text{IP}}^{\text{estimate}} = 45733$ cm^{-1} and $E_{\text{IP}}^{\text{estimate}} = 45734$ cm^{-1} return values for m with deviations from $\delta_{\text{theoretical}}$ of the same order. Therefore, no $E_{\text{IP}}^{\text{estimate}}$ are excluded for scheme 2 based on the condition on m.
Lastly, the χ^2 values are considered, or also which estimate value gives the best fit. With that said, χ^2-values of both $E_{\text{IP}}^{\text{estimate}} = 45735$ cm^{-1} and $E_{\text{IP}}^{\text{estimate}} = 45734.74$ cm^{-1} are of the same order, so they both fit the constant relation well. Nevertheless, $E_{\text{IP}}^{\text{estimate}} = 45735$ cm^{-1} is chosen as estimate value for scheme 1 as between the remaining $E_{\text{IP}}^{\text{estimate}}$ it returns overall q-values closer to zero, a more constant relation. For scheme 2 comparing the different χ^2-values, $E_{\text{IP}}^{\text{estimate}} = 45735$ cm^{-1} returns the best fit with the lowest χ^2-values.

In conclusion for both scheme 1 and scheme 2, $E_{\text{IP}}^{\text{estimate}} = 45735$ cm^{-1} is chosen as the initial estimate value of the ionisation potential.

Table A.1: *Overview of the parameters m, q and the χ^2-value obtained from the linear fit between δ and n for initial estimate value of the ionisation potential of $E_{IP}^{estimate} = 45733$ cm^{-1}. All scans per scheme are combined and fitted for each wave separately using lmfit.*

$E_{\text{IP}}^{\text{estimate}} = 45733$ cm^{-1}		Scheme 1	Scheme 2
s-wave	m	-0.0013 ± 0.0012	0.0002 ± 0.0009
	q	4.35 ± 0.05	4.27 ± 0.04
	χ^2	0.69828	1.4378
p-wave	m	0.0011 ± 0.0014	-0.0010 ± 0.0009
	q	3.76 ± 0.06	3.65 ± 0.03
	χ^2	0.18626	0.29284
d-wave	m	-0.0001 ± 0.0005	-0.0004 ± 0.0007
	q	2.84 ± 0.02	2.87 ± 0.02
	χ^2	0.012496	0.046872
f-wave	m	0.00034 ± 0.00037	-0.0005 ± 0.0004
	q	0.93 ± 0.01	0.96 ± 0.02
	χ^2	0.027358	0.044522

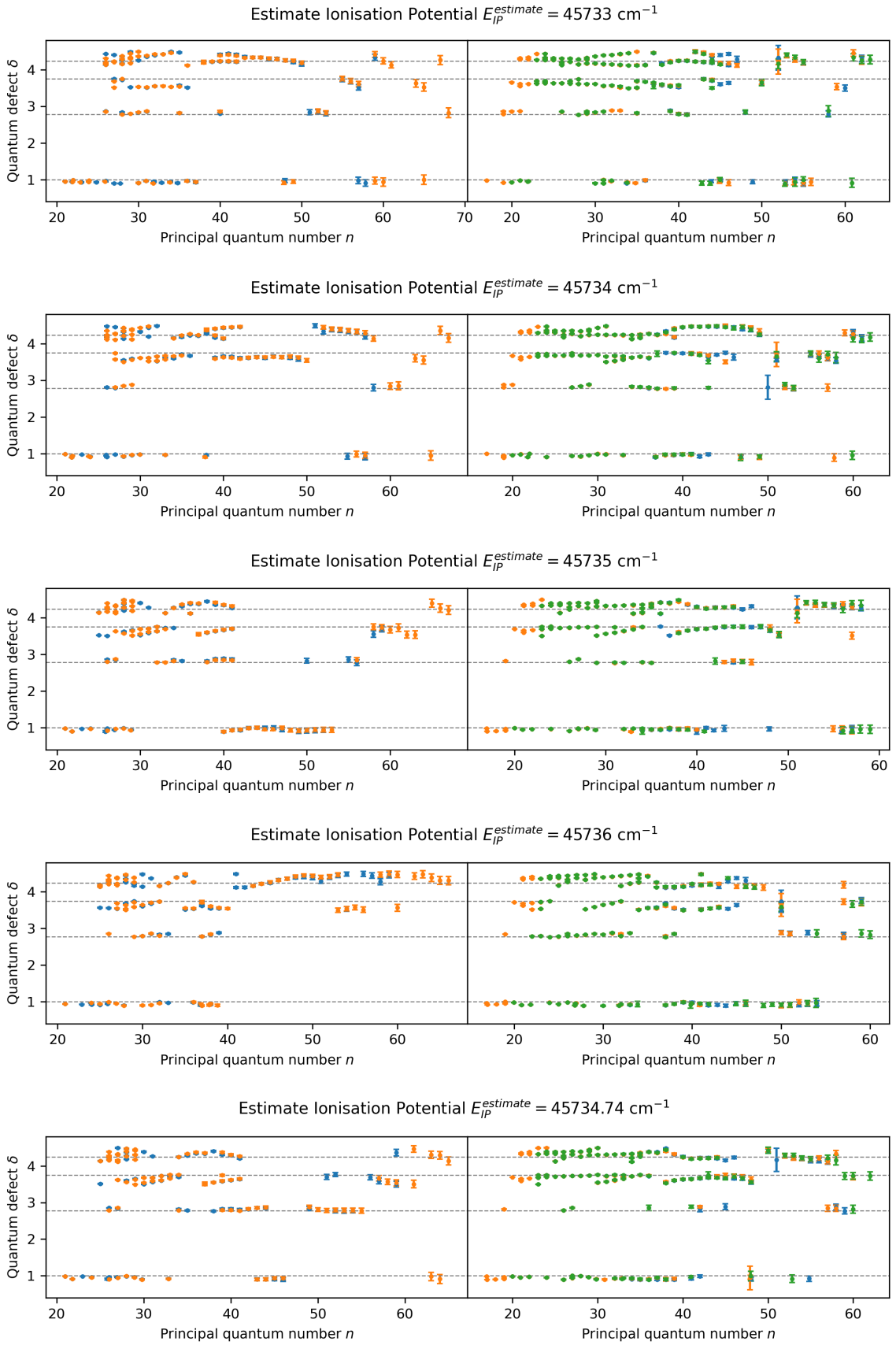

Figure A.1: *Plot of the quantum defect as a function of the principal quantum number, per scheme for different initial estimate values for the ionisation potential. Scheme 1 is depicted on the left, while scheme 2 is depicted on the right, each with their respective scans in different colour. The grey dotted lines represent the theoretical values for the quantum defect. The different* $E_{IP}^{estimate}$ *are* 45733 *cm*$^{-1}$, $E_{IP}^{estimate} = 45734$ *cm*$^{-1}$, $E_{IP}^{estimate} = 45735$ *cm*$^{-1}$, 45736 *cm*$^{-1}$ *and* 45734.74 *cm*$^{-1}$. *The best estimate value is the one that gives a more constant relation between* δ *and* n.

Table A.2: *Overview of the parameters m, q and the χ^2-value obtained from the linear fit between δ and n for initial estimate value of the ionisation potential of $E_{IP}^{estimate} = 45734$ cm^{-1}. All scans per scheme are combined and fitted for each wave separately using lmfit.*

$E_{\text{IP}}^{\text{estimate}} = 45734$ cm^{-1}		Scheme 1	Scheme 2
s-wave	m	0.0011 ± 0.0012	0.0005 ± 0.0010
	q	4.27 ± 0.05	4.31 ± 0.04
	χ^2	0.85746	1.1645
p-wave	m	0.0002 ± 0.0008	-0.0001 ± 0.0007
	q	3.61 ± 0.03	3.67 ± 0.02
	χ^2	0.10763	0.32155
d-wave	m	0.0002 ± 0.0007	-0.0014 ± 0.0006
	q	2.82 ± 0.03	2.87 ± 0.02
	χ^2	0.0070092	0.029876
f-wave	m	0.0001 ± 0.0004	-0.0008 ± 0.0005
	q	0.94 ± 0.02	0.98 ± 0.02
	χ^2	0.024354	0.057109

Table A.3: *Overview of the parameters m, q and the χ^2-value obtained from the linear fit between δ and n for initial estimate value of the ionisation potential of $E_{IP}^{estimate} = 45735$ cm^{-1}. All scans per scheme are combined and fitted for each wave separately using lmfit.*

$E_{\text{IP}}^{\text{estimate}} = 45735$ cm^{-1}		Scheme 1	Scheme 2
s-wave	m	0.0007 ± 0.0016	-0.0008 ± 0.0007
	q	4.28 ± 0.06	4.35 ± 0.03
	χ^2	0.52956	0.76511
p-wave	m	0.0011 ± 0.0010	-0.0005 ± 0.0011
	q	3.60 ± 0.04	3.70 ± 0.04
	χ^2	0.21906	0.46474
d-wave	m	-0.0003 ± 0.0008	-0.0007 ± 0.0009
	q	2.85 ± 0.03	2.82 ± 0.03
	χ^2	0.022605	0.017768
f-wave	m	-0.0002 ± 0.0005	-0.0001 ± 0.0003
	q	0.96 ± 0.02	0.96 ± 0.01
	χ^2	0.045842	0.044531

Table A.4: *Overview of the parameters m, q and the χ^2-value obtained from the linear fit between δ and n for initial estimate value of the ionisation potential of $E_{IP}^{estimate} = 45736$ cm^{-1}. All scans per scheme are combined and fitted for each wave separately using lmfit.*

$E_{\text{IP}}^{\text{estimate}} = 45736$ cm^{-1}		Scheme 1	Scheme 2
s-wave	m	0.0038 ± 0.0010	-0.008 ± 0.001
	q	4.18 ± 0.04	4.59 ± 0.05
	χ^2	0.75979	0.97499
p-wave	m	-0.003 ± 0.001	0.0002 ± 0.001
	q	3.71 ± 0.05	3.60 ± 0.04
	χ^2	0.17944	0.38927
d-wave	m	0.001 ± 0.002	0.0012 ± 0.0004
	q	2.80 ± 0.08	2.79 ± 0.02
	χ^2	0.015586	0.052211
f-wave	m	-0.001 ± 0.001	-0.0001 ± 0.0003
	q	0.96 ± 0.03	0.94 ± 0.01
	χ^2	0.025718	0.064395

Table A.5: *Overview of the parameters m, q and the χ^2-value obtained from the linear fit between δ and n for initial estimate value of the ionisation potential of $E_{IP}^{estimate} = 45734.74$ cm^{-1}. All scans per scheme are combined and fitted for each wave separately using lmfit.*

$E_{\text{IP}}^{\text{estimate}} = 45734.74$ cm^{-1}		Scheme 1	Scheme 2
s-wave	m	-0.0006 ± 0.0014	-0.0043 ± 0.0007
	q	4.27 ± 0.05	4.45 ± 0.03
	χ^2	0.44198	0.70650
p-wave	m	-0.0005 ± 0.0012	-0.0004 ± 0.0007
	q	3.64 ± 0.05	3.69 ± 0.03
	χ^2	0.26856	0.34098
d-wave	m	-0.0011 ± 0.0006	0.0003 ± 0.0007
	q	2.86 ± 0.03	2.83 ± 0.03
	χ^2	0.028871	0.019889
f-wave	m	-0.0009 ± 0.0005	-0.0008 ± 0.0004
	q	0.97 ± 0.02	0.96 ± 0.02
	χ^2	0.029229	0.058771

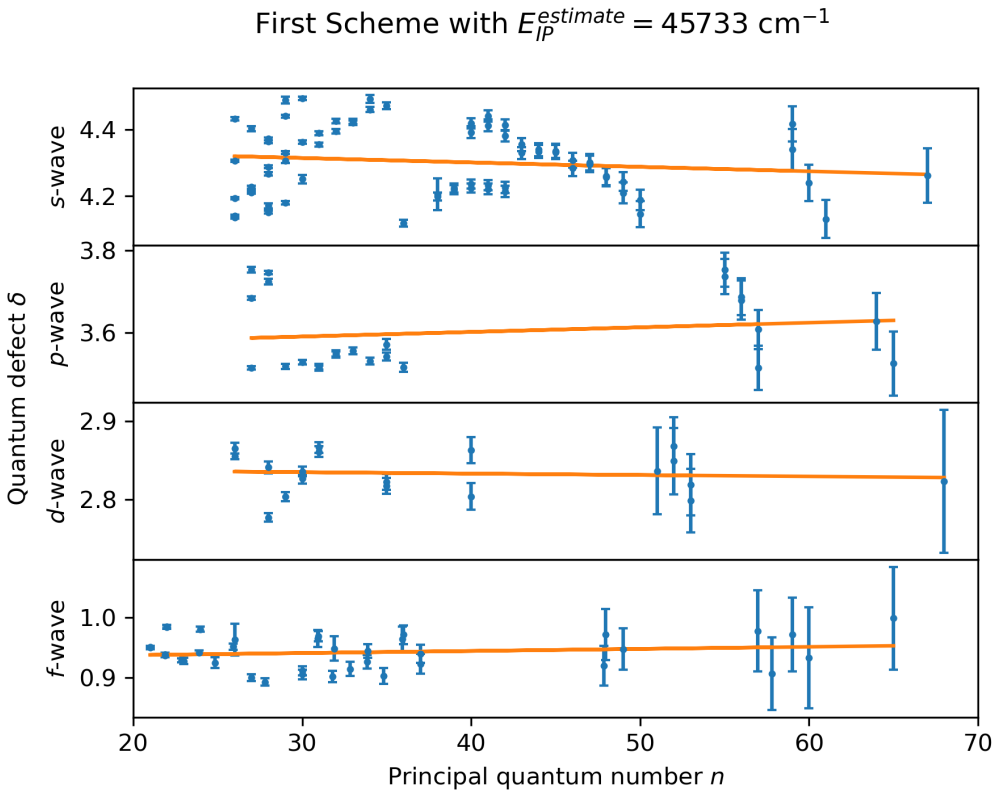

Figure A.2: *Linear fit of the quantum defect as a function of the principal quantum number for the first scheme with initial ionisation potential estimate of* $E_{IP}^{estimate} = 45733$ *cm*$^{-1}$*. Both scans of the first scheme are combined and then fitted per wave using lmfit. The ideal* $E_{IP}^{estimate}$ *yields a constant relation between* δ *and* n*.*

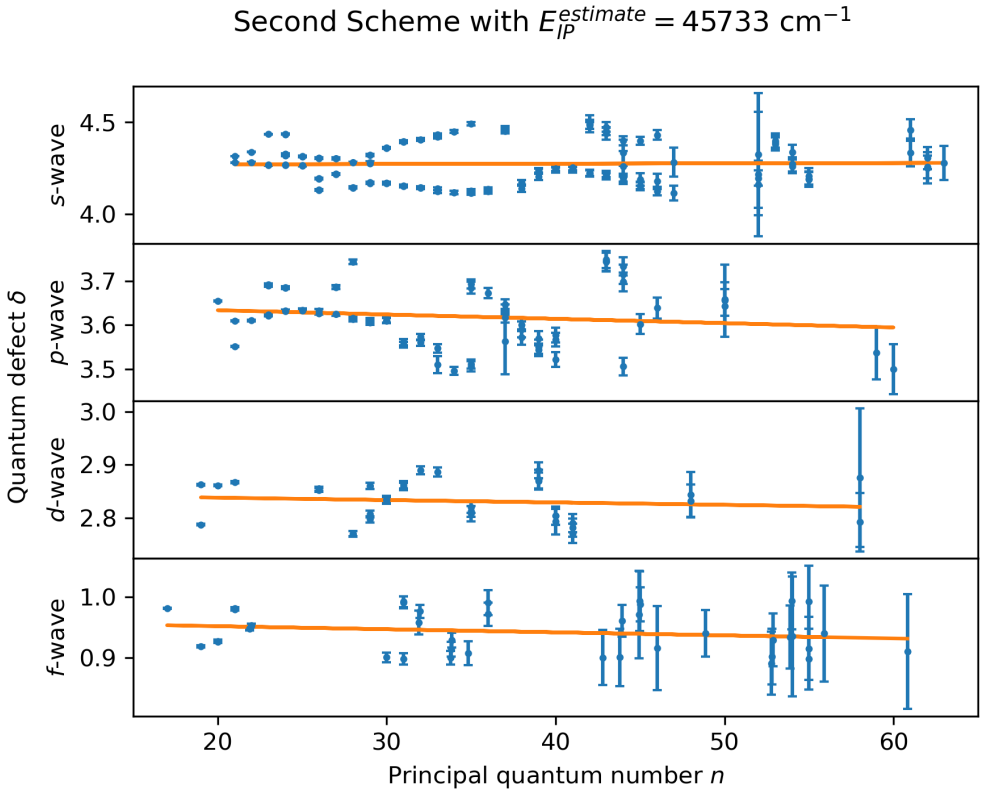

Figure A.3: *Linear fit of the first scheme with initial ionisation potential estimate of* $E_{IP}^{estimate} = 45733$ *cm*$^{-1}$*. All three scans of the second scheme are combined and then fitted per wave using lmfit. The ideal* $E_{IP}^{estimate}$ *yields a constant relation between* δ *and* n*.*

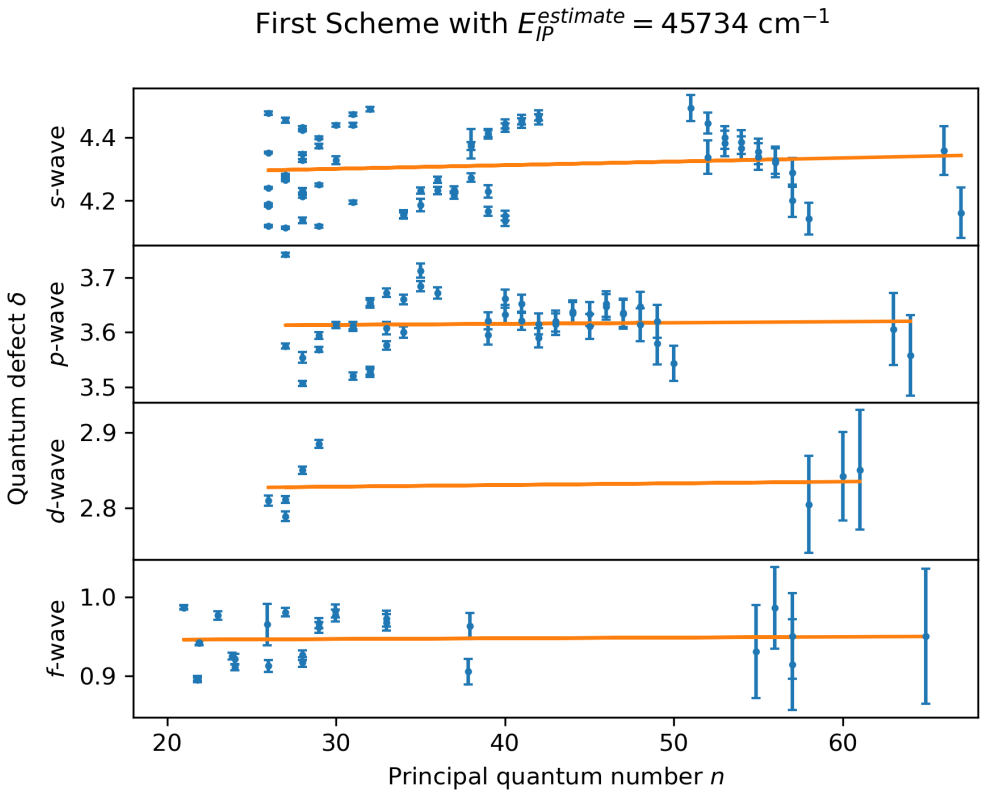

Figure A.4: *Linear fit of the first scheme with initial ionisation potential estimate of* $E_{IP}^{estimate} = 45734$ *cm*$^{-1}$. *Both scans of the first scheme are combined and then fitted per wave using lmfit. The ideal* $E_{IP}^{estimate}$ *yields a constant relation between* δ *and* n.

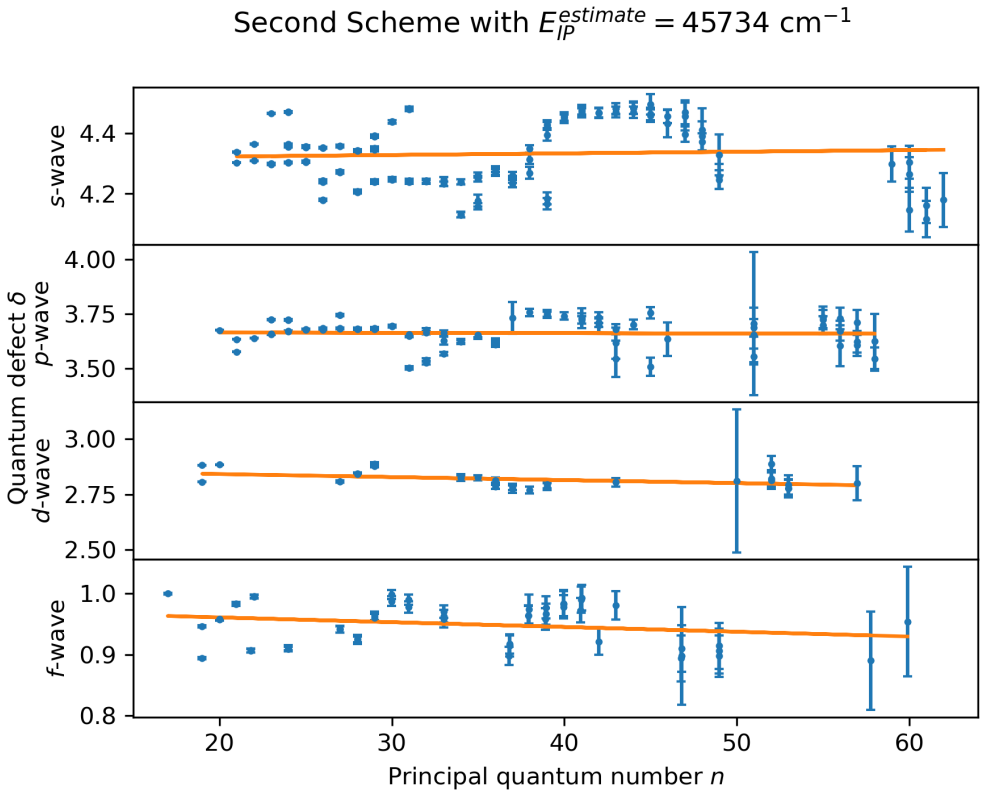

Figure A.5: *Linear fit of the first scheme with initial ionisation potential estimate of* $E_{IP}^{estimate} = 45734$ *cm*$^{-1}$. *All three scans of the second scheme are combined and then fitted per wave using lmfit. The ideal* $E_{IP}^{estimate}$ *yields a constant relation between* δ *and* n.

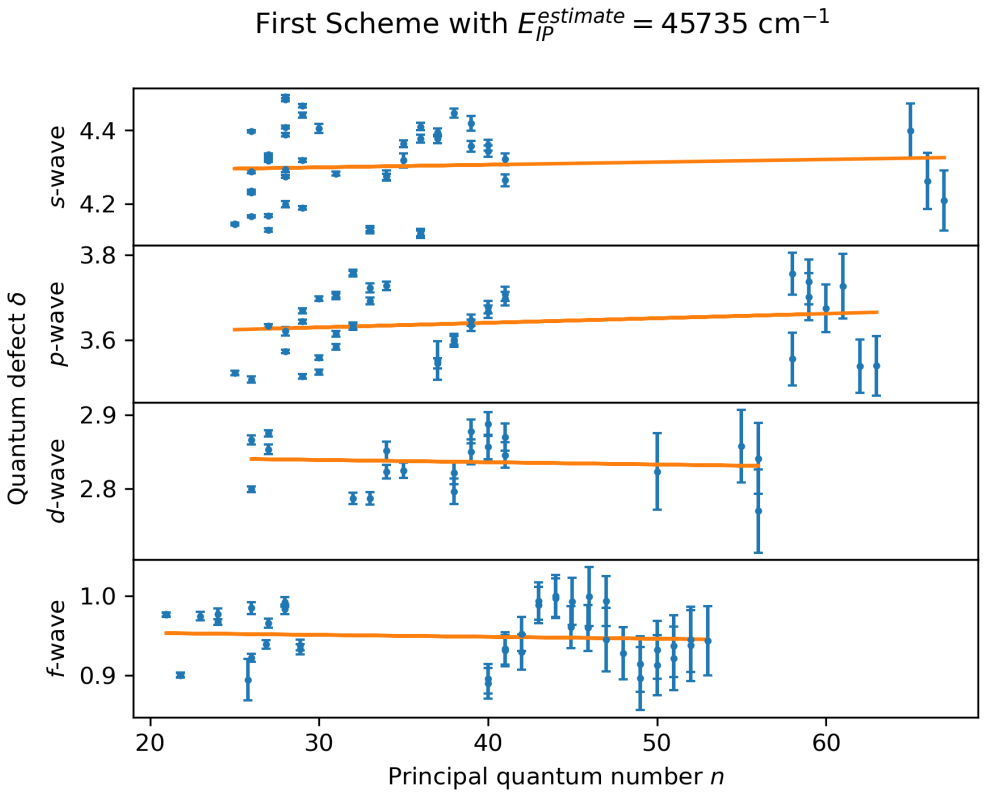

Figure A.6: *Linear fit of the first scheme with initial ionisation potential estimate of* $E_{IP}^{estimate} = 45735$ *cm*$^{-1}$. *Both scans of the first scheme are combined and then fitted per wave using lmfit. The ideal* $E_{IP}^{estimate}$ *yields a constant relation between* δ *and* n.

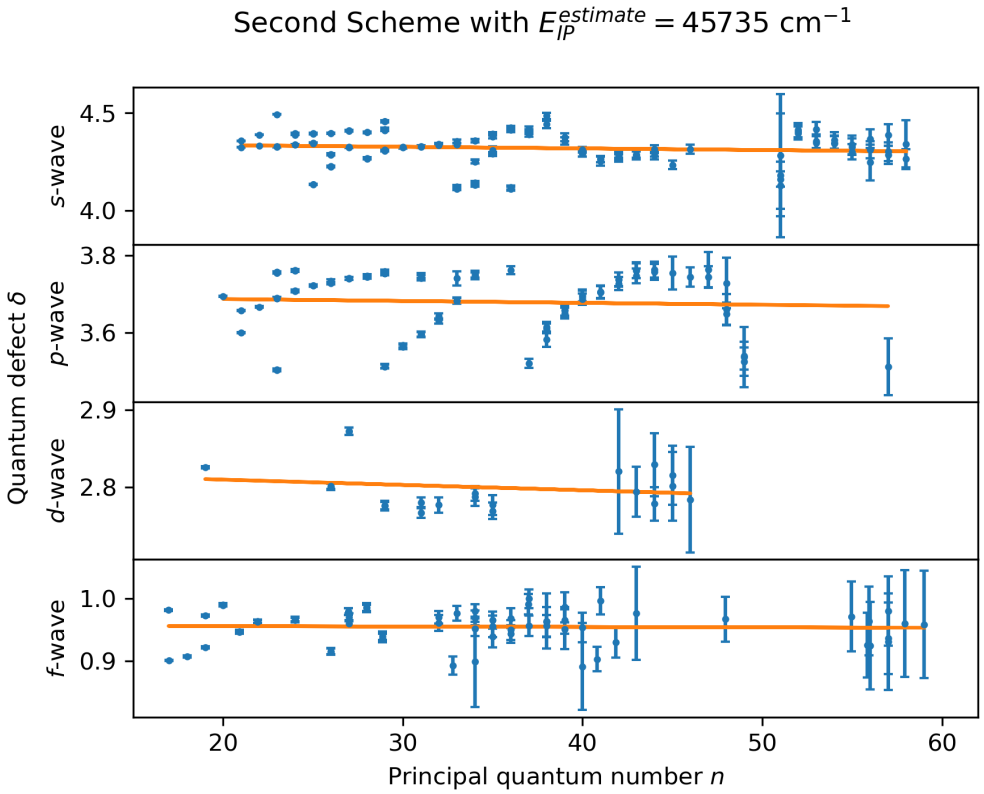

Figure A.7: *Linear fit of the first scheme with initial ionisation potential estimate of* $E_{IP}^{estimate} = 45735$ *cm*$^{-1}$. *All three scans of the second scheme are combined and then fitted per wave using lmfit. The ideal* $E_{IP}^{estimate}$ *yields a constant relation between* δ *and* n.

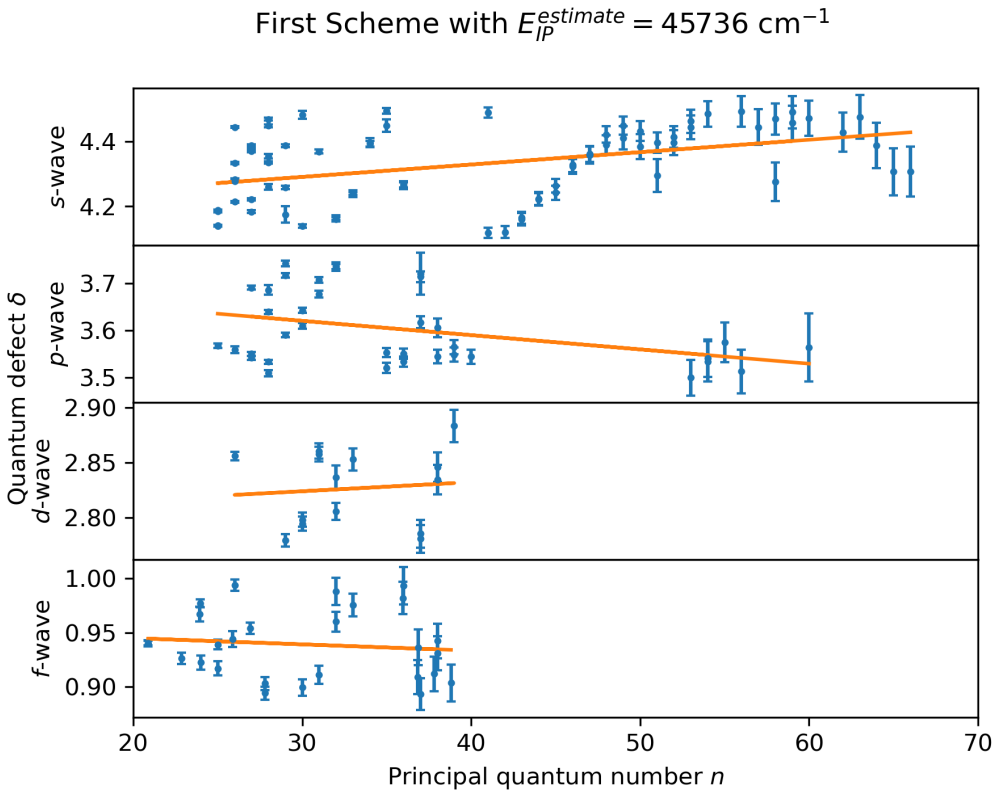

Figure A.8: *Linear fit of the first scheme with initial ionisation potential estimate of* $E_{IP}^{estimate} = 45736$ *cm*$^{-1}$*. Both scans of the first scheme are combined and then fitted per wave using lmfit. The ideal* $E_{IP}^{estimate}$ *yields a constant relation between* δ *and* n*, which seen from the plot, is not the case.*

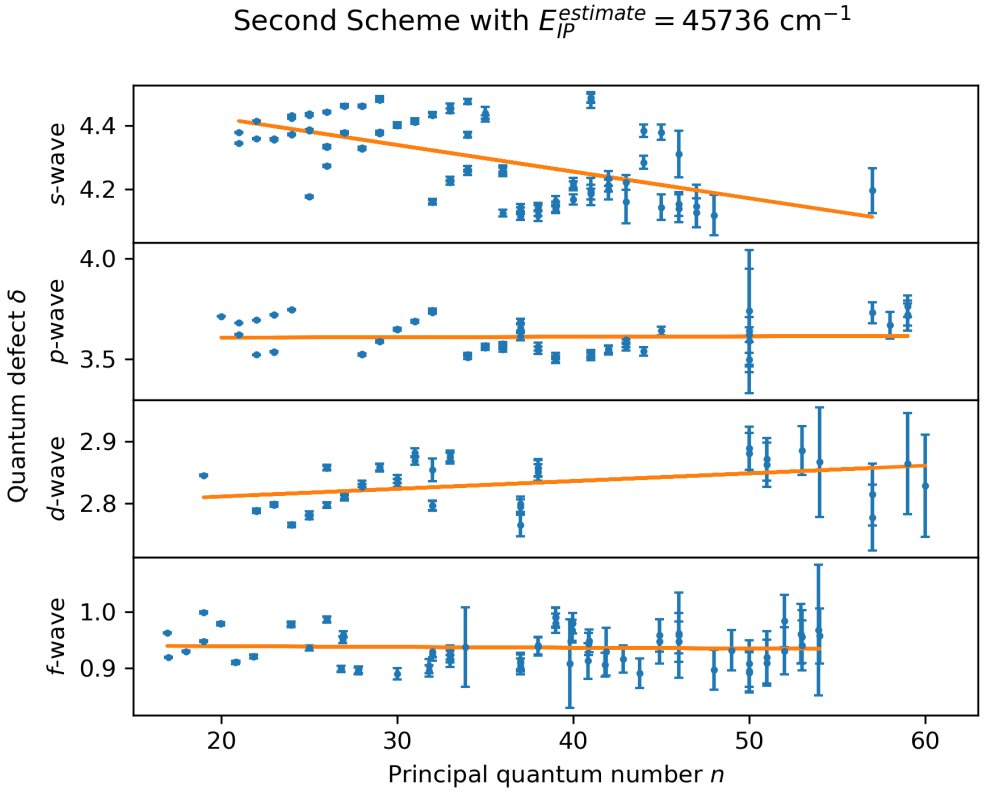

Figure A.9: *Linear fit of the first scheme with initial ionisation potential estimate of* $E_{IP}^{estimate} = 45736$ *cm*$^{-1}$*. All three scans of the first scheme are combined and then fitted per wave using lmfit. The ideal* $E_{IP}^{estimate}$ *yields a constant relation between* δ *and* n*, which seen from the plot, is not the case.*

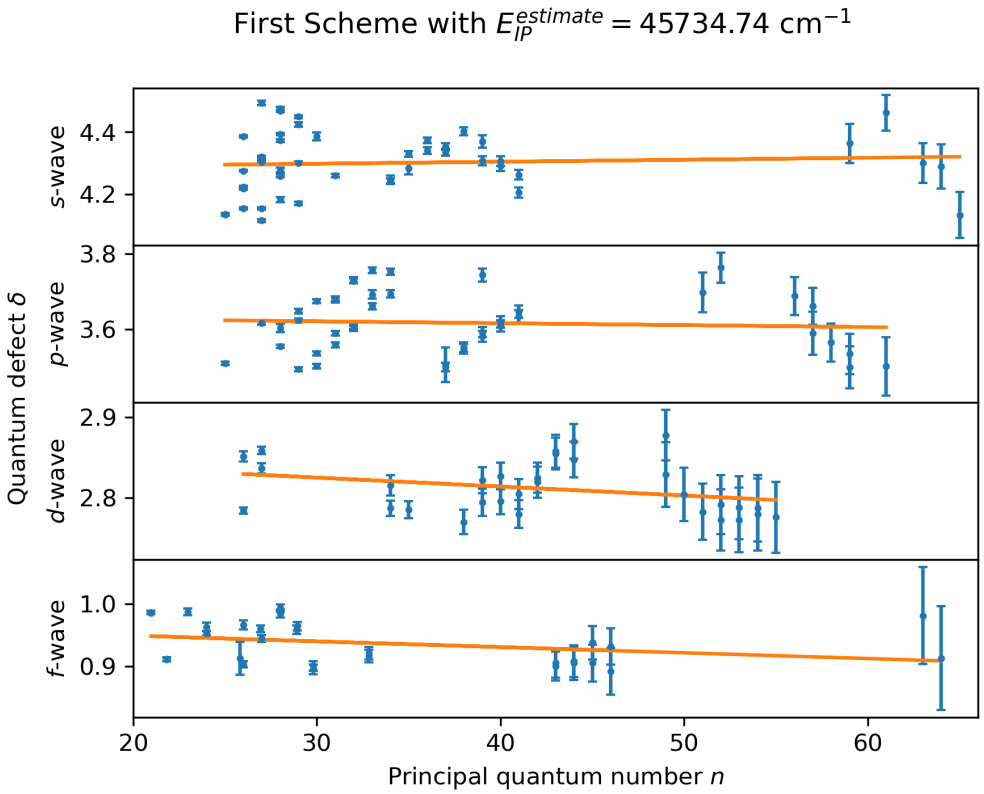

Figure A.10: *Linear fit of the first scheme with initial ionisation potential estimate of* $E_{IP}^{estimate} = 45734.74$ *cm*$^{-1}$*. Both scans of the first scheme are combined and then fitted per wave using lmfit. The ideal* $E_{IP}^{estimate}$ *yields a constant relation between* δ *and* n*.*

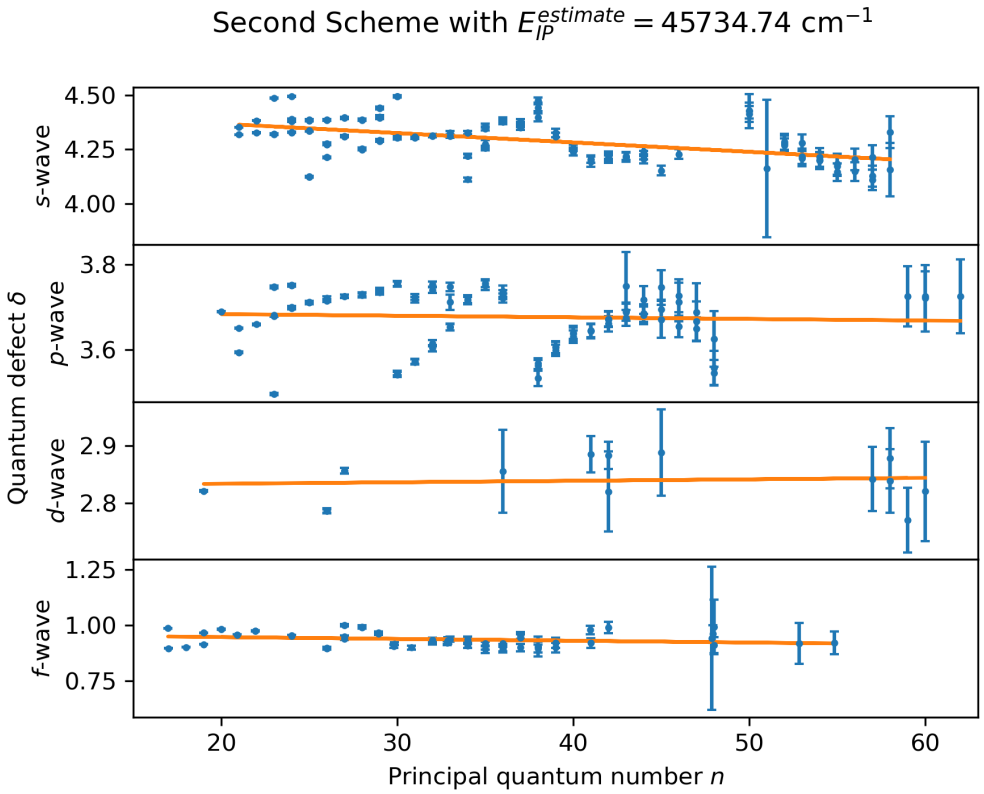

Figure A.11: *Linear fit of the first scheme with initial ionisation potential estimate of* $E_{IP}^{estimate} = 45734.74$ *cm*$^{-1}$*. All three scans of the second scheme are combined and then fitted per wave using lmfit [56]. The ideal* $E_{IP}^{estimate}$ *yields a constant relation between* δ *and* n*.*

Appendix B

Converging Rydberg Series Fitted

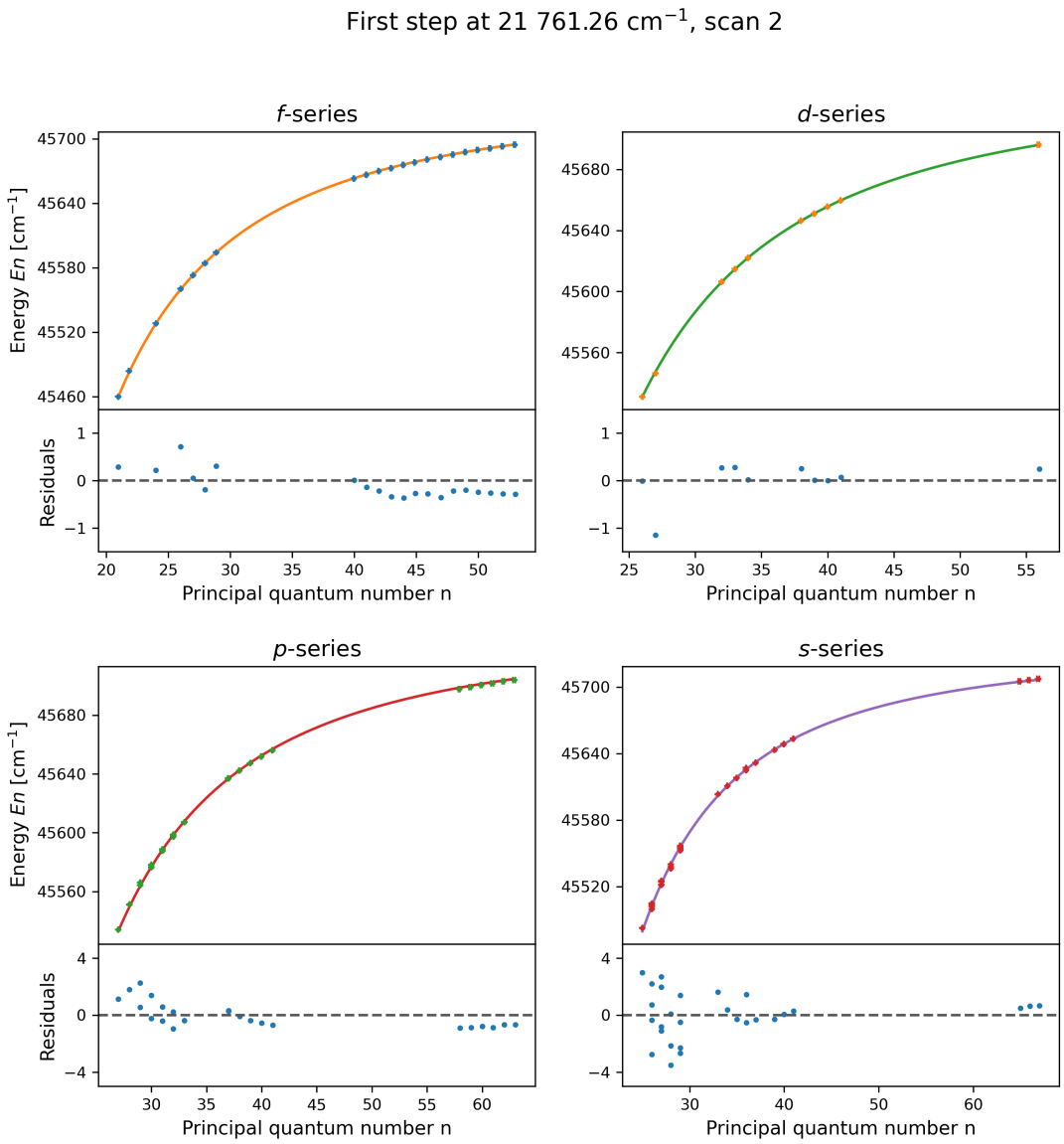

Figure B.1: *Fit of the energy as a function of the principal quantum number following equation 4.4, for the second scan of the first scheme. Each series is fitted separately, resulting in a different value of the ionisation potential the Rydberg series converge to.*

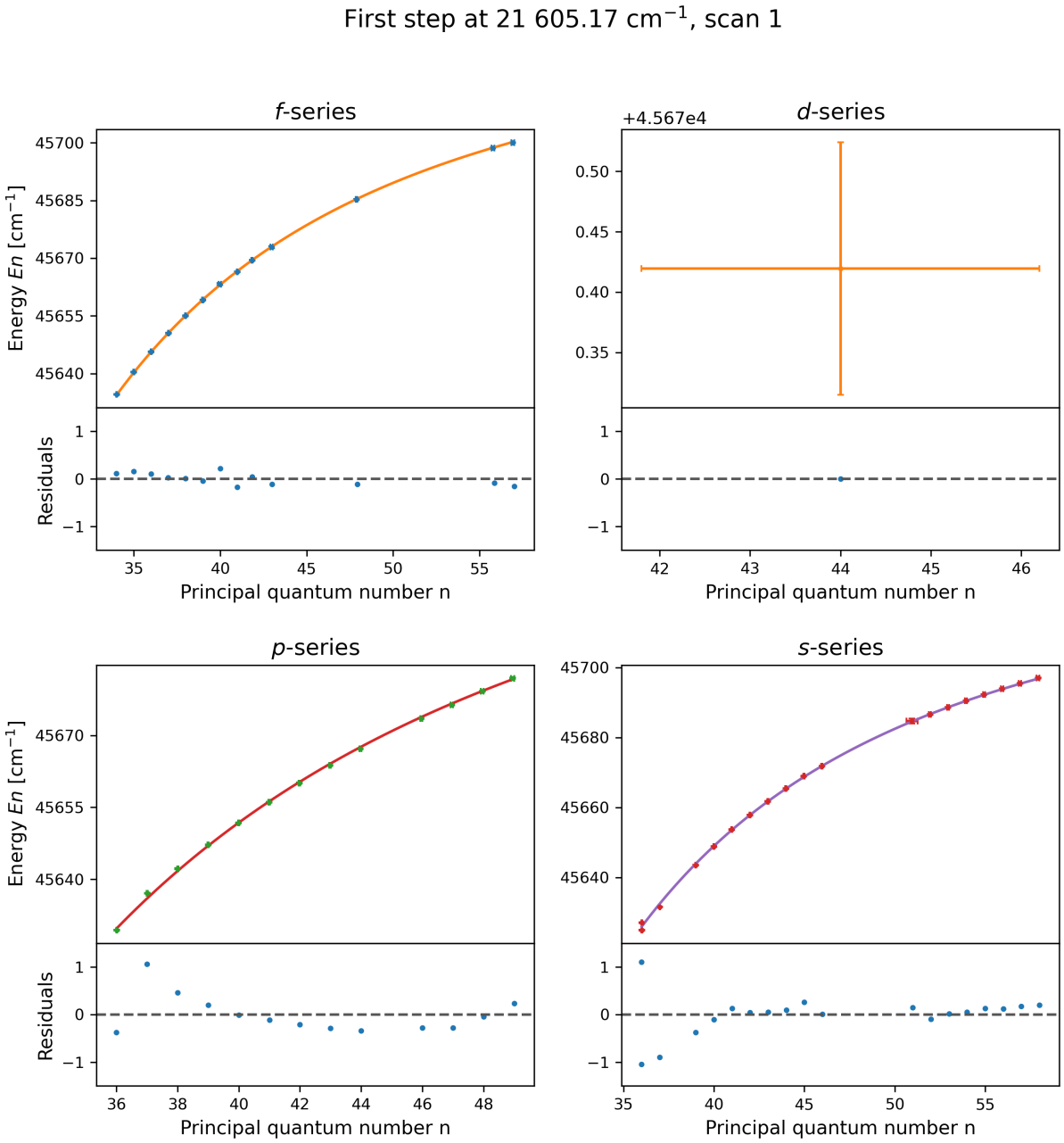

Figure B.2: *Fit of the energy as a function of the principal quantum number following equation 4.4, for the first scan of the second scheme. Each series is fitted separately, resulting in a different value of the ionisation potential the Rydberg series converge to. Only one datapoint is classified as part of the d-series. As a result, no reliable fit can be made and no ionisation potential can be deduced. Hence, the data of the d-series of this scan is omitted for the rest of the analysis.*

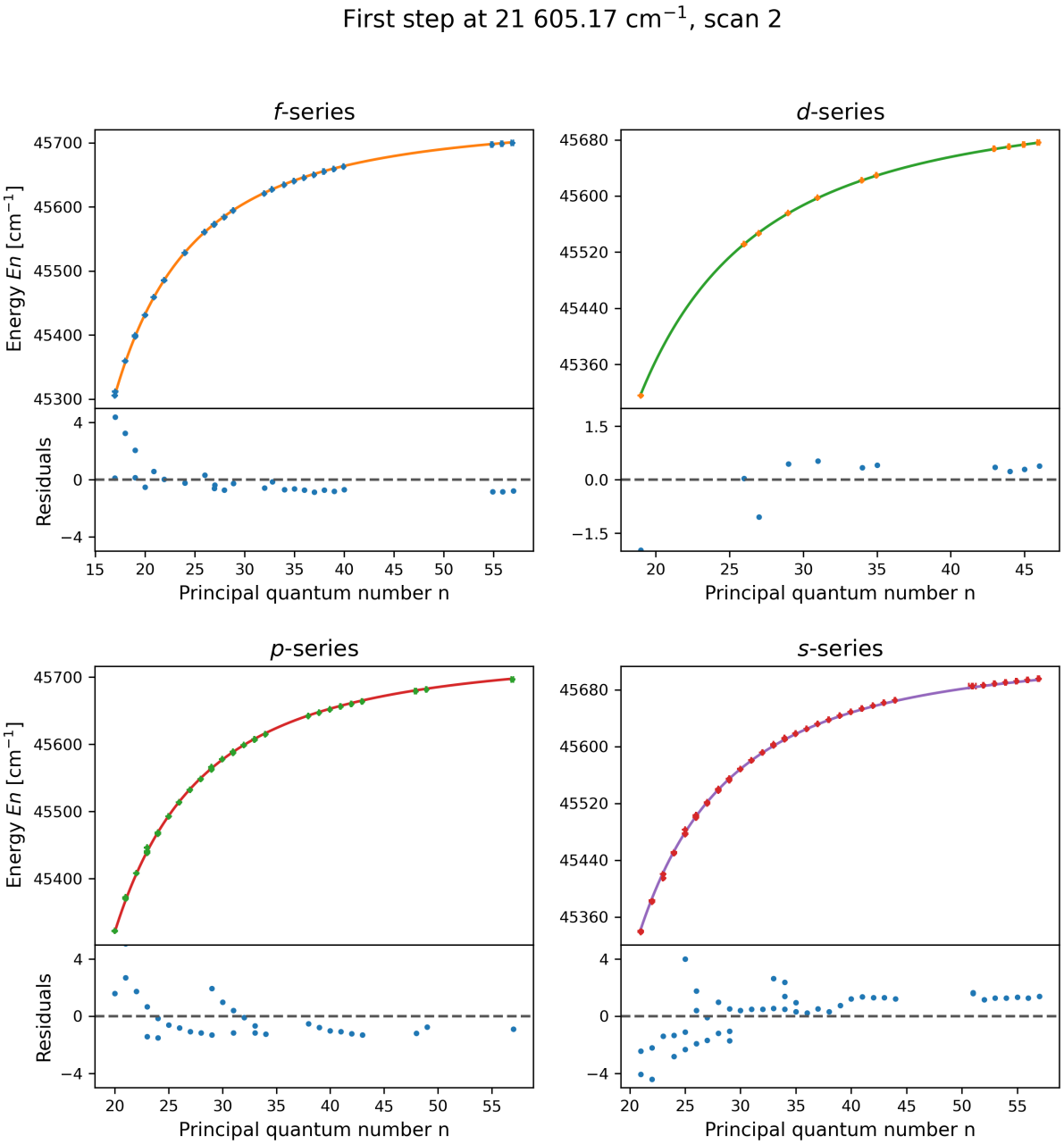

Figure B.3: *Fit of the energy as a function of the principal quantum number following equation 4.4, for the second scan of the second scheme. Each series is fitted separately, resulting in a different value of the ionisation potential the Rydberg series converge to.*

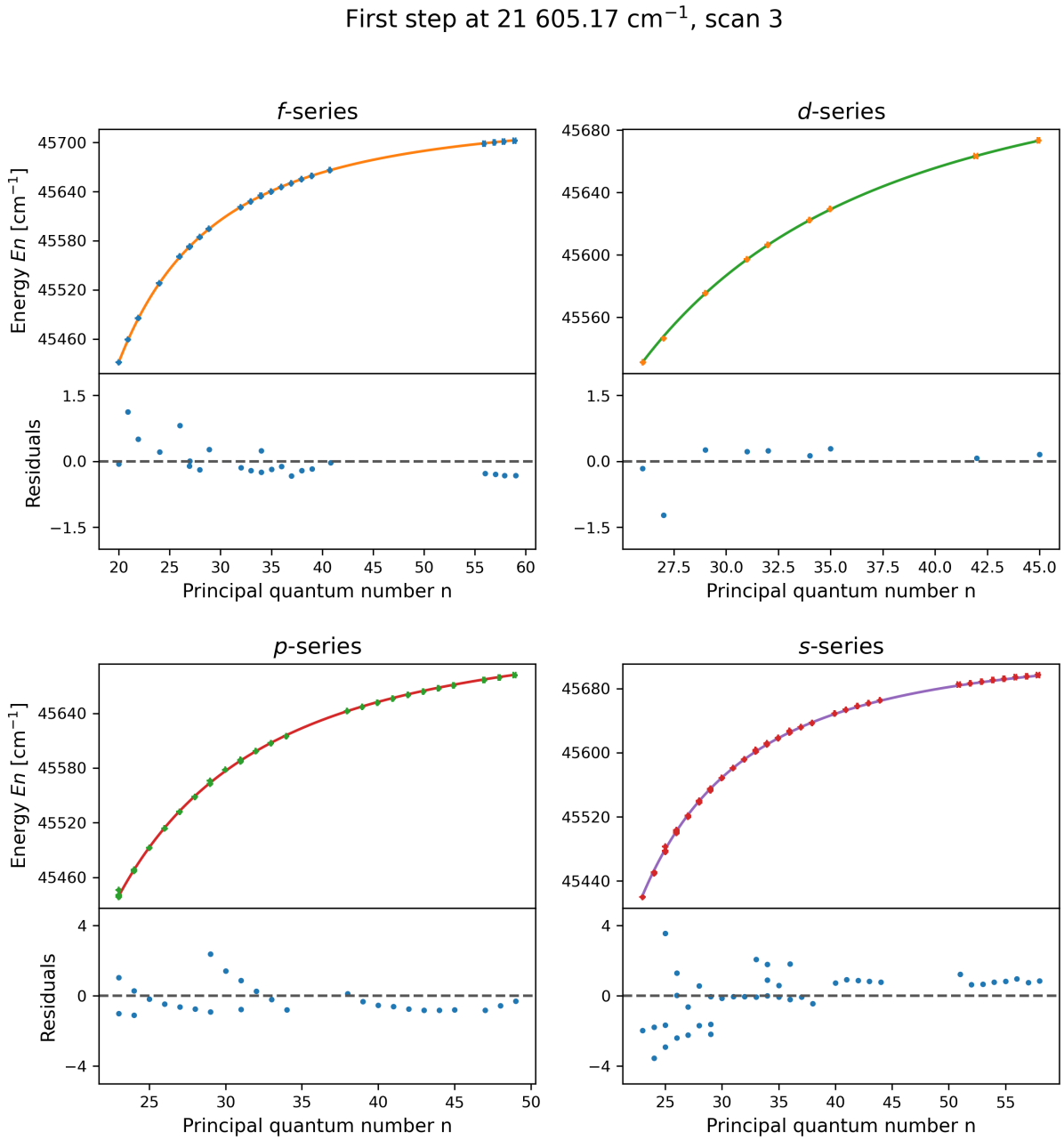

Figure B.4: *Fit of the energy as a function of the principal quantum number following equation 4.4, for the third scan of the second scheme. Each series is fitted separately, resulting in a different value of the ionisation potential the Rydberg series converge to.*

Department of Physics and Astronomy
Celestijnenlaan 200d bus 2412
3001 LEUVEN, BELGIË
tel. + 32 16 32 71 24
www.kuleuven.be